30 GHz Printed Ridge Gap Components and Antennas for Imaging Systems

Islam Sayed Hassan Mohammed Afifi

A Thesis

In the Department

of

Electrical and Computer Engineering

Presented in Partial Fulfillment of the Requirements

For the Degree of

Doctor of Philosophy (Electrical and Computer Engineering) at

Concordia University

Montréal, Québec, Canada

October, 2020

CONCORDIA UNIVERSITY

School of Graduate Studies

This is to certify that the thesis prepared

By: **Islam Sayed Hassan Mohammed Afifi**

Entitled: **30 GHz Printed Ridge Gap Components and Antennas for Imaging Systems**

and submitted in partial fulfillment of the requirements for the degree of

Doctor of Philosophy (Electrical and Computer Engineering)

complies with the regulations of the University and meets the accepted standards with respect to originality and quality.

Signed by the final examining committee:

	Chair
Dr. Rajamohan Ganesan	
	External Examiner
Dr. Mohamed Bakr	
	External to Program
Dr. Amr Yousef	
	Examiner
Dr. Ahmed A. Kishk	
	Examiner
Dr. Christopher W. Trueman	
	Thesis Supervisor
Dr. Abdel Razik Sebak	

Approved by:

Dr. Wei-Ping Zhu, Graduate Program Director

October 7, 2020

Dr. Mourad Debbabi, Acting Dean,
Gina Cody Schoool of Engineering & Computer Science

Abstract

30 GHz Printed Ridge Gap Components and Antennas for Imaging Systems

Islam Sayed Hassan Mohammed Afifi, Ph.D.

Concordia University

Working at millimeter waves (MMW) has gained massive attention for wireless communications and imaging systems. For imaging systems, MMW can be used for security to provide good resolution images and detect concealed weapons as it can penetrate common clothes and reflect from the human body and metal objects. Moreover, MMW is safe for human health, contrary to conventional X-ray imaging, which uses an ionized wave. Thus, it has a harmful effect on human health.

This research is focusing on building an active wide-view angle millimeter-wave imaging system with a small area of mechanical movement to reduce the data collection time. The imaging system is composed of three main parts: 1) the millimeter-wave components and antennas, 2) the mechanical part for moving the antennas and performing the scan of the imaging area, and 3) the imaging reconstruction algorithm.

In order to have an efficient imaging system, the printed ridge gap technology (PRGW) is used to build the imaging system components and antennas. High efficiency coaxial to PRGW transition with a fractional bandwidth of 59.22% at 32.25 GHz is designed to feed the system components. For the transmitting part of the imaging system, a moderate gain PRGW differential feeding planar aperture antenna and a wideband rat-race coupler are designed. The antenna, the rat-race, and the coaxial transition are combined to form the transmitting part, then fabricated and measured. The resulted bandwidth is from 25.62 to 34.34 GHz with a return loss better than 10 dB, a maximum gain of 12.28 dBi, and 3-dB gain bandwidth from 25.62 to 33.77 GHz.

For the receiving antenna, a PRGW Butler matrix and its components (directional couplers, 45° phase shifters, and crossovers) are designed. A semi-log periodic antenna fed

by the PRGW is designed as the radiating element. The PRGW components, the coaxial transition, and the antennas are combined to form the receiving part of the imaging system, which is fabricated and measured. The resulting beam directions are at $\pm 13^{\circ}$ and $\pm 36^{\circ}$, at the center frequency (30 GHz). The return loss and the isolations are better than 10 dB over the frequency range from 26.1 to 33.5 GHz.

For the imaging reconstruction algorithm, a synthetic aperture radar algorithm is used. Two tests are carried out, one uses CST simulation results, and the other uses measured data from the Concordia antenna chamber lab. The results show an output resolution of 0.6 λ.

Finally, the whole imaging system is built with the designed differential feeding antenna as the transmitter, the designed Butler matrix as the receiver, and the synthetic aperture algorithm as the image reconstruction algorithm. The performance network analyzer (PNA) is used to collect the data (s-parameters) required to reconstruct the image, and the antenna range controller system (NSI 5913) is used to mechanically scan the imaging area. The imaging system is used to scan a mannequin carrying an object shaped like a pistol and a knife. The results show that the two objects are detected.

Acknowledgments

First, all praise and thanks to Allah for my success in completing this thesis. I would like to thank my father, mother, and brother for supporting me in all my life.

I sincerely want to thank my supervisor Professor Abdel Razik Sebak for giving me the opportunity to join his group and supporting me during the Ph.D. journey.

Also, I would like to thank my committee members, Professor Ahmed Kishk, Professor Christopher W. Trueman, and Professor Amr Yousef for their review of my thesis and their comments that help me in illustrating my ideas in a good way. Furthermore, I would like to thank professor Mohamed Bakr for accepting to be the external examiner for my thesis and for his valuable comments.

My thanks to my colleagues, who provided me with good research and friendly environment, Abduladeem Beltayib, Magid Alzidani, Muftah Asaadi, Essa Mujammami, Abdullah Attar, Nadeem Ashraf, Marjan Jalali Moghadam, Mohammed Akbari, Reza Movahedinia, Walid Dyab, Ahmad Sakar, Mohamed Ali, and Issa Mohammed.

I also want to thank Vincent Chopin and Jeff Landry for their technical assistance in the measurement and fabrication processes.

Finally, I would like to express my thanks to the Egyptian Cultural Affairs and Scholarships Sector to give me this Ph.D. scholarship at Concordia University.

Contribution of Authors

There are joint publications out of this thesis. The authors' contributions in jointly-published one journal and two conference papers related to this thesis are presented as follows. In addition, my supervisor, Professor Abdel Razik Sebak, attested to the accuracy of this statement

In chapter 3, the coaxial to ridge gap transition is presented. There is a published journal out of this part [J1]. The contribution of the authors can be summarized as:

- I have studied the topic, designed and simulated the transition, and written the paper;
- Dr. M. Ali has helped me with the fabrication and measurement processes, and on the revision of the paper;
- As the research supervisor, Professor Abdel Razik Sebak provided guidance and direction on all aspects of the considered topic.

In chapter 4, the design of the semi-log periodic antenna with ridge gap feeding is presented. There is a published conference out of this part [C1]. The contribution of the authors can be summarized as:

- I have searched and studied about the topic, designed and simulated the antenna, and written the paper;
- Dr. M. Ali has helped in revising the paper;
- As the research supervisor, Professor Abdel Razik Sebak provided guidance and direction on all aspects of the considered topic.

In chapter 4, the design of the differential feeding antenna is presented. There is a published conference out of this part [C2]. The contribution of the authors can be summarized as:

- I have searched and studied about the topic, and designed and simulated the antenna;
- Mr. M. Alzidani has helped in writing the paper;
- As the research supervisor, Professor Abdel Razik Sebak provided guidance and direction on all aspects of the considered topic.

Contents

List of Figures

List of Tables

List of Abbreviations

1D	one-Dimension
2D	Two-Dimension
3D	Three-Dimension
5G	Fifth generation communication
AF	Array factor
AMC	Artificial Magnetic Conductor
BW	Bandwidth
CST	Computer Simulation Technology
FITD	Finite Integral Time Domain
FIFD	Finite Integral Frequency Domain
HFSS	High frequency structure simulator
MMW	Millimeter wave
MS	Microstrip
PCB	Printed Circuit Board
PEC	Perfect Electric Conductor
PMC	Perfect Magnetic Conductor
PNA	Performance Network Analyzer
QTEM	Quasi Transverse electromagnetic wave
Radar	Radio Detection And Ranging
RGW	Ridge gap waveguide
Rx	Receiver
SAR	Synthesized aperture radar
SIW	Substrate Integrated Waveguide
SNR	Signal-to-Noise Ratio
TE	Transverse Electro-magnetic wave
Tx	Transmitter

List of Symbols

α	Attenuation constant
β	Propagation constant
C	Capacitance
f	Frequency
L	Inductance
Z	Impedance

Chapter 1

Introduction

1.1 Introduction

Today, there is a great demand for millimeter-wave (MMW) imaging. MMW is the band of the spectrum from 30 to 300 GHz. The MMWs can penetrate common clothes and reflect from the human body and metal objects, so it is a good candidate for security imaging. MMW has non-ionized radiation, which makes it a safe option for human health, in contrast to conventional X-ray imaging, which could have negative health impacts [1–7] (as it uses ionized waves). MMW can penetrate fogs and clouds, which makes it a good candidate for navigation with low visibility conditions [8]. Moreover, MMW imaging is suitable for both day and night vision.

Imaging systems can be classified into two categories: passive and active imaging systems. A passive imaging system depends on the natural radiation from objects, while an active imaging system requires a radiation source to illuminate the objects.

In this thesis, active imaging is considered due to its advantages over passive imaging. These advantages include: 1) small and low profile antennas can be used and then synthesized to form the image instead of a large antenna array or a parabolic reflector antenna as with passive imaging; and 2) 3-D imaging can be constructed by combining the synthesized aperture radar technique with 2-D mechanical scanning. An active imaging system is composed of three parts: the microwave/millimeter-wave components and antennas, the mechanical part, and the signal processing part. The focus of our research is on the design of MMW components for an active imaging system.

Several technologies have been used to implement imaging systems. In [9], a microstrip patch antenna is used for imaging with a sparse array to reduce the number of antenna elements at 31.5 GHz. In [10] and [11], a silicon-based on-chip antenna is used with mechanical scanning to produce 3D images at 30 GHz and 240 GHz. In [12], horn antennas are used for imaging a rotating object at 30 GHz.

In this thesis, the printed ridge gap waveguide (PRGW) technology is used as an alternative efficient type of guiding structure suitable for the MMW frequency band. It functions by surrounding the guiding line with bandgap unit cells so that the wave propagates along the line and evanescent outside the line. The propagating mode is a quasi-TEM mode that has a low signal distortion, and the wave propagates on an air gap above a dielectric substrate so it has a very low dielectric loss. Moreover, it can be integrated with the printed circuit board (PCB) technology and thereby connected to other devices.

1.2 Motivation

Millimeter-wave imaging can be used for security and radar applications. Its non-ionized radiation behavior makes it a good candidate for human security imaging, replacing conventional X-ray imaging [1–7]. It can penetrate common clothes, and it reflects from metal objects, which is suitable for concealed weapon detection. Also, it can provide quality resolution images. For radar applications, MMW can penetrate fogs and clouds so it can be used in a navigation system or for synthetic aperture radar (SAR).

The conventional technologies used to build microwave components and antennas have several drawbacks at the MMW range. The microstrip technology has dielectric and radiation losses. The rectangular waveguide is difficult to manufacture, as the dimensions become very small and thus is expensive. Therefore, new technologies have been developed to work at high frequencies, such as the substrate integrated waveguide (SIW) and the ridge gap waveguide (RGW). The SIW has overcome the radiation losses presented in the microstrip line and is compatible with PCB technology. However, it still has dielectric losses and signal distortion (propagating mode is TE_{10}). The RGW is a

promising technology as it has overcome the dielectric losses and the signal distortion (its propagating mode is Quasi-TEM), but it is expensive and not compatible with PCB technology. The work presented in this thesis is implemented using PRGW technology, which is compatible with PCB technology and hence is low cost. Moreover, it overcomes the signals distortion problems. This research focuses on designing basic MMW components and antennas using this technology. These components and antennas are then used to build an active imaging system.

1.3 Problem Statement

Imaging systems are required for screening at security checkpoints and for quality measurement in the industry. The MMW band is a good candidate for that task as it is a non-ionized wave and has a small wavelength that leads to good quality images. Imaging systems are generally required to provide images rapidly. Also, they are more effective if they have a wide view angle. An active MMW imaging system can be realized by applying the mono-static back projection algorithm [13]. However, this approach requires a long time to collect the data and produce the image. Moreover, the scanning area is almost the same as the target area, which requires a large mechanical system to scan large objects.

Another approach to creating an imaging system is to have many antennas in a 2-D planar surface and apply the multi-static algorithm to produce the image [14, 15]. However, this approach requires several antennas, which makes the system rather expensive to implement. Yet another imaging uses a 1-D array of antennas to scan in one direction and performs mechanical scanning in the other direction [1, 16]. This system is a compromise between the two above-mentioned systems. However, this approach requires a large mechanical system to scan an area that is the same as the target area, as well as the construction of a long 1-D antenna array with electronic switching, both of which are costly.

Another imaging system utilizes a reflectometer [17, 18]. This approach uses a time-domain reflected signal to form a good quality MMW image. However, it takes a long time to conduct the scanning step, as the scanning area is the same as the imaged area. Furthermore, the technology utilized to build these systems is either microstrip, rectangular waveguide, or silicon-based structures that have high losses in the MMW band.

The system proposed in this thesis has a mechanical scanning area smaller than the target area, which reduces the cost of the mechanical system and saves time compared to the mono-static case. Moreover, it is built with PRGW technology, which has low losses, low signal distortion, and is compatible with PCB technology. In order to build the proposed system, a beam switching network is required, as well as a moderate gain antenna. Therefore, a wideband PRGW Butler matrix is designed in this thesis, as it is the matrix-based beamforming network with the lowest number of components. Also, a PRGW differential feeding planar aperture antenna is designed as the moderate gain antenna with a wideband and a stable broadside radiation pattern.

1.4 Objective

The main objective of this research is to implement an MMW imaging system using PRGW technology. The research is carried out in two phases. In the first phase, MMW components and antennas (important blocks of the imaging system) are designed and fabricated. In the second phase, the data collection and image reconstruction algorithm are performed.

The transmitting part of the imaging system is a wideband differential feeding moderate gain antenna (12- 15dBi). The associated research activities are:

- Designing a wideband coaxial to PRGW transition;
- Designing a moderate gain differential feeding antenna; and
- Designing a wideband rat-race coupler for the differential feeding.

The receiving part of the system is composed of a beamforming network (Butler matrix) and radiating antennas, as shown in Figure 1.1. The associated research activities focus on the development of the following components:

- Butler matrix components: a wideband 3-dB hybrid coupler, a wideband 45° phase shifter, and a wideband crossover; and
- A radiating element: a wideband PRGW antenna.

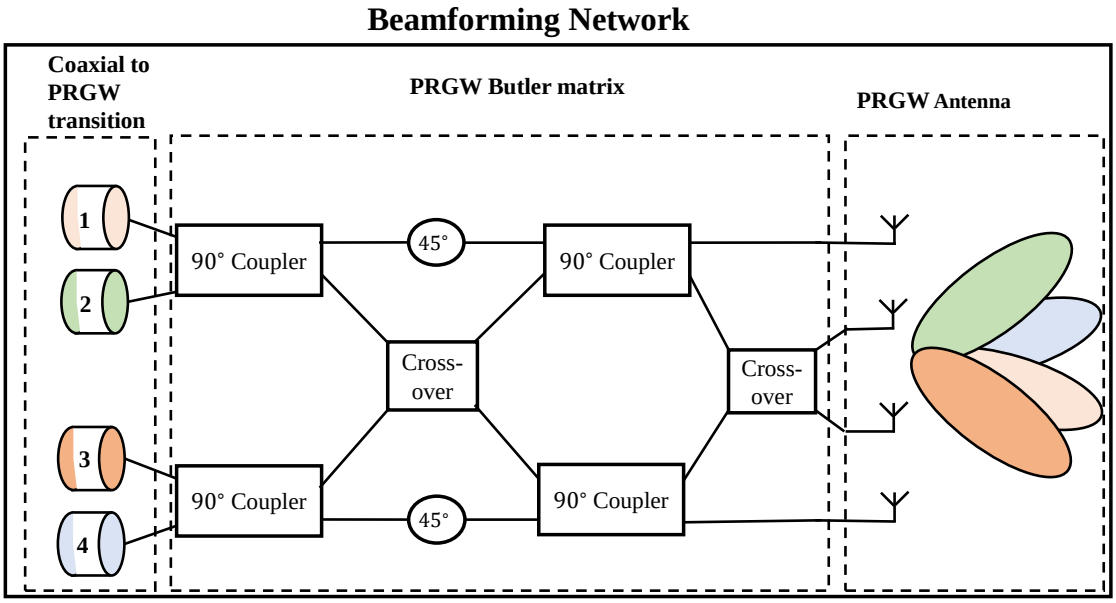

Figure 1.1: The beamforming network consists of the coaxial feeding, the Butler matrix, and the radiating elements

The imaging system components and antennas are integrated to form the imaging system, in which:

- The performance network analyzer (PNA) is connected to the transmitting and the receiving parts and is used to generate and collect the MMW signals;
- The NSI 5913 antenna range controller system available in Concordia micro/millimeter-wave lab is used as the mechanical system; and
- The collected data is processed off-line on a PC using Matlab code, based on the synthesized aperture algorithm, to produce the MMW image.

The whole system, as illustrated in Figure 1.2, employs multiple moderate gain (12 - 15 dBi) antennas, operating at different frequencies, to illuminate the object. As the imaged object is illuminated from different directions, a wideband switched-beam antenna is used to collect the reflected signals. A beamforming network that performs space multiplexing is required in the receiving antenna to enhance the signal to noise ratio and hence the produced image quality. Moreover, the use of wideband components allows the use of different frequencies to perform frequency multiplexing that helps to have adequate isolation between the antennas. Therefore, all the transmitters can work at the same time without interference.

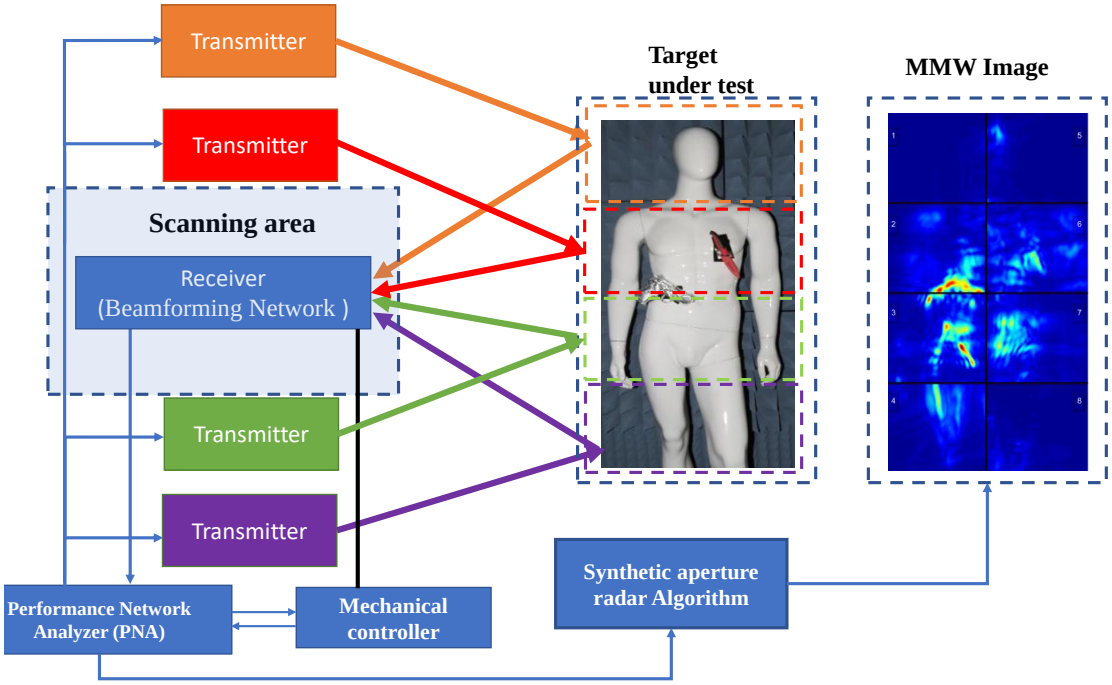

Figure 1.2: Millimeter-wave imaging system.

The proposed imaging system offers a wide-view angle, minimal mechanical movement, and potentially a low cost. It produces good quality images with a resolution near the Abbe limit ($\delta l \approx \lambda/2$). It is faster than conventional mono-static imaging, as the scanning area is half the imaged area instead of needing to be the same as the imaging area.

1.5 System Design Methodology

The system design methodology is shown in Figure 1.3. The system resolution is set to $\lambda/2$ (the Abbe limit), and the synthetic aperture technique is used to collect the data and reconstruct the image. The design methodology of the MMW components and antennas in the PRGW technology is summarized as: 1) setting the initial parameters; 2) building the simulation model; and 3) optimizing the design until the specifications are met.

As noted at the end of section 1.3, the mechanical scanning combined with the synthetic aperture technique is selected as it overcomes the drawbacks of other scenarios. In the first possible scenario, a fixed receiving antenna is used, and a one-pixel image is produced, as there is only one S_{21} between the transmitting and the receiving antennas. In the second scenario, a multi-beam fixed antenna is used to produce an N pixel image, where N is the number of the ports of the beamforming network, feeding the multi-beam antenna. However, as the number of ports of the beamforming network is increased, the far field region of the antenna will be too far from the antenna, and the resolution will degrade. Moreover, there will be more losses in the beamforming network as it will become lengthy and contains many components. Therefore, a synthetic aperture technique is used to overcome these issues. The main idea of the synthetic aperture technique is that a group of wide beamwidth antennas placed separately from each other can be used to collect the reflected signals from the imaged object. After that, the collected data can be processed to produce an image with the same resolution as if there is a large aperture antenna. It also has an advantage in that the object can be placed close to the scanning area, thereby increasing the resolution (the far field of low gain wide beamwidth antennas are short). In this thesis, a four-beam receiving antenna is used and moved in the xy-plane by a mechanical controller device to collect the data at different points.

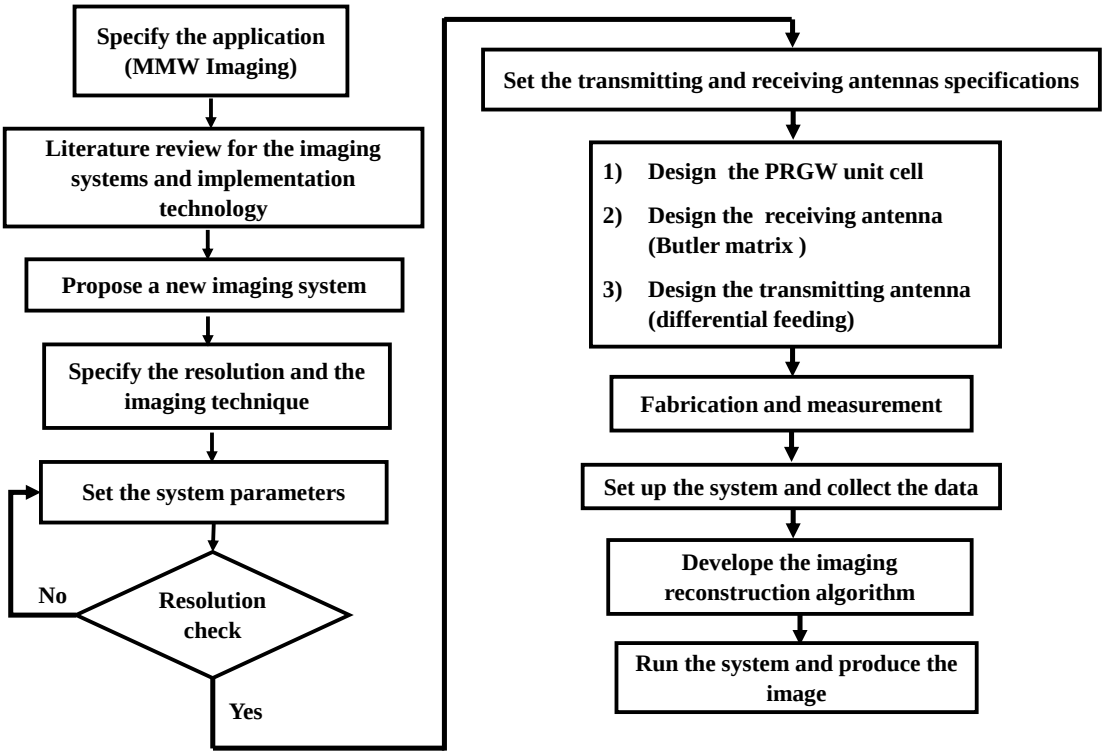

Figure 1.3: Imaging system design methodology

1.6 Contributions

The contributions of this thesis are divided into three parts: 1) the design and specification of MMW PRGW components for the proposed active imaging system; 2) the integration of the components with antennas to form the transmitting and the receiving parts of the imaging system; and 3) the fabrication and implementation of the proposed wide-view angle active imaging system.

The contributions of the reported work are:

- The design of a wideband coaxial to PRGW transition that is very compact, compared to other transitions in the literature, and avoids the dielectric and radiation losses presented by other microstrip transitions [J1]. Also, the proposed design procedure is suitable for metal and printed ridge gap waveguides at different frequencies. It has a fractional bandwidth of 59.22% at 32 GHz.

- The design of a wideband rat-race coupler using PRGW technology [J2] to differentially feed a moderate gain antenna. The design is based on adding a stub in

the middle of the $3/4\,\lambda$ branch line and quarter wave transformers in all the ports. The addition of the stub introduces a separation between the output amplitudes and hence two intersection points are obtained that increases the amplitude imbalance bandwidth, while the addition of the quarter wave transformers increases the matching and isolation bandwidths. The rat-race coupler design has a bandwidth from 25.8 to 34.2 GHz with return loss and isolation better than 15 dB. The amplitude imbalance between the output ports is ± 0.5 dB.

- The design of a moderate gain differential feeding antenna (12-15 dBi) and its integration with the rat-race coupler and the coaxial feeding, transmitter part. Differential feeding is used to have a stable broadside radiation pattern while capacitive coupling results in a wide bandwidth. The antenna bandwidth is from 25.62 to 34.34 GHz with $S_{11} \leq -10$ dB and a maximum gain of 12.28 dBi and 3-dB bandwidth from 25.62 to 33.77 GHz.

- The design of a 1-D 4×4 Butler matrix using PRGW technology to achieve low losses with a wideband performance and then integrating it with a semi-log periodic antenna and the coaxial feeding to form the receiving part [J3]. The directional coupler is designed based on altering the impedance of the normal branch line coupler and adding quarter-wave transformers at all ports to have two intersection points between the output coupling instead of one in the conventional case. The simulated results of the coupler are: (1) the bandwidth is 7.35 GHz around 30 GHz, (2) the return loss and isolation are better than 15 dB, (3) the output amplitude imbalance is -3.375 ± 0.425 dB, (4) the output phase difference is $90.9^\circ \pm 1.62^\circ$. The phase shifter is designed based on using a coupled line coupler with two ports connected to each other. It is the first wideband phase shifter designed in the ridge gap waveguide technology (BW $> 20\%$). It has a matching bandwidth ($S_{11} < -15$ dB) from 27 to 33.6 GHz with an output phase shift of $45^\circ \pm 2^\circ$. Finally, the crossover is built using three cascaded couplers, in which the dimensions are optimized to maximize the operational bandwidth while maintaining good matching and isolation levels. A

bandwidth from 26.8 to 33.9 GHz is obtained with return loss and isolation better than 14 dB, and the insertion loss is better than 0.5 dB. It has the optimum design compared to previous works in terms of size and bandwidth.

- The implementation of a system that requires less mechanical movement compared to conventional mono-static imaging, and hence allows for more rapid scanning. Also, the developed MMW imaging system uses less computational resources than conventional mono-static imaging and thus requires less processing time. The resulted images have a resolution near the Abbe limit.

1.7 Organization of The Thesis

This thesis consists of six chapters. The first chapter contains the introduction, the problem statement, the motivation, and the objective. Chapter 2 presents literature review of MMW imaging, beamforming networks, and differential feeding antennas. Chapter 3 elaborates the design of the imaging system, the coaxial to ridge gap transition, and of the basic MMW components (a 3-dB coupler, a 45° phase shifter, a crossover, and a rat-race coupler). The design of the differential feeding antenna and its integration with the rat-race coupler are presented in chapter 4, as well as the design of a semi-log periodic antenna and its integration with the Butler matrix. The imaging reconstruction algorithm and the resulted images are presented in chapter 5. Finally, the conclusions and promising future work are discussed in chapter 6.

Chapter 2

Literature Review

The literature review focuses on six parts. First, millimeter imaging techniques are discussed. Second, the resolution limits of imaging systems are presented. Third, the printed ridge gap technology is compared with other technologies to illustrate the advantage of this technology over others. Fourth, reported works of a coaxial to printed ridge gap waveguide are illustrated, feeding of the imaging system components. Fifth, a brief review of low profile antennas (transmitting part of the designed imaging system) is given. Finally, a literature review of the Butler matrix (receiving part of the imaging system) is presented.

2.1 Millimeter-Wave Imaging

Millimeter-wave imaging has many applications such as medical imaging, security imaging, non-destructive testing, and radars. In this thesis, we focus on MMW imaging at 30 GHz. It has a high potential to replace conventional X-ray imaging in airports and surveillance applications because of its ability to provide a good resolution image and be safe for human health. Also, as it has a low penetration depth in the human body, it can be used for medical imaging to detect skin and breast cancers. Moreover, as it can penetrate fogs and dust, it can be used in navigation systems and high-resolution radars. In general, there are two types of imaging systems, namely passive imaging and active imaging.

Passive MMW imaging system is based on the radiometer concept [19] in which the natural radiation from the objects is collected by the antenna. Passive imaging system requires a large number of antennas to form the picture in real-time and may also needs a dielectric lens to capture a large area (like the principle of operation of the visible camera). Also, it can be constructed by a high gain Cassegrain antenna with a mechanical movement to scan the whole image. The image resolution depends on the size of the antenna [20, 21]. For a large size antenna, the gain is high, and the beamwidth is narrow. Therefore, fine-resolution can be obtained, whereas a small antenna with low gain and hence a wide beamwidth will degrade the image resolution. Figure 2.1 shows a schematic of a passive imaging system where a parabolic antenna is used as the receiver. The antenna is moved in the vertical and horizontal axes by the mechanical controller system to scan the target area while the radiometer is used to calculate the natural radiated power from the target. The resolution can be calculated from the 3-dB beamwidth of the antenna (θ_{HP}) as

$$d = \theta_{HP} R \tag{2.1}$$

where d is the resolution of the resulted image and R is the distance between the antenna and the target. Another way to construct a passive imaging system is by using a phased array, where the resolution depends on the size of the array [22].

Active imaging is another type of MMW imaging system in which an antenna is used as a radiating source to illuminate the imaged object, and another antenna is used as a receiver. After that, signal processing is used to analyze the collected data to form the image. Active imaging can be used to construct 3D images, as the time axis can be used to determine the object distance from the imaging system (ranging dimension or z-axis) beside the 2D axis of the spatial scanning (x and y-axis) [1]. This is an advantage of the active imaging over passive imaging, which depends on the incoherent thermal radiation of the object; hence no ranging dimension can be obtained [23]. Also, active imaging can be used to construct 2D images either by considering one space dimension besides the time dimension as in the synthetic aperture radar [13], or by using a 2D space dimension

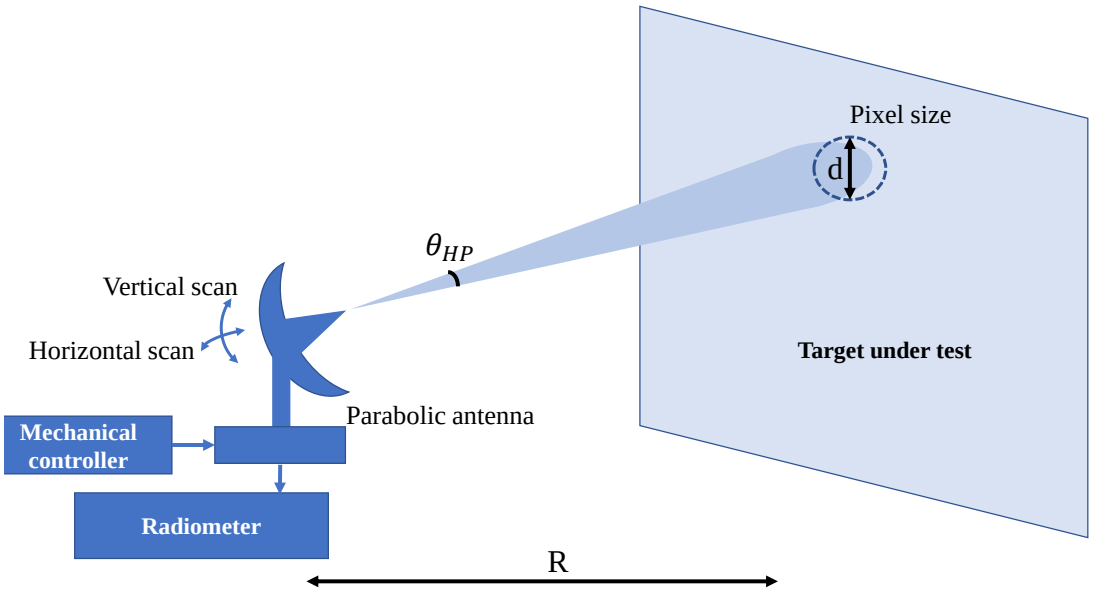

Figure 2.1: A passive imaging system.

and only a single operating frequency [12].

The active imaging can be classified according to the way of illumination and collection of the data as:

1. Mono-static, in which the transmitter and the receiver are very close to each other or only one antenna is used with a circulator [1].

2. Bi-static, in which the transmitter and the receiver are separated from each other.

3. Multi-static, in which there are multi-transmitters and receivers [12, 14].

Figure 2.2 shows an active mono-static imaging system where the transmitter and the receiver coincide with each other. The mechanical controller is used to move the antennas in a raster scan motion on the scanning area. The PNA is used to calculate the reflected signals that are processed using the synthetic aperture radar algorithm to have the final image. The equations regarding the resolution of such a system are given in section 2.3.

A comparison between active imaging using a single frequency scanning (2D) and using a wide frequency band scanning (3D) can be found in [1]. Figure 2.3 (a) shows the millimeter-wave image of a person using the mono-static method at a single frequency

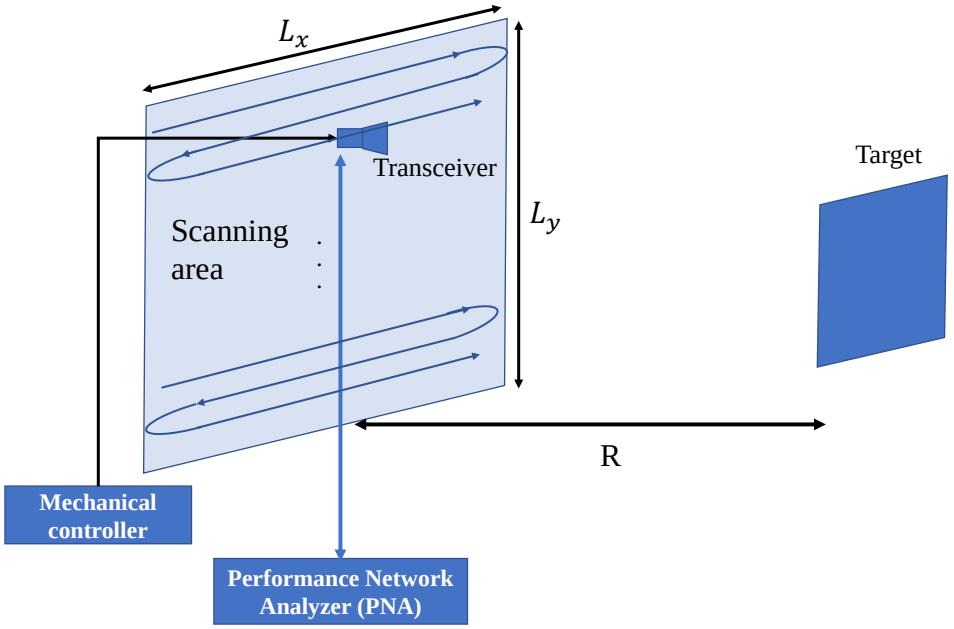

Figure 2.2: An active mono-static imaging system.

of 35 GHz. Figure 2.3 (b) shows the millimeter-wave image of the same person using the mono-static method with a wide frequency band (from 27 to 33 GHz). It is clear that using a wide frequency band is better, as we have access to the range dimension; hence a high quality image can be obtained. Moreover, in [24], a 10 GHz bandwidth around 35 GHz is used to produce a 3D imaging of a human body model. Also, in [25], a wideband spiral antenna (10- 40 GHz) is used to produce a 3D image.

Another example of active imaging is found in [12], where the multi-static method is used to construct the image of a tilted object with respect to the plane of the scanning aperture. The advantage of using multi-static over mono-static and bi-static is that it can capture the reflection from non-flat surfaces (as it has many transmitters and receivers), hence better images are resulted. Figure 2.4 (a) shows the schematic structure of the multi-static system where the system works at 30 GHz, and the object is tilted by 30°. Figure 2.4 (b) and (c) show the object and the resulted image, respectively.

Indeed, the time for the scanning is an important factor in imaging systems; it depends on the scanning mechanism. When one transmitter and one receiver are used with

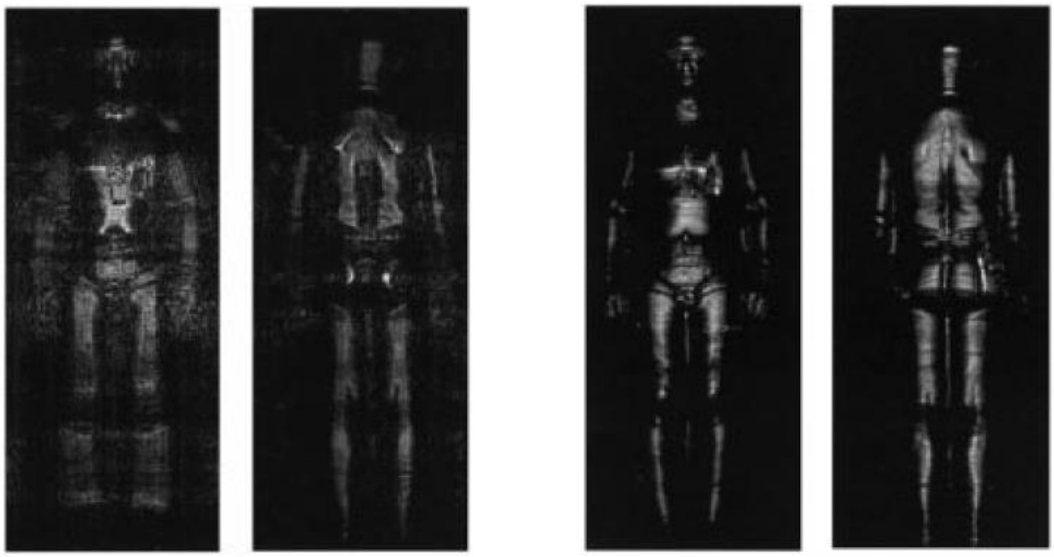

(a) (b)

Figure 2.3: Millimeter-wave imaging using mono-static method. (a) Front and back of a person using single frequency scanning at 35 GHz. (b) The front and back of a person using wide frequency band from 27 to 33 GHz, (D.M. Sheen et al [1], ©2001 IEEE.)

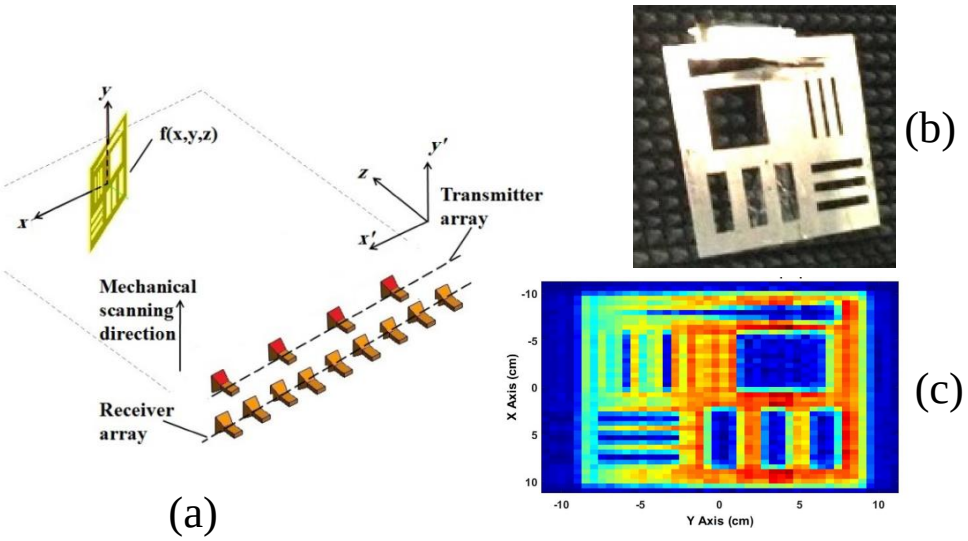

Figure 2.4: Millimeter-wave imaging using multi-static method at a single frequency (30 GHz) to image a tilted object. (a) The schematic structure of the system. (b) The scanned object. (c) The constructed image (A. A. Farsaee et al [12], ©2018 IET.)

2D spatial scanning, it takes a very long time. The time can be reduced by using electronic switching in one direction and mechanical scanning in the other direction [1]. A further improvement is achieved by making the whole system electronically switched, and a real-time image can be obtained (measurement time is less than 50 ms, and the image results within 2 seconds [14]). However, increasing the number of transmitters and receivers makes the cost of the system very high. Another approach to decrease the time and the number of antenna elements is introduced in [9, 26], where a sparse array is used to decrease the number of elements while maintaining good quality images.

Another factor in the active imaging systems is the efficient illumination of the imaged object as it has an important role in the quality of the produced image. In [27], a modified multi-static imaging system is proposed that gives better resolution compared to the conventional multi-static imaging systems, as shown in Figure 2.5. The system depends on rotating the antenna beams to efficiently illuminate the object. Also, the authors in [27] used a modified synthetic aperture radar technique to reconstruct the image and avoid the redundancy in the information coming from each transmitter.

The imaging reconstruction algorithms depend mainly on the Fourier transform [1, 24, 28]. It is used to construct a 2D or a 3D image. Also, it is suitable for high-speed processing, as we can take advantage of the fast Fourier transform functions implemented in many software programs.

2.2 Resolution Limits of Imaging Systems

Any imaging system has limitations on the resolution of the produced image. These limitations can be classified into two categories: the instrument limitation and the diffraction limit. The instrument limitation depends on the quality of the used sensors and the used lenses. In this case, the image resolution can be improved by changing the technology and use high quality components. On the contrary, the diffraction limit is not avoidable and sets the maximum resolution of an imaging system. Therefore, the diffraction limit is discussed here. There are two concepts for the diffraction limit, namely: 1) the Airy pattern

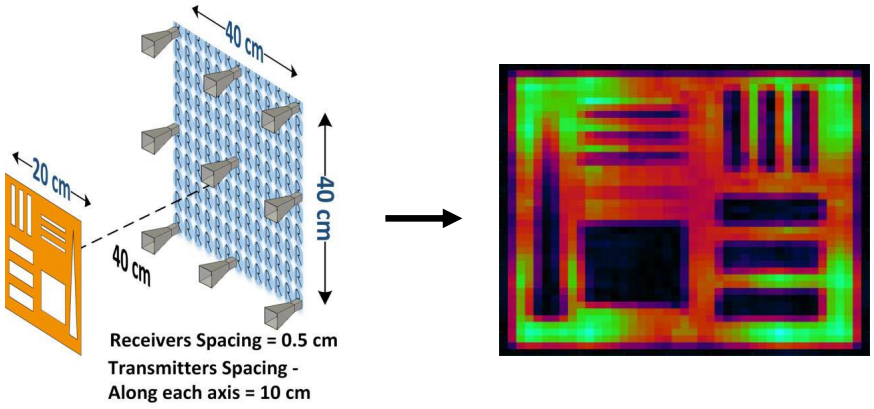

(a)

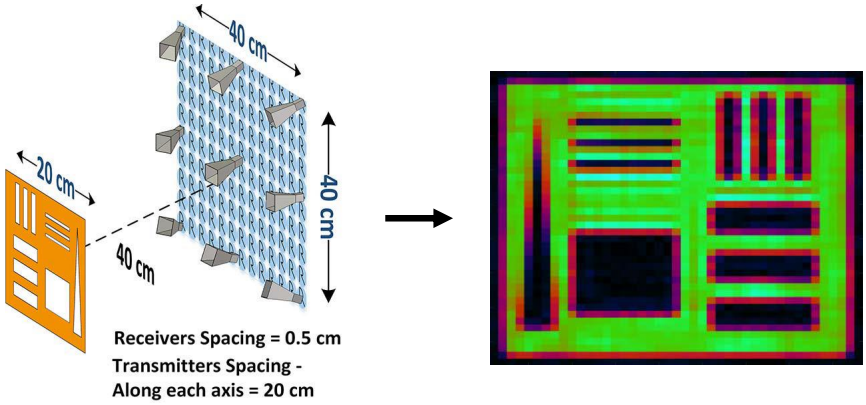

(b)

Figure 2.5: (a) Conventional multi-static imaging system and the resulted image. (b) Modified multi-static imaging system and the resulted image. (M. Kazemi et al [27], ©2019 IEEE.)

and Rayleigh criterion, and 2) Abbe diffraction limit. In this thesis, the Abbe diffraction limit is presented as it sets the maximum resolution limit.

In 1873, Ernst Karl Abbe argued that there is another diffraction limit than that proposed by Rayleigh criterion [29]. He states that a detail with a particular size is resolved when the numerical aperture (NA =n sin α) of the lens is large enough to capture the first-order diffraction pattern produced by the detail, at the working wavelength. Therefore, the spatial resolution of an object is given by

$$\Delta l = \frac{\lambda}{2n \sin \alpha} \tag{2.2}$$

where Δl is the resolvable detail size, λ is the wavelength of used light, n is the index of refraction of the imaging medium, and α is the half-angle subtended by the microscope lens, as shown in Figure 2.6. From this theory by Abbe, the minimum detail size that can be resolved for an imaging system capturing an image in the air is

$$\Delta l_{min} = \frac{\lambda_0}{2} \tag{2.3}$$

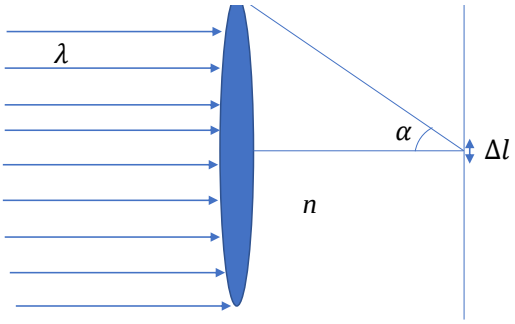

Figure 2.6: Geometry of Abbe diffraction limit.

2.3 Synthetic Aperture Technique for Active Imaging Systems

Aperture synthesis was first developed at radio wavelengths by Martin Ryle and coworkers from the Radio Astronomy group at Cambridge University. Martin Ryle has received the Nobel Prize for this work [30]. "Aperture synthesis or synthesis imaging is defined as a type of interferometry that mixes signals from a collection of telescopes to produce images having the same angular resolution as an instrument has the size of the entire collection" [31].

For a good understanding of the working mechanism, Figure 2.7 shows a comparison between a synthetic aperture antenna and a large aperture antenna. In the synthetic aperture antenna, small antennas with wide beamwidth are used at different locations along a line or a 2D grid to capture the signal from a target. After that, the collected signals are

processed to produce an image with the same resolution as that can be produced with a large aperture antenna occupying the whole line or 2D grid. Furthermore, a single antenna can be used to do this task by moving it along a line or in a 2D grid to collect the data at different positions.

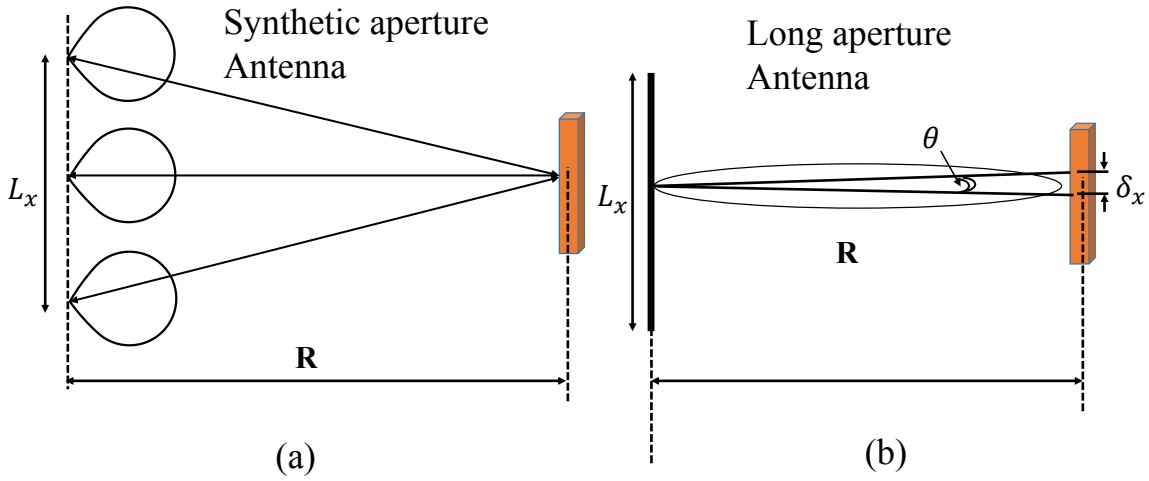

Figure 2.7: (a) Synthetic aperture antenna. (b) Large aperture antenna

For the imaging system in this thesis, an antenna moving in xy-plane is used to collect the data. Then, the data is processed to produce the final image. The use of the synthetic aperture allows the placement of the object close to the scanning plane, as the far field region of small antennas is short, and hence better resolution can be obtained. Also, the use of small antennas facilities the design of the mechanical scanning system.

2.3.1 Resolution Calculations for Synthetic Aperture Technique

The antenna half-power beamwidth defines the resolution of the imaging system. For simplicity, the case of a long line is considered in which the half-power beamwidth is

calculated as in [32].

$$HP_x \approx 0.886\frac{\lambda_0}{L_x} \tag{2.4}$$

The spatial resolution of an image can be calculated by multiplying the half-power beamwidth with the distance to the target (R) as

$$\delta_x \approx 0.886\frac{\lambda_0\ R}{L_x} \tag{2.5}$$

When dealing with a synthesized aperture, the used phase in synchronization is double the phase of a normal antenna, as the forward and backward phase changes are considered in constructing the image. Therefore, the obtained resolution is approximated by Equation 2.6 as in [1]

$$\delta_{x(syn)} = \frac{\lambda_0 R}{2L_x} \tag{2.6}$$

Similarly, for a line in the y-direction, the resolution is approximated by

$$\delta_{y(syn)} = \frac{\lambda_0 R}{2L_y} \tag{2.7}$$

Based on the stated diffraction limits (Abbe Limit), it is found that the maximum resolution occurs when $R = L_x = L_y$, which gives a $\lambda_0/2$ resolution.

2.4 Ridge Gap Waveguide Compared with Other Technologies

Ridge gap waveguide is a new technology for implementing devices and antennas at the millimeter band. It is first introduced by Kildal *et.al* [33–35]. It consists of a bed of nails with quarter wavelength height connected to ground, and above it, there is an air gap followed by a metal cover. When a ridgeline is placed between the bed of nails, a quasi-TEM wave can propagate along it.

The operating principle comes from the soft/hard surface concept introduced by Kildal [36, 37]. It states that a corrugated metal surface with a quarter wavelength corrugation height prevents the propagation of electromagnetic waves in the direction transverse to the corrugation. The bed of nails with the ground in the ridge gap case can be considered as a two transverse corrugation, which prevents the propagation of the waves in all directions tangential to the surface of the bed of nails. In order to have a propagating wave among the bed of nails surface, a ridgeline is placed between the nails, and another metal layer is placed on top of the bed of nails, and they are separated by an air gap. This allows a quasi-TEM mode to propagate in the gap between the ridgeline and the upper metal layer. The constraint on the gap height comes from the fact that a bed of nails with a quarter wavelength height and connected by a ground plane forms an artificial magnetic conductor surface. So, to have only a quasi-TEM mode along the ridgeline, the gap height must be less than $\lambda/4$ to have a bandgap structure around the ridgeline. Another constraint comes from the parallel plate mode between the ground of the bed of nails and the top metal, which is that the total height of the nail and the gap must be less than $\lambda/2$. Full analytical analysis of such a structure is in [38], [39] (based on the reflection coefficient from a grounded bed of nails and applying a PEC boundary at a distance from the bed of nail surface). Another solution is presented in [40] using mode matching with cylindrical Bessel functions.

RGW has superior features over other existing technologies. The structure is closed, so there are no radiation losses. Also, the wave propagates in an air gap and hence no dielectric losses for the metal RGW, and it is very small for the PRGW (from the fringing fields inside the mushroom substrate). On the other hand, the conventional microstrip line has radiation losses as it is an open structure. Also, it has dielectric losses as the wave mainly propagates in dielectric material. Another developed technology for millimeter waves is the substrate integrated waveguide (SIW). It is developed as an alternative to the rectangular waveguide but with dielectric-filled and easy to fabricate in the PCB technology. It avoided the radiation losses as it is a closed structure but still have dielectric losses.

A comparison between the three technologies is presented here, where RT600 substrate with a 0.254 mm thickness is used as the main substrate for the microstrip and the SIW structure and also the air gap height in the PRGW is 0.254 mm. In this thesis, the PRGW is used, where it is easy to fabricate with low cost and also compatible with PCB technology, which facilitates its integration with PCB circuits. Figure 2.8 shows the structure of the microstrip line with two bends, an SIW waveguide, and a PRGW. The bends are the source of radiation losses, so they have been considered in the microstrip, which is an open structure. On the other hand, bends are not considered in the SIW and the PRGW as they are closed structures. Figure 2.9 shows the simulated s-parameters for the three technologies where there is good matching. The reason for the deterioration in the matching in the PRGW compared to the other technology is that the PRGW unit cell has periodicity about one-fifth of a wavelength. Therefore, the medium around the line cannot be considered homogeneous, while in the SIW case, the periodicity of the vias is less than a tenth of the wavelength and hence can be considered homogeneous. For the microstrip case, there is no periodicity around the line, and it is pure homogeneous.

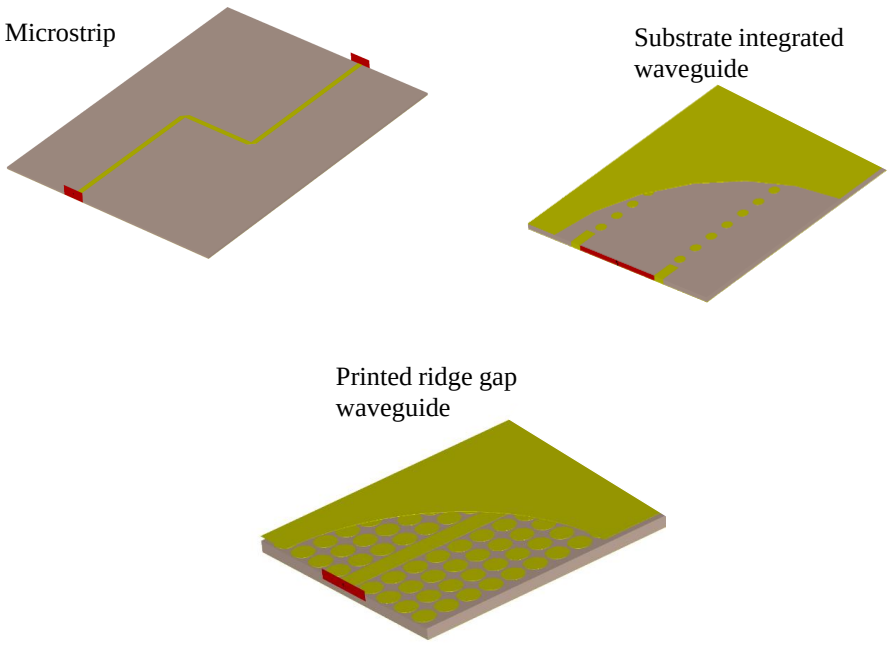

Figure 2.8: The structure of the microstrip line, the substrate integrated waveguide, and the printed ridge gap waveguide

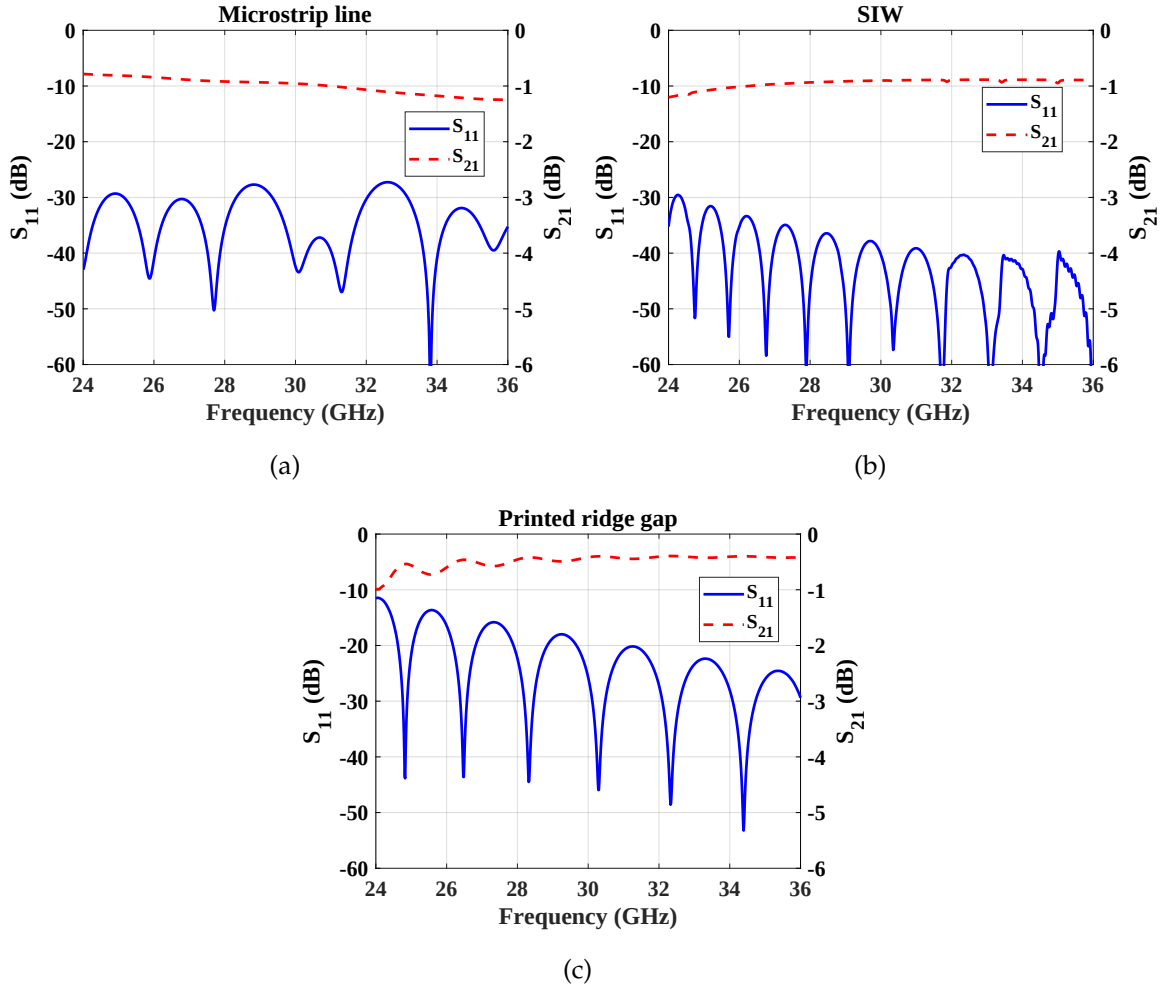

Figure 2.9: The simulated s-parameters of various guiding structure. (a) Microstrip line. (b) substrate integrated waveguide. (c) Printed ridge gap waveguide.

Figure 2.10 (a), (b), and (c) show the metal losses, the dielectric losses, and the radiation losses, respectively in the three technologies. It is clear that the metal losses decrease with frequency as the skin depth decrease, and hence the penetration in the metal is small. It is also noticed that the SIW has the biggest metal and dielectric losses compared to both the MS line and PRGW line, in this case study. The PRGW has the lowest dielectric losses, as the main wave propagates in an air gap region. Considering the radiation losses, the microstrip line has the biggest as it is an open structure, while the SIW and the PRGW are very low and almost near zero because they are closed structure. Figure 2.10 (d) shows the total attenuation coefficient, where it is obvious that the PRGW has the lowest attenuation coefficient.

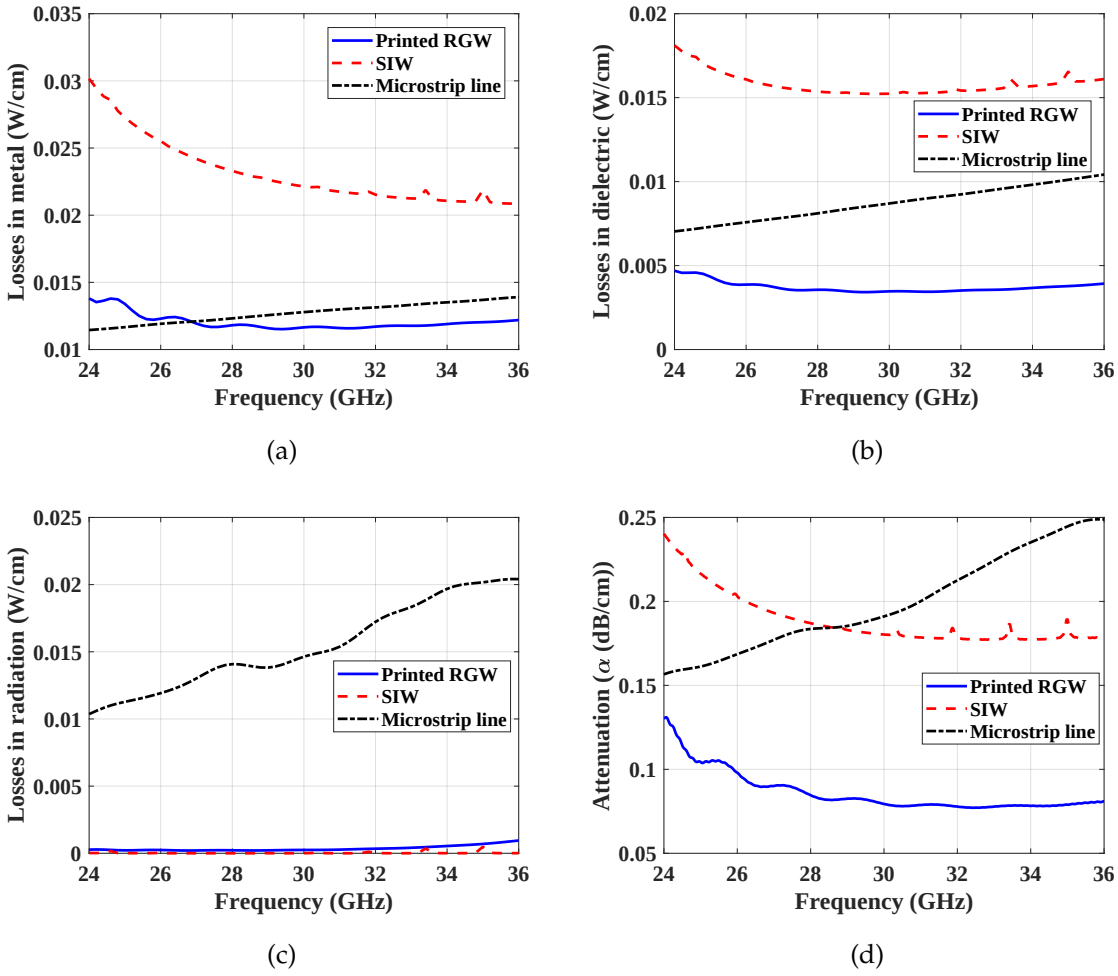

Figure 2.10: Comparison between the losses and attenuation in the microstrip line, the SIW, and the PRGW. (a) Metal losses. (a) Dielectric losses. (a) Radiation losses. (a) Attenuation constant.

2.5 Ridge Gap Feeding: Coaxial to Ridge Gap Transition

The proper excitation of the imaging system components is an important issue. Therefore, a literature review of the excitation of the ridge gap waveguide is presented here. The common technique to excite the ridge gap structure is by inserting a microstrip line in the air gap of the RGW structure. It is used to excite both metal and printed RGW [41–46], but it has a major disadvantage of using an end-launch connector, which has high insertion loss. Another way to excite the RGW is through the use of a coaxial transition. It has been introduced in many configurations, such as half wavelength open circuit [35] and quarter wavelength short circuit [47]. These techniques suffer from a narrow bandwidth and sensitivity for probe position. Broadband transitions are introduced in [47] and [48] using

multi-section matching transformer and fitting parts connected to the RGW. Although this technique has a wide bandwidth performance, it is a bulky structure connected to the microwave devices. Moreover, it is limited to metal RGW structures due to the use of different heights in the transition. Few trials have been done to excite the printed RGW using a coaxial transition, but they have a narrow bandwidth performance [49, 50]. The use of a waveguide to excite the RGW is introduced in [51–53] for metal RGW and in [54] for the printed type. It exhibits a narrow band for printed type and can achieve wideband for the metal type, but it makes the device bulky.

2.6 Transmitting Antenna

Planar antennas with high gain and wide bandwidth are desired in many applications. Moreover, differential feeding antennas are known to have a stable broadside beam and low cross-polarization level. In this thesis, a differential feeding planar antenna is designed. It consists of two parts: the antenna element and the differential feeding network. The antenna is implemented in the printed ridge gap technology and has a planar structure. The differential feeding is achieved by using a modified rat-race coupler. In the following subsections, a literature review about planar antennas and rat-race coupler is presented.

2.6.1 Planar Antenna

Planar antennas have been implemented at the millimeter-wave band in the SIW and the RGW technologies. In SIW, a planar aperture antenna is presented in [55] that is differentially fed and has a measurement impedance bandwidth of 21.5% at 60 GHz and 15.3dB peak gain. However, the SIW suffers from the signal distortion as the main propagating mode is TE_{10}, and also it suffers from dielectric losses. A substrate integrated dual level gap waveguide H-plane horn antenna is presented in [56], where a fan beam is achieved with 8% bandwidth at 61 GHz and a peak gain of 9 dBi. In the PRGW technology, a CP aperture antenna fed by PRGW with a bandwidth of 10% and a peak gain of 13.5 dBi is

presented in [57]. In [58], a 4×4 slot array antenna fed by PRGW is presented. It has an impedance bandwidth of 17% from 55.68 to 65.17 GHz ($S_{11} \leq -10$ dB) with a peak gain of 21.13 dBi. Also, in [J5], a 4×4 cavity slot antenna fed by TE_{10}^{RGW} mode is presented. It has an impedance bandwidth of 7.1% at 33.7 GHz ($S_{11} \leq -10$ dB) and a peak gain of 16.5 dBi.

2.6.2 Rat-Race Coupler

In this section, a brief review of the rat-race coupler is presented. This coupler is used to differentially feed the transmitting antenna. The differential feeding is required as it results in a stable radiation pattern, no beam tilting as in the case of single ended feeding, with a low cross-polarization level over a wide frequency range.

Rat-race coupler has an important role in many microwave circuits. It provides equal power division with in-phase and out of phase characteristics, depending on the feeding port. It is used in mixers and differential feeding network. It has been implemented in different technologies such as microstrip line, substrate integrated waveguide (SIW), and ridge gap waveguide (RGW). Several techniques to improve the bandwidth and reduce the size are used. A 180° phase inverter with only one quarter wavelength section instead of the $3\lambda/4$ branch can be used to reduce the frequency dependency of the rat-race coupler and decrease the size. This technique was first introduced theoretically by S. March in 1968 [59]. Then it has been implemented in the coplanar waveguide [60, 61], finite-ground-plane coplanar waveguide (FGCPW) [62, 63], and inter digit coplanar waveguide [64]. This technique needs a uniplanar waveguide structure that facilitates making the phase inverter either by using bonding wires or conductive tape without increasing the size of the structure. Also, replacing the $3\lambda/4$ by a $\lambda/4$ left-handed transmission line gives the same effect [65–67]. Moreover, lumped elements are used for size reduction by replacing the transmission lines [68–70] or loading the transmission lines and reduce their electrical length [71]. Also, slow-wave waveguides have been used to reduce the size as in [72, 73]. Finally, cascading of rat-race couplers is used to have a wideband as

in [74]. These techniques are valid for low operating frequencies as there is enough area to build a left-handed transmission line, slow-wave structures, or to use lumped elements. However, at high frequencies, the devices become very small, and there is no enough area to build artificial transmission lines or to use lumped elements with the current PCB technology.

For high frequency devices, new guiding structure technologies such as substrate integrated waveguide (SIW) and ridge gap waveguide are considered. The SIW has been used to build a rat-race coupler [75]. However, as the propagating mode is TE_{10} and the width of the waveguide is large, the $\lambda/4$ section cannot be realized, and $5\lambda/4$ is used instead. This increases the frequency dependency of the structure, and the bandwidth is only 10%. Then it has been optimized in [76] to reach 30%. Several techniques have been used to reduce the overall size of the SIW rat-race, such as using half mode SIW [77], folded SIW [78] or ridge SIW with slow-wave [79]. All of these works suffer from dielectric losses in SIW technology. Considering the ridge gap waveguide, to the authors' best knowledge, only one article has been found [80] in metal RGW technology and using conventional rat-race with only 12.1% bandwidth around 16.5 GHz.

2.7 Beamforming Network

Generally, beamforming is used to surveillance a wide angular sector with the resolution of a narrow beam [81]. It is defined as the shaping of the beam to point to a specific direction, and it is also called spatial filtering. The device that produces the excitation to an array of antennas is called a beamforming network, as shown in Figure 2.11. There are lots of beamforming networks for millimeter-wave applications. They are divided into two categories: the active beamforming networks and the passive beamforming networks. The active beamforming is like the phased array in which there are many controllers to control the phase and amplitude of each element. The Passive beamforming is like the Butler Matrix, Nolen matrix, Blass matrix, Ruze lens, and Rotman lens.

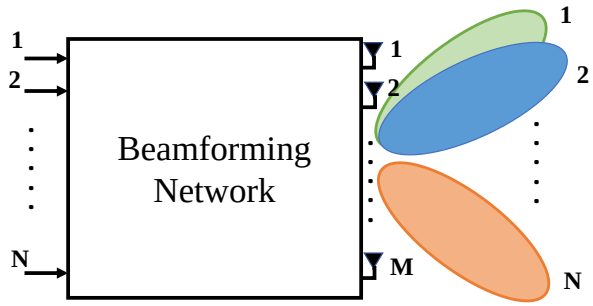

Figure 2.11: General Beamforming Network

Ruze and Rotman are lens-based beamforming networks. Ruze [82], in 1950, proposed a set of lenses for beamforming. The main idea is to have a parallel plate waveguide and putting a source at the focal point of a lens to illuminate an array of antennas (it has its basis in the optics). The most important property of the Ruze lens is the true time delay nature of it (the scanning angle does not depend on frequency). It has the constraint that the output lines are parallel to the lens axis, which leads to having only two focal points. After that, Rotman in 1963 [83] proposed a new parameter by removing the constraint of having the output lines parallel to the lens axis (this lens design is called the Gent model). Rotman lens has the inputs on a circular arc of radius R, and its output lines have variable lengths. The added parameter allows making the design for three focal points, which decrease the phase error. It originally has the beam directed at an angle equals to the focal point angle ($\psi = \alpha$). After that, a general formula ($\psi \neq \alpha$) has been developed in [84]

The Blass, Nolen, and Butler are matrix-based beamforming network. The Blass matrix was developed in 1958 [85]. It uses a set of couplers, phase shifters, and matched loads [85, 86]. It consists of rows and columns. The number of rows determines the number of output beams, while the number of columns determines the number of antenna elements. The output beams are orthogonal, which means that the beams are independent. The disadvantage of the Blass matrix is the use of the matched load as there is a loss in the power delivered to the antennas. Also, the design is hard, as the excitation ports must feed simultaneously to have the desired beam [86] (a single port cannot give

the desired beam as in Butler Matrix). Moreover, the design is complicated, as it contains a lot of couplers with different values of coupling and a lot of phase shifters with different values. It needs $n \times m$ couplers and $n \times m$ phase shifters, where m is the number of inputs and n is the number of antennas. The advantage of the Blass matrix is that it can produce simultaneous beams, and the number of antennas can be bigger than the number of inputs and hence can achieve a high gain. In 1965, J. Nolen developed the Nolen matrix. It is a Blass matrix with the diagonal couplers are replaced by bend connections, and the down diagonal couplers are removed. In fact, Nolen matrix has the same design procedure as the Blass matrix with the advantage of being lossless, as all the matched loads are removed. Also, Nolen and Blass matrices are series feed networks that avoid the use of crossovers. However, they have the disadvantage of being a narrow band.

2.7.1 Butler Matrix

The Butler matrix was introduced in 1961 by Butler [87]. It has a wideband behavior compared to Blass and Nolen matrices. It is also known to be the matrix with the fewest number of components. It has a power of 2 inputs and outputs (2^n). The number of components in a Butler matrix is $\frac{N}{2}\log_2(N)$ directional coupler and $\frac{N}{2}(\log_2(N)-1)$ phase shifter [88]. It provides a constant phase difference between radiating elements (the phase difference is calculated as $\Delta\phi = \frac{2n-1}{N}180^\circ$ where n=1,2,..,N.). The array factor of the output beams is [89]

$$\frac{\sin\left(\frac{N\pi d}{\lambda_0}\left(\sin\theta - \frac{(2n-1)\lambda_0}{2Nd}\right)\right)}{N\sin\left(\frac{\pi d}{\lambda_0}\left(\sin\theta - \frac{(2n-1)\lambda_0}{2Nd}\right)\right)} \tag{2.8}$$

where θ is measured from the broadside direction, d is the antenna spacing, and λ_0 is the free space wavelength. The structure for a 4×4 matrix is shown in Figure 1.1. Also, a systematic design procedure for $N \times N$ matrix is in [90]. The disadvantage of the Butler matrix is that the beam direction is not fixed with frequency even if there are wideband phase shifters, contrary to the Ruze and Rotman lenses, where the beam direction is independent of the frequency.

Butler matrix has been implemented in different technologies (microstrip, rectangular waveguide, SIW, and RGW) and at different frequency bands. It has two main configurations: the 1-D scanning [87, 91] as in Figure 1.1, where the beam is steered in only one direction, and the 2-D scanning [92–94] as in Figure 2.12, where the beam is steered in two dimensions. The performance of the Butler matrix is determined by several factors, namely the matching, isolation, amplitude imbalance, and phase error.

In the millimeter-wave band, the Butler matrix has been implemented in several technologies with different configurations. In [95], a 4×4 1-D Butler matrix is implemented in the SIW technology and has a bandwidth of 6.67% around 60 GHz. Also, it has a phase error of $\pm 24^{\circ}$ with a high insertion loss of 2.5 dB. Another Butler matrix in the SIW technology is in [96], where it is 4×4 1-D with a bandwidth of 7.15 % around 28 GHz. A 2-D Butler matrix in the SIW technology is presented in [97]. It has a bandwidth of 13.33% around 30 GHz with an amplitude imbalance of ± 2 dB and a phase error of $\pm 18^{\circ}$. Another 2-D Butler matrix in the SIW technology is reported in [92]. It has a bandwidth of 27%, around 60 GHz. However, the structure is bulky, as it has two layers, and the radiation efficiency is only 80 %. The main limitation of these structures is the high insertion loss due to the dielectric losses in the SIW technology.

In the microstrip technology, an 8×8 Butler matrix is presented in [98] where the bandwidth is 4% around 25 GHz, and the phase variation is $\pm 7.7^{\circ}$, with an output amplitude variation less than 1 dB around -10 dB. Another 4×4 microstrip Butler matrix is in [99], where it has a bandwidth of 4.9 % around 60 GHz. In addition, a 2-D microstrip Butler matrix is reported in [94], where it has a bandwidth of 17% around 2.4 GHz with an amplitude imbalance of ± 1.2 dB and a phase error of $\pm 7^{\circ}$.

Other modern technologies like substrate integrated suspended line technology is used in [100] to build a 4×4 Butler matrix with a bandwidth of 7.85% around 25.5 GHz. In [101], an integrated PTFE-based waveguide 4×4 Butler matrix at 180 GHz is implemented using X-ray lithography, sputter deposition of metal, and electroplating. Also, in [102], an inverted microstrip gap waveguide Butler matrix is presented with a 5.26% bandwidth at 57 GHz.

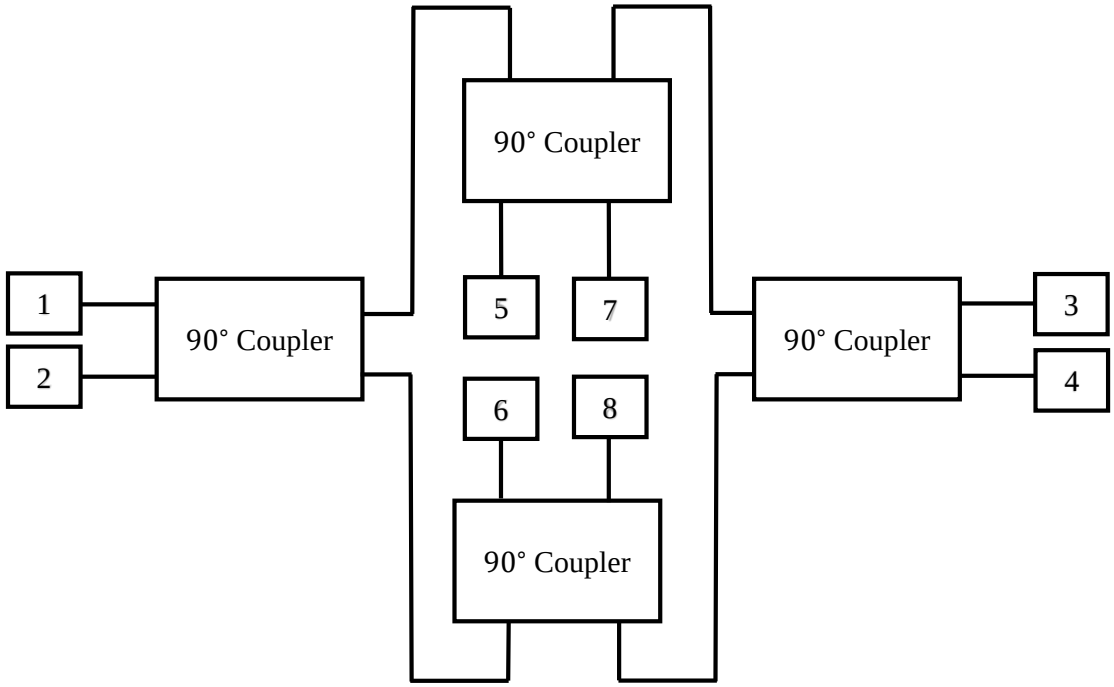

Figure 2.12: 2D scanning 2 × 2 Butler matrix

The standard 1-D Butler matrix cannot originally produce a broadside beam, has high sidelobe level, and has a low gain. However, in [103], a modified Butler matrix is presented with a broadside beam using a tapered line coupler to produce output phase differences of 0°, ±90°, and 180° [103] instead of ±45° and ±135°, which are produced by the conventional 1-D Butler matrix. A method to increase the gain is in [104], where a microstrip 8 × 16 Butler matrix is reported in which an increase in the gain is achieved by increasing the number of radiation elements. This is done by introducing the use of a rat-race coupler at the end of the conventional 8 × 8 Butler matrix, but the bandwidth is narrow (from 9.3 -9.5 GHz), and there is a need for many crossovers. Another method to increase the gain is in [105], where a horn antenna fed by 60 GHz Butler matrix in the microstrip technology is used to increase the gain of a conventional 4 × 4 Butler matrix to 13.4 dBi. It has a wide bandwidth of 24.3 %, but the insertion loss is high, and the output phase error is ±20°. In [106], a microstrip 4 × 4 Butler matrix with low sidelobe level is presented with a bandwidth from 27.525 to 28.325 GHz. The sidelobe level reduction has been achieved using amplitude tapering of the output ports by adding couplers and matched loads at the outer output ports. Another way for sidelobe reduction is in [107],

where the modified 4 × 4 Butler matrix is used with unequal power dividers at the output ports to perform amplitude tapering over 8 output ports. In addition, in [108], a 2-bit phase shifter is added to the output ports to increase the scanning range. Also, in [91], a dual-polarized 4 × 4 Butler matrix is presented in the rectangular waveguide technology with a bandwidth of 6.67 % around 60 GHz.

In this thesis, we focus on the 1-D scanning Butler matrix, which is used in the proposed imaging system. Therefore, the following subsections present literature reviews of the components of the Butler matrix (3-dB coupler, crossover, and 45° phase shifter).

2.7.2 3-dB Directional Coupler

The directional coupler is an essential component in microwave circuits and beamforming networks. It is used to divide the power between two output ports with a 90° phase shift between them. Also, it can be used with dual-polarized antennas to have Left-hand circular polarization (LHCP) or right-hand circular polarization (RHCP)

The conventional branch line directional coupler in [109] has a small bandwidth. A modification is introduced in [110] by using two quarter wave sections to have wider bandwidth (about 50%), but the amplitude imbalance increases compared to the conventional one. Besides, the technology used is the microstrip technology, which has dielectric losses and radiation losses. Moreover, the device needs high and low line impedances, which introduces fabrication problems (40 Ω to 120 Ω). Another wideband coupler with a minimization technique is reported in [111], where the author uses two quarter wave sections as his first step and then loads them by capacitors to reduce the length of the lines and hence minimize the whole device. A bandwidth of 68% at 3.5 GHz is achieved, but the device is implemented with microstrip technology and needs a space for the use of capacitors. Therefore, it is not suitable for the millimeter-wave range, as the wavelength is very small, and there are no rooms for the capacitors introduced in the design. Using quarter wave transformers at all the ports of a conventional branch line direction coupler is presented in [112] for coupling of 10 dB and shows a fractional bandwidth of 50.9%.

It shows that the matching can be sacrificed for an increase in the bandwidth. In [113], a 3 dB coupler is designed using suspended and normal microstrip lines and reaches 49% bandwidth at 6 GHz, but it has the disadvantage of using the suspended part, as it makes the device bulky. A slot coupler is presented in [114] with an ultra-wideband performance from 3.1 to 10.6 GHz and output amplitudes of 3 ± 0.75 dB. However, it uses two layers and built-in microstrip technology, which has a lot of losses. In [115, 116], a PRGW coupler using 6 slots between two PRGW lines flipped to face each other is presented, but the device is bulky, and the bandwidth is narrow (11.5 %). In [117], a directional coupler at 60 GHz is presented in the microstrip RGW technology, but it has a narrow bandwidth of 11.5%. A directional coupler built in the metal RGW at 15 GHz is presented in [118], where a 16.6% bandwidth has been achieved. However, the device is only suitable for bulky structures, as a matching spherical cap is used. Printed RGW couplers are presented in [119] and [93] with a narrow bandwidth ($\leq$ 12%).

2.7.3 Crossover

Crossover is an essential component in microwave circuits. It is used to allow the crossing of two transmission lines carrying different signals while maintaining high isolation between them [120]. There are two main approaches to realize a crossover. The first one is to have two layers of guiding structures in which one signal passes from the first layer to the second layer and then returns back after a distance while the other signal passes directly. The second approach is to have the crossover built within one the layer of guiding structure. In this thesis, the planar crossover is used to avoid having a bulky structure and to reduce the cost of the fabrication.

Crossover has been implemented in different technologies. In [120], a wideband crossover built in the microstrip technology is presented, and a bandwidth of 44% around 2.8 GHz is achieved using a combination of a ring resonator and a circular patch. However, the return loss is near 10 dB, which is not good when integrated with other components. Also, in [121], a similar structure is reported in the millimeter-wave band around 30 GHz using

slotted SIW structure. However the bandwidth is only 16.7% (with return loss better than 14 dB), and the size is large ($1.2\lambda_g \times 1.2\lambda_g$). Another crossover built in the SIW technology is reported in [122], where 17.1% bandwidth around 35 GHz (20-dB return loss and isolation) is achieved, but the insertion loss is 0.9 dB, which is quite high, and the device is built in two layers (bulky). Moreover, in [123], a planar crossover in the SIW technology is presented with a 10.5 % bandwidth, which is quite low. The crossover has been recently implemented in the PRGW technology. In [124], a PRGW crossover is presented at 30 GHz where the size of the crossover is $1.5\lambda_0 \times 1.5\lambda_0$ (this includes the first two rows of cells around the middle junction), and the bandwidth is 13.33% with 0.5 dB insertion loss. Another PRGW crossover is in [49], where a bandwidth from 12.3 to 16 GHz (26%), and return loss and isolation better than 13 dB and 19.5 dB, respectively, are obtained. However, the device has a very large size of $5.183\lambda_0 \times 2.143\lambda_0$.

2.7.4 45° Phase Shifter

The phase shifter is an important component in most matrix-based beamforming networks [86,87,125]. Also, it can be used with T-junction to provide a wideband phase shift between the output ports. There are two types of phase shifter: 1) active phase shifter with a variable phase difference, 2) passive phase shifter with a fixed phase difference.

The active phase shifter can be achieved by using varactors with a directional coupler as in [126, 127] (reflective type phase shifter) or using MEMS (changing position of a dielectric block near the guiding structure) as in [128]. Also, the use of piezoelectric transducers for phase shift is presented in [129] and [130]. The active phase shifter can achieve a wide bandwidth with a variable phase shift but needs external controllers to bias the structure.

The passive phase shifter has been implemented in the MMW band in different technologies. In the SIW technology, a phase shifter using two post pins has been reported in [131], with a bandwidth of 0.35% and a phase error of $\pm 3^\circ$ at 28 GHz. Another SIW

phase shifter is in [132], where air holes are used to introduce the phase shift. The structure has a stable phase difference and has 20% bandwidth around 36 GHz, but the insertion loss is about 0.7 dB due to some radiation losses from the air holes. In [133], an RGW 90° phase shifter is presented using ferrite material, and a bandwidth of 16.67% around 30 GHz is achieved with a phase variation of 10°. In this thesis, the whole beamforming system is passive; hence our focus is on the passive phase shifter at the millimeter-wave band.

2.7.5 Receiving Antenna

The radiating element of the Butler matrix must have a wide bandwidth and a wide beamwidth. In this thesis, an end-fire antenna is considered as the beam direction, and radiation patterns are stable over a wide frequency range. Yagi-Uda, Vivaldi, log-periodic, and tapered slot antenna are the most common types of end-fire antennas.

In [134], a Yagi-Uda antenna with one director and one reflector is presented. It has a wide bandwidth from 2.8 to 5.2 GHz and gain between 4 and 5 dBi. In [135], a bandwidth of approximately 41.4% and a maximum gain of 7.2 dBi have been achieved at 1.45 GHz using two feed dipole antennas and also one reflector and one director. A Yagi-Uda antenna with bowtie shape dipole and one reflector and one director at the center frequency 1.29 GHz is presented in [136]. It has a bandwidth of 18.6% and a peak gain of 6.4 dBi. In [137] a microstrip Vivaldi antenna with a wide bandwidth from 3.4 GHz to 10.2 GHz and gain around 10 dB is presented.

In the millimeter-wave band, several end-fire antennas have been designed in the microstrip, SIW, and RGW technologies. In [138], a microstrip Yagi-Uda antenna at 24 GHz is presented with a bandwidth of 16.6% and a gain of 10.4 dBi. Also, a logic periodic antenna is presented in [139] with a peak gain of 12.64 dBi and 68% impedance bandwidth at 62 GHz. Moreover, a Quasi-Yagi antenna is presented in [J6], which has a bandwidth from 26 to 40 GHz and an average gain of 7 dBi. In the SIW technology, a printed log-periodic dipole antenna fed by half mode substrate integrated waveguide is designed

in [140] with an impedance bandwidth from 3.1 GHz to 10.6 GHz (VSWR less than 2). Also, in [141], a log periodic antenna fed by SIW is presented with a peak gain of 8.1 dBi and an impedance bandwidth from 26 to 40 GHz ($S_{11} \leq -10$ dB). In the metal RGW, a Vivaldi antenna is presented in [142], where a gain of 7 dBi is achieved with 35% impedance matching bandwidth ($S_{11} \leq -10$ dB) at 30 GHz. Most of these antennas have the disadvantage of using the microstrip or SIW technologies, which are lossy at millimeter-wave bands. Besides, the Vivaldi antenna presented in the RGW technology is expensive as it requires two CNC machining layers.

Chapter 3

30 GHz Imaging System: Printed Ridge Gap Components

In this chapter, the proposed imaging system is presented in detail with the associated hardware requirements. The active imaging with synthetic aperture technique is used as it is appropriate for high quality imaging of close distance objects. This allows the use of small antennas with low gain to image an area and hence reduce the cost and the complexity of the system. The system hardware requirements are calculated based on Abbe limit and the synthetic aperture equations in the previous chapter. After that, the building of the millimeter-wave components of the imaging system is presented. Afterward, the components used for building the imaging system are designed in the PRGW technology: 1) the coaxial to ridge gap transition, which is used for feeding the structures, 2) the directional coupler, 3) the phase shifter, 4) the crossover, and 5) the rat-race coupler.

3.1 System Overview

Before going to the proposed system, it is worth knowing that most imaging systems for security applications such as personal screening have an imaging area of 2 $m \times 1$ m [14]. In a conventional backscattering imaging system, the imaging area is the same as the scanning area as seen in Figure 3.1. The transmitting and receiving antennas are coincided with each other and moving in a 2D plane to perform a raster scan of the imaging

area. Therefore, in the proposed imaging system, we set $d = L1$ for maximum resolution. The problem with the conventional method is that for scanning a 2 $m \times 1$ m area, a long time is required to complete the scan. So, we proposed a method to reduce the scanning area to half and hence reducing the scanning time. This is done by using offset scanning, as illustrated in Figure 3.2, in which the transmitting and receiving antennas are separated from each other (also called bi-static imaging). The transmitting antenna is fixed away from the receiving antenna to illuminate an offset spot of the imaging area (black and orange area in Figure 3.2) while the receiving antenna is moving in a scan area of 1 $m \times 1$ m to collect the reflected and scattered signals. It is shown that using only two transmitters cannot cover the whole area, so we proposed using four transmitters, as shown in Figure 3.3 to illuminate the imaging area. It is clear that by appropriate positioning of the transmitters, an area double the scanning area is covered, which meets our purpose. Now, four transmitters illuminate the imaging area, and each one is responsible for illuminating a certain area. Hence, it is better for the receiving antenna to be able to capture the signal from each transmitter alone without the interferences coming from the other transmitters. Therefore, a four switchable beam antenna is required in the receiving antenna to cover the four parts of the imaging area separately and hence reduce the interference and noise in the received signal. Thus, the signal to noise ratio is increased and hence the produced image quality. In the proposed work, a 4×4 Butler matrix is selected for this task for its advantages over other beamforming techniques, as will be discussed in the next chapter. For the other direction (y-direction), an imaging area equal to the scanning area is required, and hence only two transmitters are used to illuminate the imaging area, as shown in Figure 3.4. Moreover, each transmitter operates at a different frequency to ensure isolation between the imaging sections. It is worth noting that the spatial multiplexing produced by the use of the Butler matrix is still in need as there are background radiation and the blackbody radiation from the imaging objects that are needed to be suppressed.

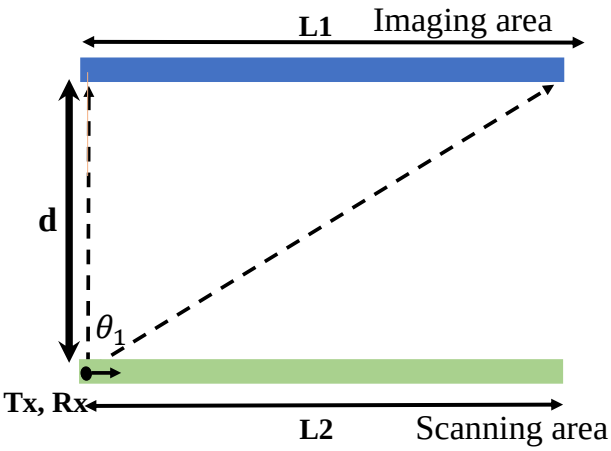

Figure 3.1: Conventional mono-static imaging where the imaging area is the same as the scanning area.

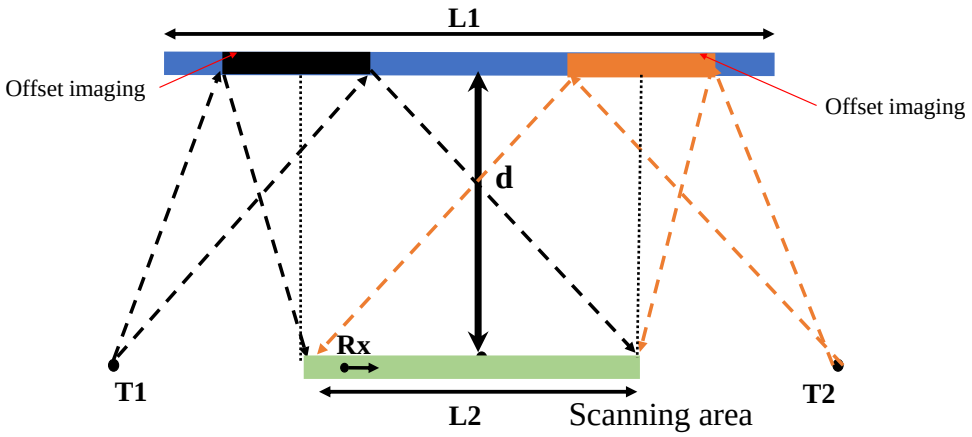

Figure 3.2: Offset imaging by separating the transmitter and receiver antennas from each other.

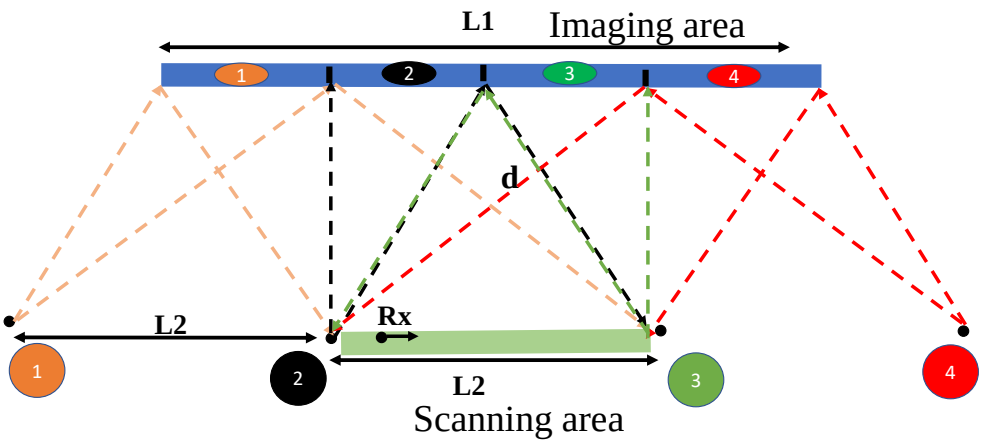

Figure 3.3: Proposed wide-view angle imaging system.

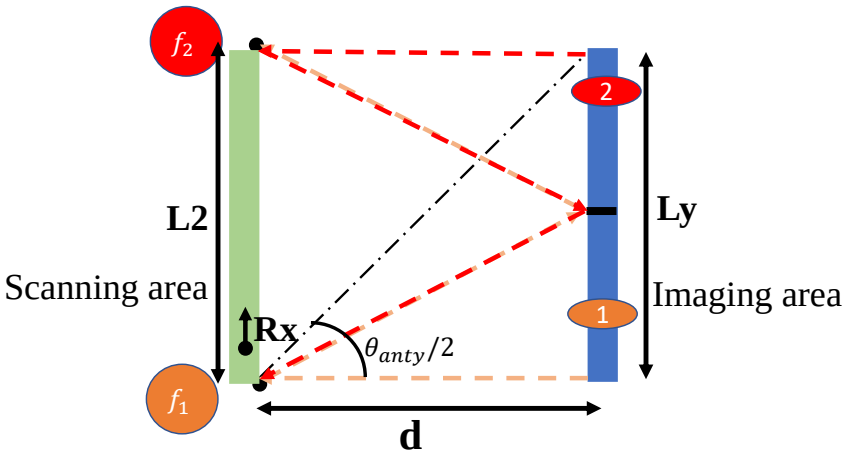

Figure 3.4: Proposed imaging system set up in the y-direction using two transmitting antennas working at different frequencies.

3.2 Hardware Requirements

The millimeter-wave components and antennas are designed in PRGW technology. Two antennas are to be designed for the proposed imaging system. The first one is that of the receiving antenna, and the requirements for it are calculated from the proposed system Figures 3.4 and 3.5 as

$$\theta_{antx_r} = 2\tan^{-1}(1.5) = 112.6^\circ \tag{3.1}$$

$$\theta_{anty_r} = 2\tan^{-1}(1) = 90^\circ \tag{3.2}$$

where θ_{antx_r} and θ_{anty_r} are the receiving antenna beamwidths in the x and y-axes, respectively. For the transmitting antennas used for illumination, the required beamwidth is

$$\theta_{ant_t} = \tan^{-1}(0.5\sqrt{2}) = 35.26^\circ \tag{3.3}$$

where θ_{ant_t} is the beamwidth of the transmitting antenna. The extreme case for all the transmitting antennas is considered in the calculation.

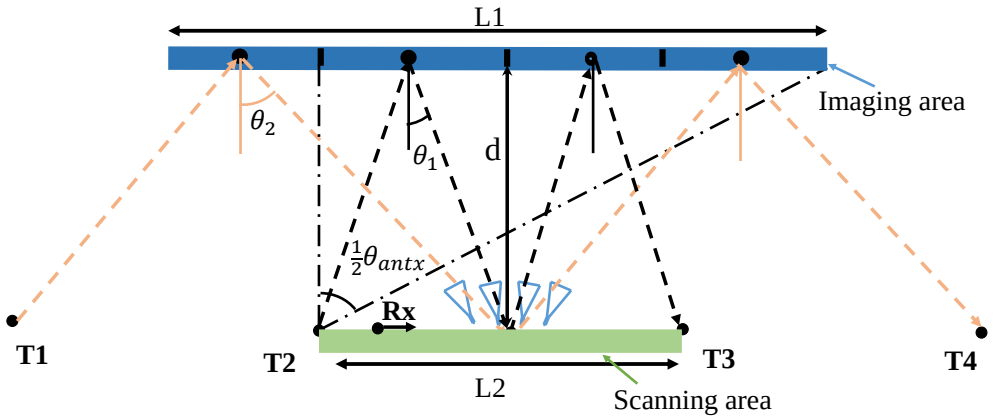

Figure 3.5: Required angles of the beamforming network and the receiving antenna beamwidth in the x-direction.

Table 3.1 shows the required angles for the beamforming network of the receiving antenna (θ_1 and θ_2 in Figure 3.5) along with that produced by a 4×4 Butler matrix with $0.6\lambda_0$ spacing between antenna elements. The beam angles produced by the Butler matrix are in a good agreement with the required beam angles.

Table 3.1: The required beam directions and the beam direction produced by a Butler matrix with $0.6\lambda_0$ spacing.

	Beam # 2, 3	Beam # 1, 4
Required beam angles	$\pm 11.25^\circ$	$\pm 36.875^\circ$
Realized beam angles by Butler matrix with $0.6\lambda_0$ spacing	$\pm 12^\circ$	$\pm 38^\circ$

3.3 Coaxial to Ridge Gap Transition

In this section, the analysis and design of a wideband coaxial to ridge gap transition are presented. The proposed transition is featured with: compact size, wide bandwidth, and simple structure. It can be used to excite ridge gap waveguides fabricated with the printed circuit board (PCB) or computer numerical control (CNC) technologies. A circuit model similar to that of the coax-to-microstrip junction is proposed and used to have a systematic design procedure for the transition. First, perfect electric conductor (PEC) and perfect magnetic conductor (PMC) boundaries are used to making the procedure applicable for any fabrication technology. Second, the PMC is replaced by a bed of nails

for the ridge gap realized by CNC technology and a mushroom-shaped structure for the ridge gap realized by PCB technology.

The aim of this work is to design a wideband coaxial to RGW transition based on a systematic design procedure. The design procedure is validated for both metal and PRGW. A wideband performance has been achieved with a compact size. The transition can be integrated with other microwave components with a low cost while covering the possible operating bandwidth of RGW (usually an octave frequency range). In the following subsections, the design procedure of the transition is presented, followed by the implementation of the transition in the metal and PRGW structures.

3.3.1 Systematic Design Procedure

The transition from a coaxial line to RGW structure is designed in three steps as follows

1. A circuit model for the direct connection between the coaxial and the RGW using ideal boundary conditions (PEC and PMC boundaries) to make the design independent of the implementation technology.

2. A matching technique is used to increase the operating bandwidth.

3. The PMC boundary is replaced by bandgap unit cells designed to cover the operating frequency band.

4. An optimization process is performed to achieve a better matching level

3.3.2 The Circuit Model for The Coaxial to RGW Transition

The design starts by examining the direct connection between a coaxial line and an RGW line, as shown in Figure 3.6 (a). The width of the ridgeline (W=1.75 mm) and the air gap height (h=0.289 mm) are chosen to achieve a 50 Ω characteristics impedance that to be matched with a standard 50 Ω coaxial line. The connection is similar to the coaxial to microstrip line connection, so it can be modeled by a π-circuit as shown in Figure 3.6 (b) [109](two capacitors ($C/2$) and one inductor (L), the inner conductor of the coaxial line

acts as an inductor, and the outer radius of the coaxial line with the top ground acts as a capacitor). The π-circuit parameters are extracted from simulating the direct connection between the coaxial and the RGW in high frequency structure simulator (HFSS) with perfect boundary conditions. The reflection coefficient, obtained from HFSS simulation, is used to calculate the input impedance $Z_{in\ simulation}$ as follows [109]:

$$Z_{in\ simulation} = Z_0 \frac{1 + S_{11}}{1 - S_{11}} \tag{3.4}$$

The input impedance for the circuit model (Figure 3.6 (b)) can be expressed as

$$\begin{aligned} Z_{in\ model} &= \left(Z_0 \| \left(\frac{1}{j\omega C/2} \right) + j\omega L \right) \| \left(\frac{1}{j\omega C/2} \right) \\ &= \frac{Z_0(1 - \frac{\omega^2 LC}{2}) + j\omega L}{(1 - \frac{\omega^2 LC}{2})(1 + j\frac{\omega C Z_0}{2}) + j\frac{\omega C Z_0}{2}} \end{aligned} \tag{3.5}$$

where ω is the angular frequency and $Z_{in\ model}$ is the input impedance of the circuit model. By equating the input impedance of (3.4) with the input impedance of the circuit model (3.5), the values of the capacitance (C) and inductance (L) of the π-circuit model shown in Figure 3.6 (b) can be obtained. As there are two equations (one for the real part and the other for the imaginary part) and two variables (L and C), the equations are consistent, and there is only one solution.

Figure 3.7 shows the obtained capacitance and inductance of the circuit model. It can be seen that they are stable in the region from 30 to 45 GHz. By choosing the values at the center frequency (33.5 GHz), the obtained capacitance and inductance are C=0.043 pF, and L=0.0605 nH, respectively. Figure 3.8 shows the agreement between the reflection coefficient obtained from the π-circuit model and that from the simulator.

In order to improve the impedance matching even further, the input impedance of the direct connection is investigated. The real and imaginary parts of the input impedance are shown in Figure 3.9. Since the reactance part is capacitive, an inductive element is required to have a pure real impedance that can be easily matched with the 50 Ω coaxial

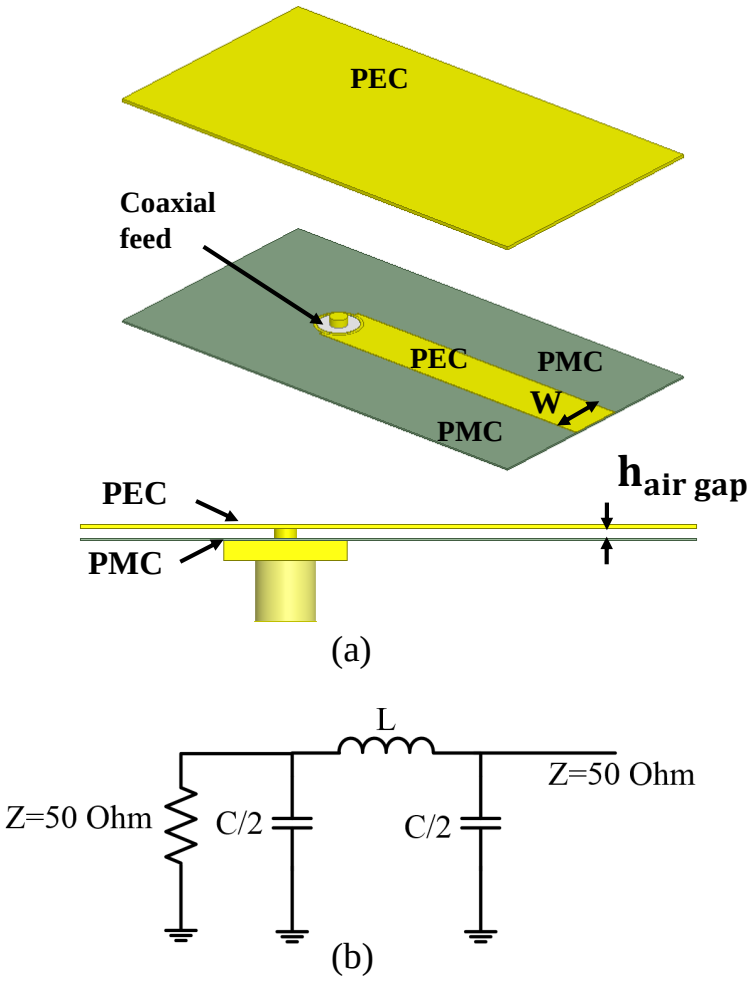

Figure 3.6: (a) Coaxial to ridge gap transition in HFSS using perfect magnetic conductor boundary condition. (b) The π-circuit model of the direct connection between the coaxial and the RGW. (Islam Afifi et al [J1], ©2018 IEEE.)

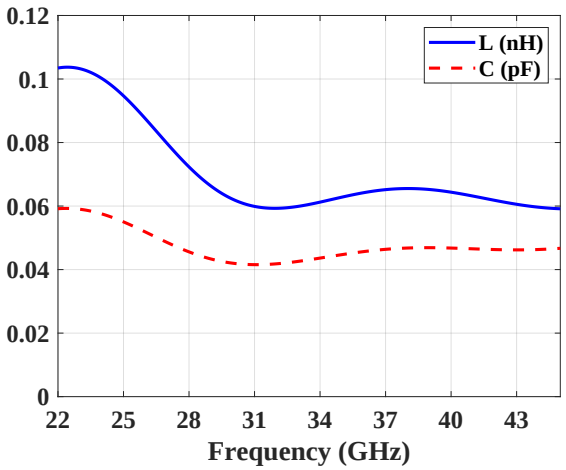

Figure 3.7: The capacitance and inductance of the π-circuit model obtained using the s-parameters from the HFSS simulation. (Islam Afifi et al [J1], ©2018 IEEE.)

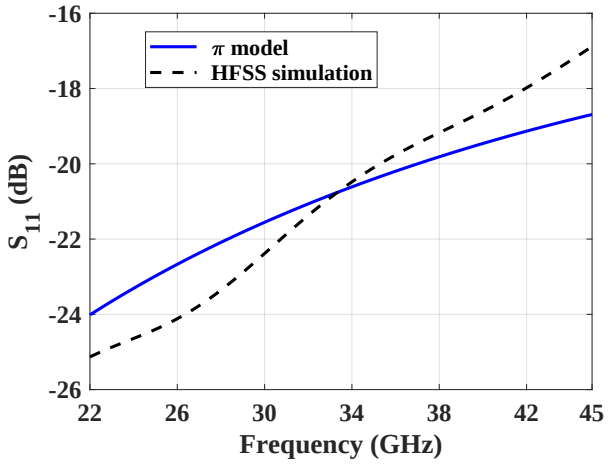

Figure 3.8: Comparison between the s-parameter obtained from theπ model with that obtained from HFSS simulation. (Islam Afifi et al [J1], ©2018 IEEE.)

line. In addition, since the value of the real part of the impedance is declining with the frequency, an inductance and a tapered matching section are added to have a matched transition with 50 Ω ridgeline impedance, making the proposed transition compatible with most of the microwave components.

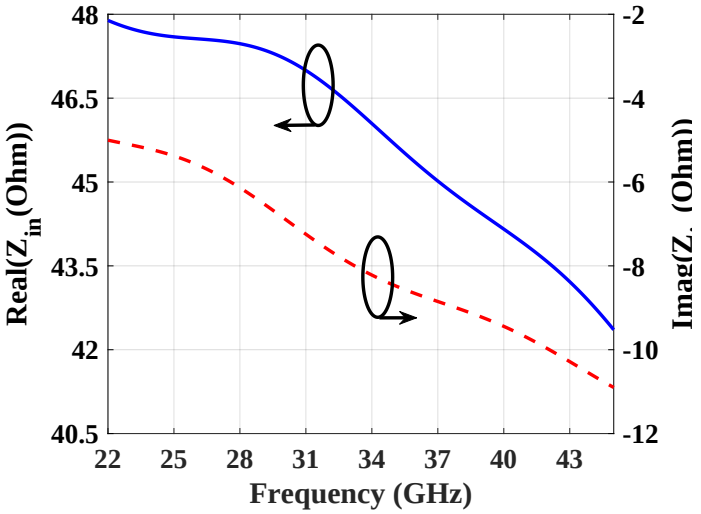

Figure 3.9: Real and imaginary part of the input impedance of the direct connection between coaxial and the ridge. (Islam Afifi et al [J1], ©2018 IEEE.)

The circuit model with the added parallel inductor (L_2) is shown in Figure 3.10. Note that the tapering section is not considered here for the simplicity of the circuit model. The

new input impedance $Z_{in\ total}$, after adding L_2 (Figure 3.10) becomes:

$$Z_{in\ total} = j\omega L_2 \| \frac{Z_0(1-\frac{\omega^2 LC}{2}) + j\omega L}{(1-\frac{\omega^2 LC}{2})(1+j\frac{\omega C Z_0}{2}) + j\frac{\omega C Z_0}{2}} \tag{3.6}$$

Here, the value of L_2 is optimized to minimize the reflection coefficient Γ which can be expressed as:

$$\Gamma = \frac{Z_{in\ totoal} - 50}{Z_{in\ total} + 50} \tag{3.7}$$

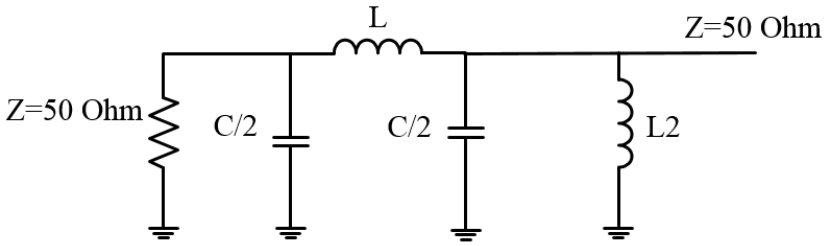

Figure 3.10: The circuit model of the direct connection with the added parallel inductor (L_2.) (Islam Afifi et al [J1], ©2018 IEEE.)

The conventional way to add a parallel inductance to a transmission line is through adding a shorted stub with a certain length. This technique produces an inductance that is changing with frequency and will limit the bandwidth of the proposed transition. In the proposed work, vias around the line are used to act as inductors to avoid such limitations. The value of the inductance depends on the radius and the height of the vias. Since the height is fixed in this work, the radius of the vias is the parameter that can be used in the optimization. Another parameter is the position of the vias with respect to the ridgeline, as the field is decaying away from the ridgeline (see Figure 3.19 for the printed ridge gap case). These two parameters are used in the optimization process to have a good matching.

3.3.3 Proposed Transition Structure

A good matching level transition is required to excite the RGW. By using a single connection with perfect boundary conditions, the matching level in the direct connection

approach -17 dB in the frequency band from 22 to 45 GHz. For a back-to-back configuration, the matching level will degrade further. Moreover, by replacing the PMC with the bandgap unit cells, the matching level becomes even worse. In this subsection, $S_{11} < -20$ dB over the whole frequency band is achieved in the ideal case. Therefore, when realizing the transition, it reaches an acceptable range of about -15 dB.

Figure 3.11 shows the total proposed transition in which a matching section and vias are used. Figure 3.12 depicts S_{11} results from HFSS along with that of the direct connection with/without parallel inductance, where $L_2 = 1.3$ nH is the optimum value for a good matching level. It is clear that the matching bandwidth ($S_{11} < -20$ dB) is wider, and the matching level is improved, especially at higher frequencies. As the principle of operation has been elaborated in the ideal case with PEC and PMC boundaries, the implementation of this transition in metal RGW and PRGW is presented in the following sections.

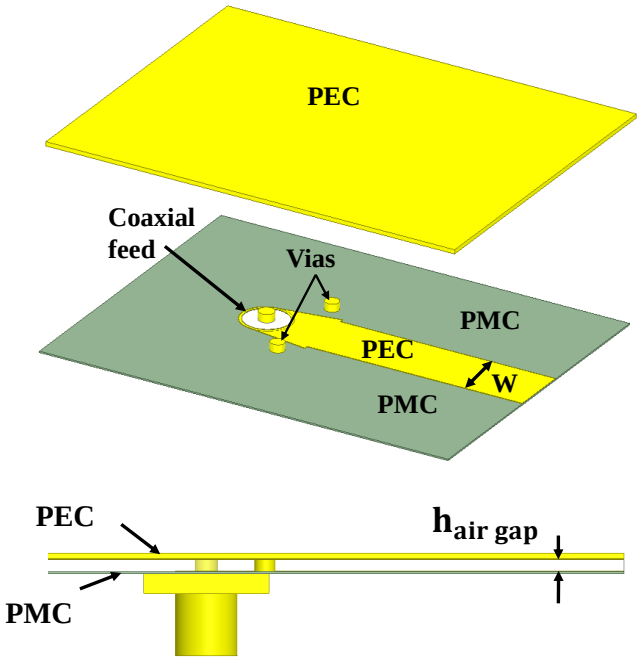

Figure 3.11: The geometry of the proposed transition with a tapered matching section and vias around the line. (Islam Afifi et al [J1], ©2018 IEEE.)

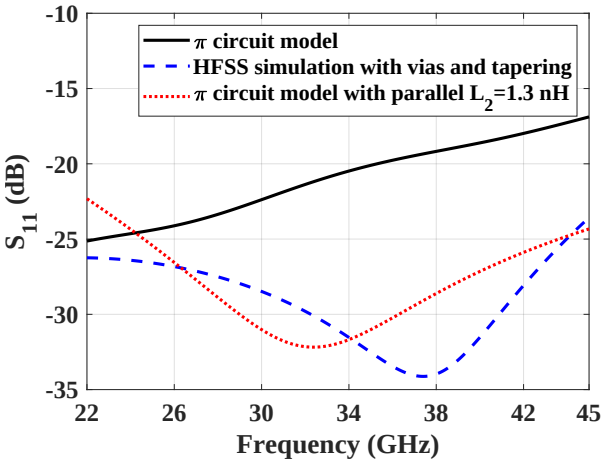

Figure 3.12: Comparison between the reflection coefficients of the π-circuit model, the π-circuit model with the added parallel inductor, and the simulated transition with the tapering and vias. (Islam Afifi et al [J1], ©2018 IEEE.)

3.3.4 Metal Ridge Gap Transition

The design of the proposed transition in the metal RGW is presented for the frequency band from 24 to 40 GHz. The structure of the unit cell which is used to realize the artificial magnetic conductor (AMC) and the associated bandgap for a single unit cell are shown in Figure 3.13 and those of the unit cell with the added ridgeline is shown in Figure 3.14, where β is the propagation constant, and a is the period of the unit cell. The CST Eigenmode solver is used with periodic boundaries to calculate the modes in Figures 3.13 and 3.14. The bandgap of the unit cell alone is from 20.05 to 45.65 GHz, while it becomes from 21.6 to 44.6 GHz when the ridgeline is included. The propagating mode (QTEM) appears because of the added ridgeline between the unit cells and propagates along the line. The appearance of extra modes, in the dispersion diagram of the unit cells with the ridgeline, is due to the truncation of the periodic boundary in the direction normal to the line [35]. While in the single unit cell case, the periodicity is on two directions, normal to the line and along the line, which assumes infinite structure and only one TM mode can propagate below the bandgap and higher order TM and TE modes can propagate after the bandgap.

The geometry of the back-to-back configuration of the proposed transition is illustrated in Figure 3.15. The design of the ridge gap waveguide with 50 Ω characteristic

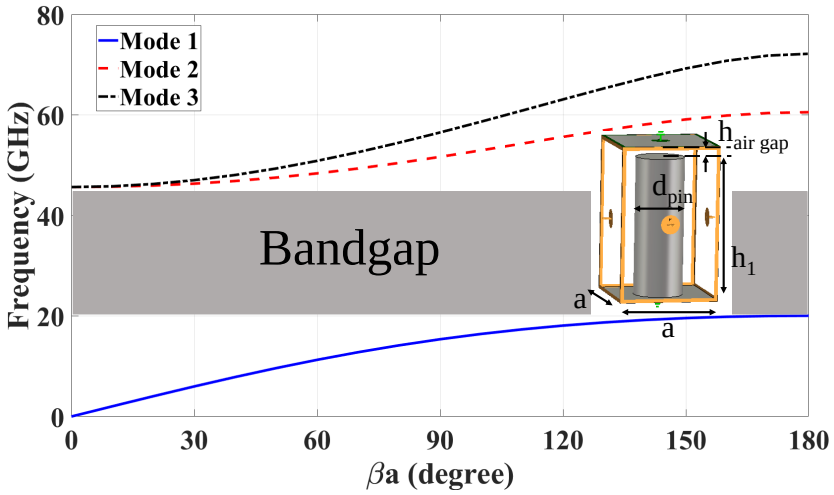

Figure 3.13: Dispersion diagram of a single unit cell for the Ka-band. (Islam Afifi et al [J1], ©2018 IEEE.)

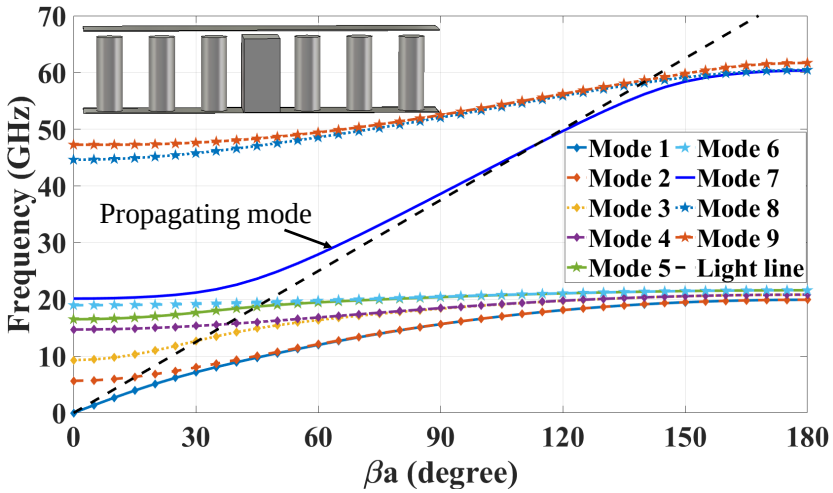

Figure 3.14: Dispersion diagram of the unit cell with the ridgeline for the Ka-band. (Islam Afifi et al [J1], ©2018 IEEE.)

impedance is done by using the stripline model [35] to calculate the initial width of the ridge-line W_{line}. Then adjustment has been done using the computer simulation technology (CST) simulator, at the center frequency, to obtain the line width for matching with a 50 Ω coaxial line. A tapered section and four pins around the ridge-line are then used to have an acceptable matching level. Finally, an optimization for the tapered section and the four vias is done to compensate for the capacitance and inductance introduced by the unit cells near the transition. The final dimensions are presented in Table 3.2. Figure 3.16 shows the simulated s-parameters for the back-to-back configuration of the proposed transition. The impedance matching bandwidth ($S_{11} < -10$ dB) is from 23.18 to 41 GHz,

which covers the whole Ka-band (from 27-40 GHz), which makes it suitable for 5G communication and imaging applications. Furthermore, the S_{21} is above -0.5 dB over the whole frequency band, and S_{11} is less than -15 dB in most of the band.

Table 3.2: The dimensions of the coaxial transition for metal ridge gap in the frequency range 24-40 GHz. (Islam Afifi et al [J1], ©2018 IEEE.)

Dimension		Value in (mm)
Coaxial outer raduis (R_1)		0.644
Matching length (L_m)		3.289
Matching width(W_1)		1.506
Ridge width(W_{line})		1.2
Unit cell period (a)		2
Pin diameter (d_{pin})		1.0
Pin height (h_{pin})		2.8
Gap height (h_{airgap})		0.289
Total line length (L_{line})		26.8
Via 1	x_1	1.547
	y_1	1.347
Via 2	x_2	2.396
	y_2	1.433

3.3.5 Printed Ridge Gap Transition

In this subsection, the proposed transition is applied in PRGW technology. The mushroom-shaped unit cell is used for the PRGW. The unit cell with its bandgap is illustrated in Figure 3.17, where the used substrate material is Roger RT6002 (ε_r=2.94 and $tan\delta$=0.0012). The bandgap is from 22.307 to 43.095 GHz for the single unit cell, and from 22.15 to 43.014 GHz for the unit cell with the ridgeline as illustrated in Figure 3.18. Another RT6002 substrate with 0.254 mm thickness is used as a middle substrate while the center is removed to introduce the air gap. The vias around the transition are inserted in this substrate. The electric field distribution on the PRGW cross-section is shown in Figure 3.19. The result shows that the use of the bandgap unit cells around the ridgeline has confined the electric field within the ridgeline section.

Figure 3.20 shows the configuration of the proposed transition. Figure 3.21 shows the electric field distribution in the middle of the air gap region and along the transition.

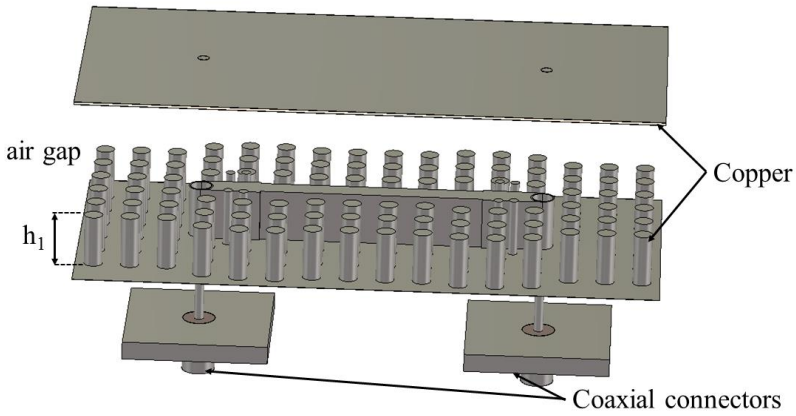

(a)

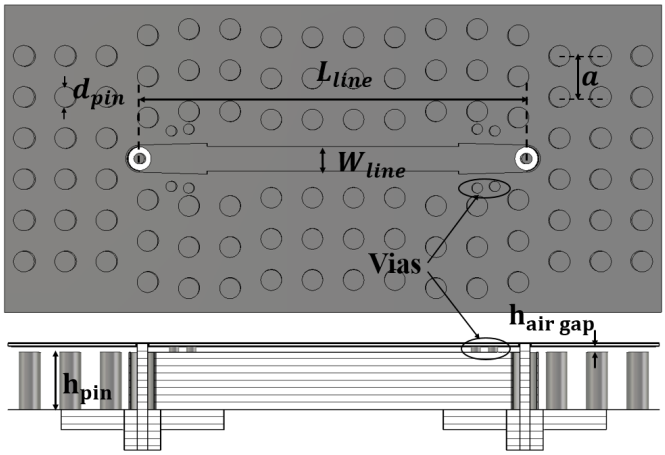

(b)

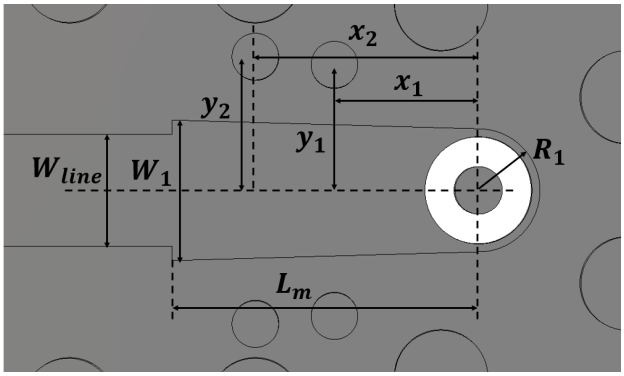

(c)

Figure 3.15: The geometry of the coaxial to metal ridge gap transition in the frequency range from 24 to 40 GHz. (a) The whole structure. (b) The top and side view (upper layer removed to show the structure). (c) The transition section. *(some inner unit cells are removed to make the geometry compact.)* (Islam Afifi et al [J1], ©2018 IEEE.)

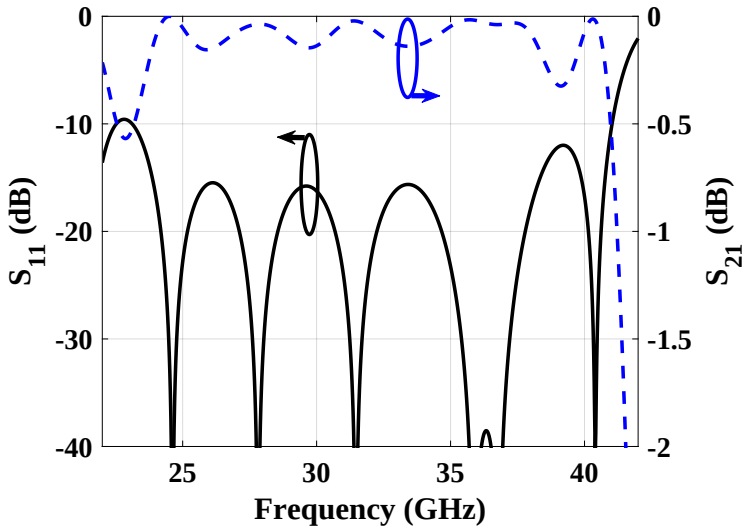

Figure 3.16: Simulated s-parameters of the coaxial to metal ridge transition in the frequency range from 24 to 40 GHz. (Islam Afifi et al [J1], ©2018 IEEE.)

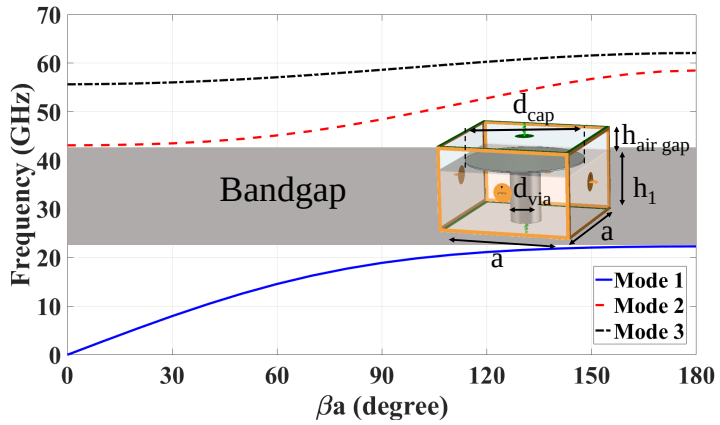

Figure 3.17: Dispersion diagram of a single unit cell for the Ka-band in the printed ridge gap technology. (Islam Afifi et al [J1], ©2018 IEEE.)

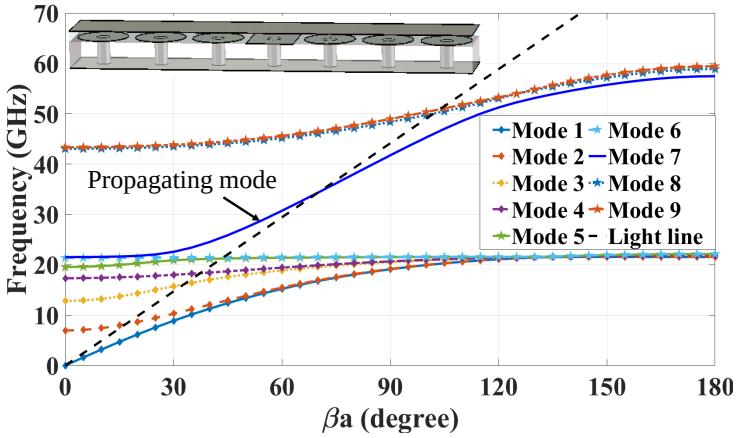

Figure 3.18: Dispersion diagram of the unit cell with the ridgeline for the Ka-band in the printed ridge gap technology. (Islam Afifi et al [J1], ©2018 IEEE.)

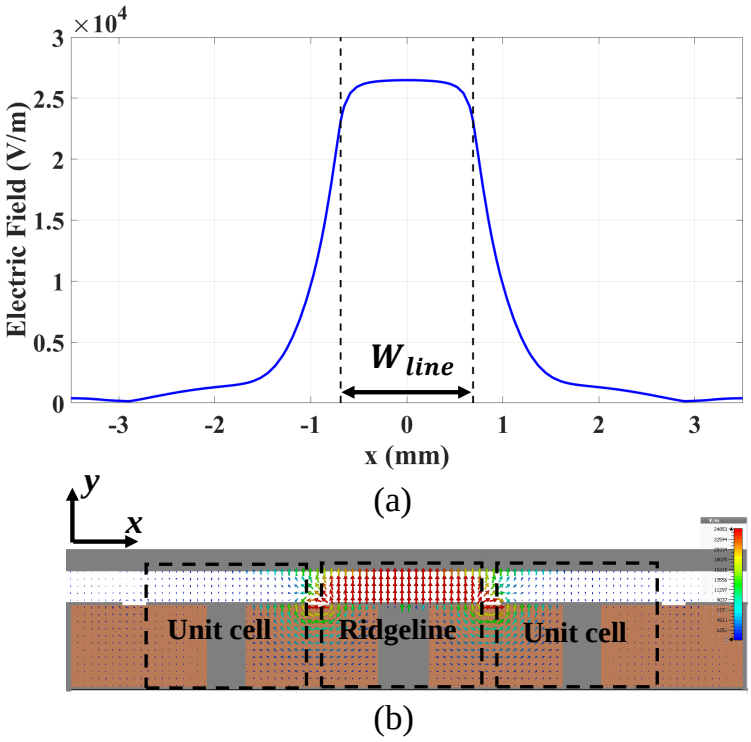

Figure 3.19: (a) The magnitude of the electric field in the middle of the air gap region. (b) Electric field distribution on the PRGW at 30 GHz. (Islam Afifi et al [J1], ©2018 IEEE.)

The final dimensions are shown in Table 3.3. The simulated s-parameters are shown in Figure 3.23 along with the measurement results, where the impedance matching bandwidth ($S_{11} < -10$ dB) is from 22.7 to 41.8 GHz, and the S_{21} is greater than -0.5 dB. Once again, the transition covers the whole Ka-band (27-40 GHz). This transition is fabricated to validate the concept of the proposed technique.

3.3.6 Measurement and Discussion

The fabricated parts of the proposed transition using conventional PCB technology together with the integrated prototype are shown in Figure 3.22. For measurement purposes, an aluminum base has been drilled with the same PCB drilling machine, and the plastic housing has been fabricated using 3D printing. A conducting copper tab has been used on top of the structure instead of soldering to connect the inner pin of the coaxial line to the upper copper plate. The (N52271A) PNA network analyzer, the Electronic

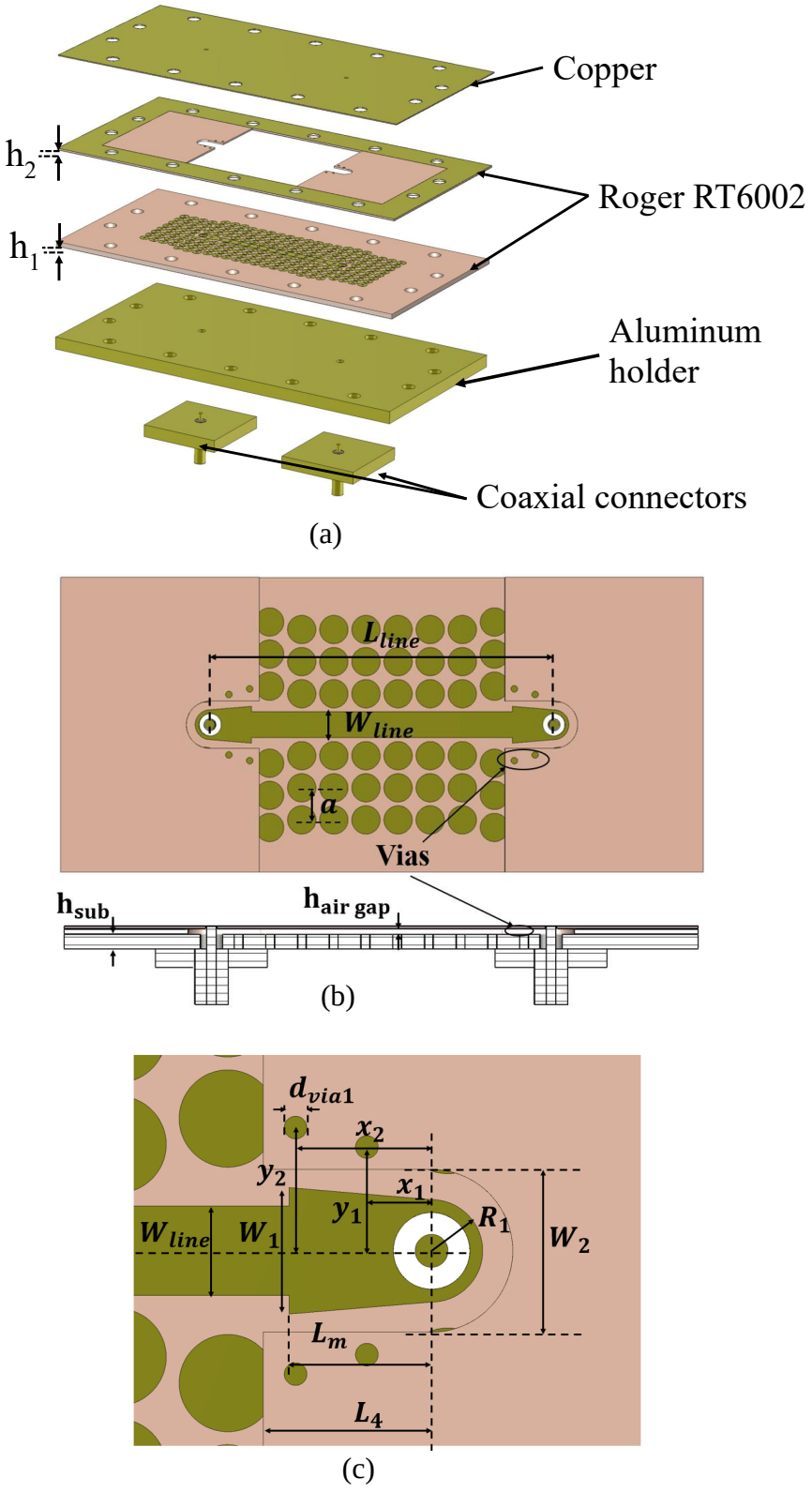

Figure 3.20: The geometry of the coaxial to printed ridge gap transition in the frequency range from 24 to 40 GHz. (a) The whole structure. (b) The top and side view (upper layer removed to show the structure). (c) The transition section. *(some inner unit cells are removed to make the geometry compact.)* (Islam Afifi et al [J1], ©2018 IEEE.)

Table 3.3: The dimensions of the coaxial transition for the printed ridge gap technology in the frequency range 24-40 GHz. (Islam Afifi et al [J1], ©2018 IEEE.)

Dimension		Value in (mm)
Coaxial outer raduis (R_1)		0.79
Matching length (L_m)		2.2
Matching width(W_1)		1.95
Ridge width(W_{line})		1.38
Unit cell period (a)		1.7
unit cell via diameter (d_{via})		0.39
unit cell cap diameter (d_{cap})		1.5
Pin height (h_{pin})		2.8
Gap height (h_{airgap})		0.289
Middle substrate inset length (L_4)		2.6
Middle substrate inset width (W_2)		2.508
Matching via diameter (d_{via1})		0.35
Total line length (L_{line})		52.2
Via 1	x_1	1
	y_1	1.6
Via 2	x_2	1.1
	y_2	1.9

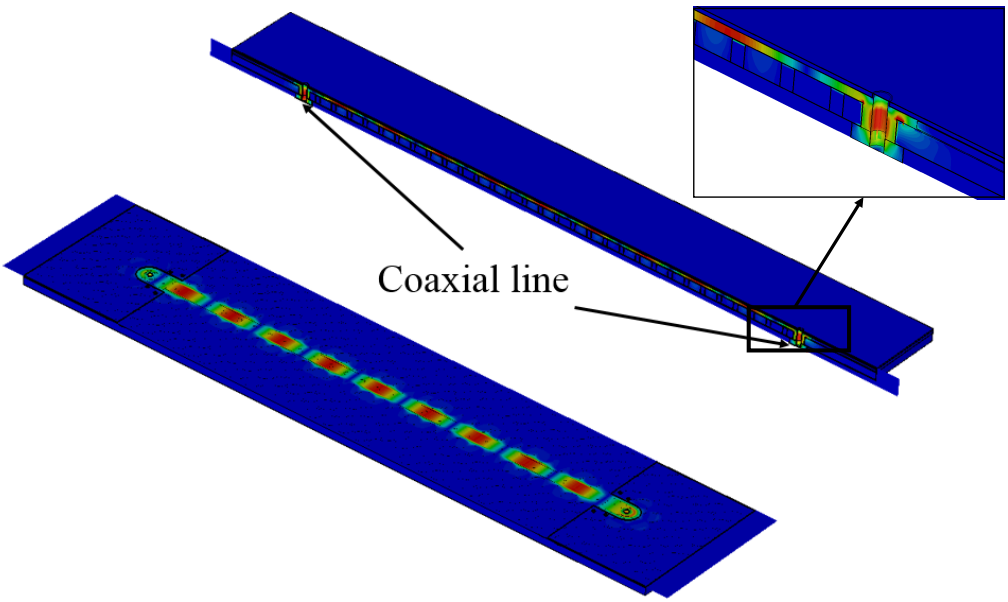

Figure 3.21: Simulated electric field distribution of the back to back coaxial to PRGW transition. (Islam Afifi et al [J1], ©2018 IEEE.)

calibration kit (Ecal), and 2.4 mm coaxial connectors are used through the measurement. There is a good agreement in the behavior between the measured and simulated results, as shown in Figure 3.23. The proposed transition achieves -10 dB matching level over the whole frequency band (24-40 GHz) with insertion loss less than 0.5 dB. The discrepancy in the amplitudes at the start of the band, between measured and simulated results, is due to the misalignment between the layers, the tolerance in the fabrication, and the contact between the connector and the ground of the ridge gap substrate. The measured performance has a fractional bandwidth of 45.8% (from 24.9-39.7 GHz) with $S_{11} < -8.3$ dB and $S_{21} > -0.5$ dB. The increase of the insertion loss at the beginning and the ending of the operating frequency band may come from dielectric and copper losses. The fields are exponentially decaying away from the ridgeline (in the bandgap region of the unit cell surrounding the ridgeline). As the operating frequency reaches the edges of the bandgap region, the exponential decaying is weak, and hence the fields suffer from the dielectric and copper losses. The reason for high losses in the measurement rather than in the simulation may come from the fact that the simulation uses the dielectric loss tangent at 10 GHz, but the measurement takes the real value at the millimeter-wave frequency range (22-42 GHz), which is different than the value at 10 GHz.

A performance comparison between the proposed design and other related work in the literature is presented in Table 3.4. The proposed transition performance is better than most of the reported transitions [35, 41–45, 50, 51, 54] in terms of the fractional bandwidth. Reported results in [47, 48] show a better fractional bandwidth performance, but they are bulky (non-planar structures) and electrically large (length is more than 2.5 λ_0) compared to the proposed transition and only suitable for CNC technology. The proposed work is planar (which makes it suitable for both CNC and PCB technologies) and compact in size (0.28 λ_0) with reasonable return loss and insertion loss. The matching concept of the proposed transition is also scalable to different frequency bands. The use of the coaxial feeding avoids dielectric and radiation losses that exist in microstrip to ridge transitions [43, 45]. The proposed transition has superior performance over other small sizes (less than λ_0) coaxial to RGW transitions reported in [35, 50]. It focuses on reducing the effect

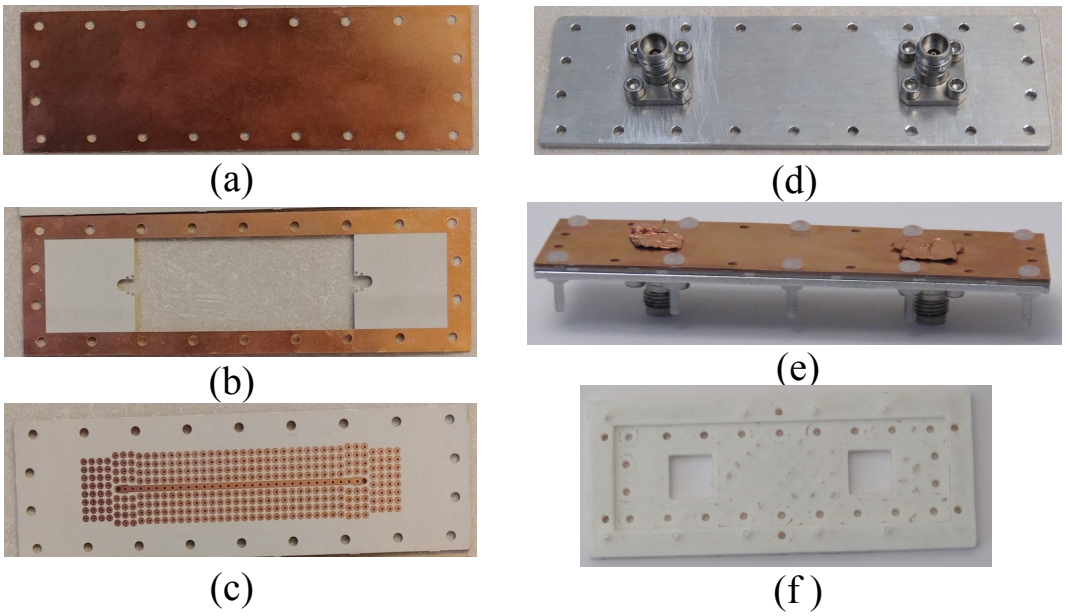

Figure 3.22: The fabricated prototype of the proposed transition in the printed ridge gap technology. (a) Top layer. (b) Middle layer. (c) Bottom layer. (d) Aluminum holder. (e) Assembled structure. (f) Plastic holder. (Islam Afifi et al [J1], ©2018 IEEE.)

of the parasitic inductance and capacitance introduced by the direct connection between the coaxial line and the RGW, and hence a wide bandwidth is achieved. The use of a rectangular waveguide to excite the ridge gap is presented in [51, 54]; it can achieve a wideband matching but again makes the design bulky.

3.4 Printed Ridge Gap Directional Coupler

3.4.1 Design Procedure

The design depends on using the normal branch line coupler [109] and adding quarter wavelength transformers at all the ports. The even and odd analysis of the coupler with the added quarter wavelength transformers has been used to build a complete circuit model of the coupler. After that, the genetic algorithm (in Matlab toolbox) is used to obtain the optimum parameters of the proposed coupler, where the objective is to have a low amplitude imbalance over a wide frequency band. Figure 3.24 shows the circuit model of the 3 dB coupler with the quarter wavelength transformers, $\theta_1 = \theta_2 = \theta_3 = \lambda/4$.

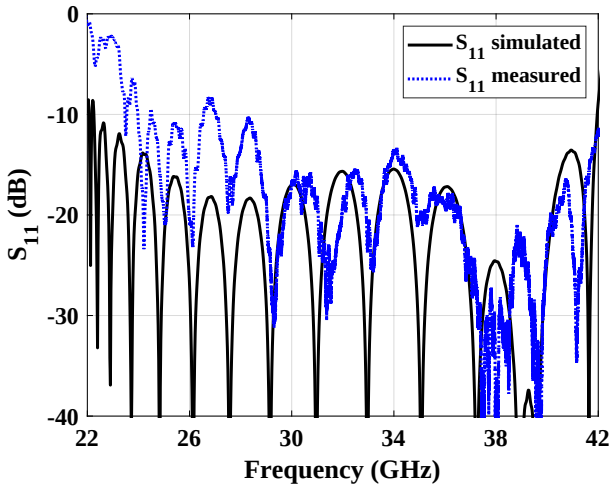

(a)

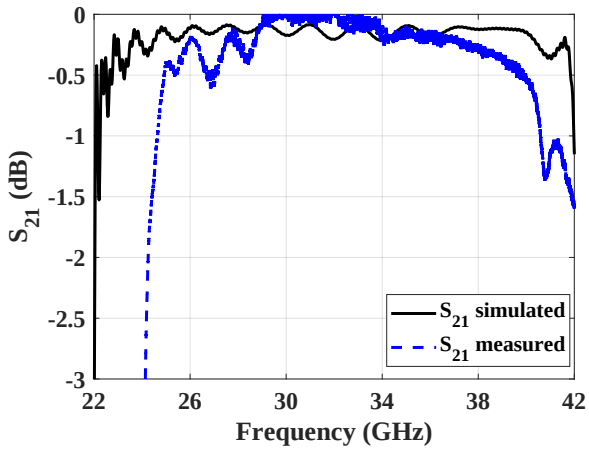

(b)

Figure 3.23: Comparison between simulated and measured s-parameters for the proposed transition. (a) S_{11} and (b) S_{21}. (Islam Afifi et al [J1], ©2018 IEEE.)

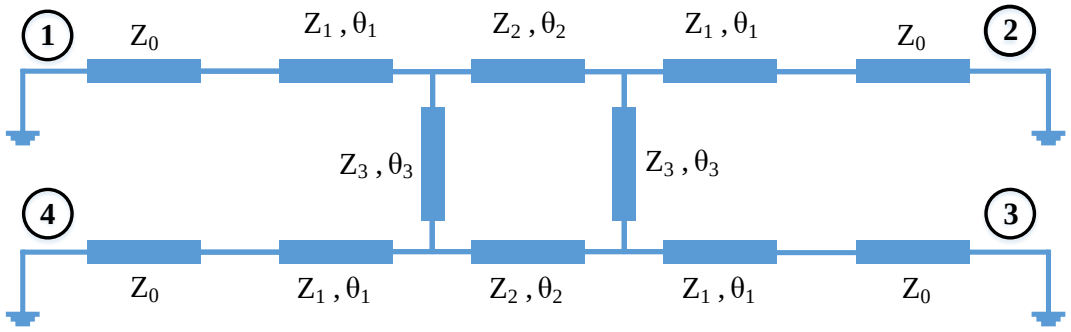

Figure 3.24: Circuit model of the 3 dB coupler.

Table 3.4: Comparison between various types of transition in the metal and printed ridge gap technologies (Islam Afifi et al [J1], ©2018 IEEE.)

	Technology	Feeding type	Fractional bandwidth (%)	Return loss (dB)	Insertion loss (dB)	Length
[51]	metal	WR62	58% (12-19 GHz)	10	-	5.5 mm (0.284 λ_0)
[42]	metal	microstrip	46.05% (11.7-18.7 GHz)	10	0.3	15.7 mm (0.796 λ_0)
[44]	metal	microstrip	20.87% (55.8-68.8 GHz)	20	0.5	-
[35]	metal	coaxial	26.67% (13-17 GHz)	8	1	10 mm (0.5 λ_0)
[47]	metal	coaxial	85.71% (10-25 GHz)	15	0.15	46.68 mm (2.723 λ_0)
[48]	metal	coaxial	96.63% (11.5-33 GHz)	15	1	58 mm (4.3 λ)
[54]	Printed	WR15	17.89% (56-67 GHz)	10	1.5	Direct connection
[41]	Printed	microstrip	38.6% (23-34 GHz)	15	0.5	-
[43]	Printed	microstrip	55.17% (21-37 GHz)	10	1	-
[45]	Printed	microstrip	37.04% (27.5-40 GHz)	10	0.8	-
[50]	Printed	coaxial	28.19% (10.97-14.57 GHz)	15	0.35	Direct connection
This work	Printed	coaxial	59.22% (22.7-41.8 GHz)	10	0.5	2.6 mm (0.28 λ_0)

The s-parameter of the coupler can be calculated from the even and odd analysis as follows [109]

$$S_{11} = \frac{S_{11e} + S_{11o}}{2} \tag{3.8}$$

$$S_{21} = \frac{S_{21e} + S_{21o}}{2} \tag{3.9}$$

$$S_{31} = \frac{S_{21e} - S_{21o}}{2} \tag{3.10}$$

$$S_{41} = \frac{S_{11e} - S_{11o}}{2} \tag{3.11}$$

Where S_{11e}, S_{21e}, S_{11o}, and S_{21e} are calculated by applying the even and odd symmetry respectively on the coupler. The even symmetry leaves open stubs of $\lambda/8$ length at the Z_3 branches of the coupler while the odd symmetry leaves short stubs. The ABCD matrices of different sections of the coupler are [109]

$$ABCD_{1e} = \begin{bmatrix} \cos(\theta_1) & jZ_1 \sin(\theta_1) \\ jY_1 \sin(\theta_1) & \cos(\theta_1) \end{bmatrix} \tag{3.12}$$

$$ABCD_{2e} = \begin{bmatrix} 1 & 0 \\ jY_3 \tan(\theta_3/2) & 1 \end{bmatrix} \tag{3.13}$$

$$ABCD_{3e} = \begin{bmatrix} \cos(\theta_2) & jZ_2 \sin(\theta_2) \\ jY_2 \sin(\theta_2) & \cos(\theta_2) \end{bmatrix} \tag{3.14}$$

$$ABCD_{2o} = \begin{bmatrix} 1 & 0 \\ -jY_3 \cot(\theta_3/2) & 1 \end{bmatrix} \tag{3.15}$$

The total ABCD matrices for the even and odd cases are

$$ABCD_{even\ total} = ABCD_{1e} ABCD_{2e} ABCD_{3e} ABCD_{2e} ABCD_{1e} \tag{3.16}$$

$$ABCD_{odd\ total} = ABCD_{1e} ABCD_{2o} ABCD_{3e} ABCD_{2o} ABCD_{1e} \tag{3.17}$$

From the genetic algorithm and the circuit model, it has been found that using values of line impedances slightly different from theoretical values gives a better amplitude imbalance. The two coupling outputs intersect at two points instead of only one point in the conventional branch line coupler. Finally, the proposed coupler has been implemented in PRGW technology and simulated using CST. Figure 3.25 shows the geometry of the coupler, and Table 3.5 shows the final optimized parameters of the coupler. Here, the genetic algorithm in CST is used in the optimization process to have a wide bandwidth and a low output amplitude imbalance (less than 1 dB) over a 20% bandwidth around 30 GHz. The simulation results are shown in Figure 3.26 and 3.27 using the finite integral time-domain(FITD) and finite integral frequency-domain (FIFD) CST solvers for the s-parameters and the output phase imbalance, respectively. The proposed coupler has an output amplitude imbalance of -3.3750 ± 0.425 dB and an output phase imbalance of $90.9° \pm 1.62°$. The return loss and the isolation are better than 15 dB over the operating frequency band (26.4 to 33.75 GHz).

Table 3.5: The dimensions of the 3-dB coupler (Islam Afifi et al [J3], ©2020 IEEE.)

Parameter	W_{line}	W_{match}	L_{match}	r_{center}	W_{ring1}	W_{ring1}
Value(mm)	1.38	1.582	3.14	1.753	1.595	3.05

3.4.2 Discussion

The proposed coupler is planar and PCB compatible with wideband and low insertion loss. It has a wideband performance, and the output amplitude and phase imbalance are good compared to other works in both the metal and PRGW [93, 118, 119] as shown in Table 3.6. The use of two sections quarter wave transformers as in [110] to have wider bandwidth is not suitable for PRGW technology where the use of a high impedance line requires a narrow line width which has a fabrication difficulty (it is difficult to connect the lines to the ground by vias that have a certain diameter larger than the line width). The prototyping of the proposed coupler is done as part of the integrated 4×4 Butler matrix in Chapter 4.

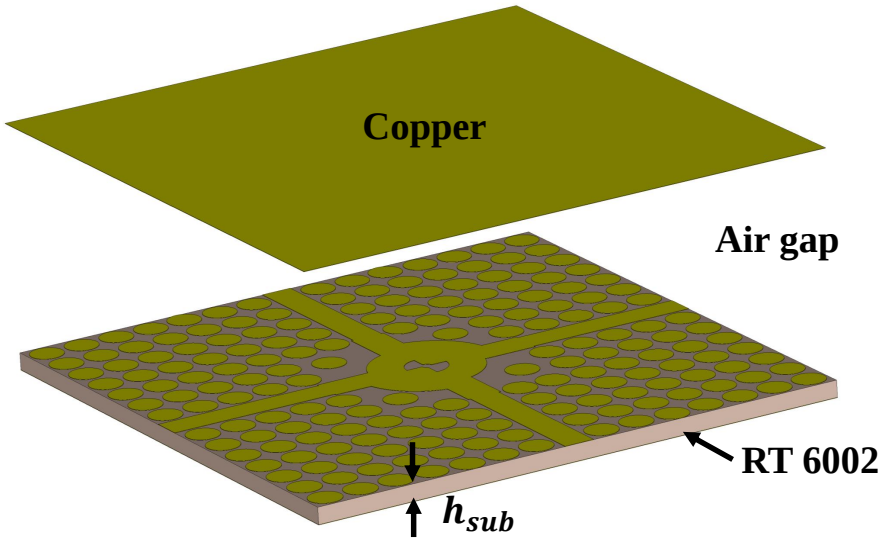

(a)

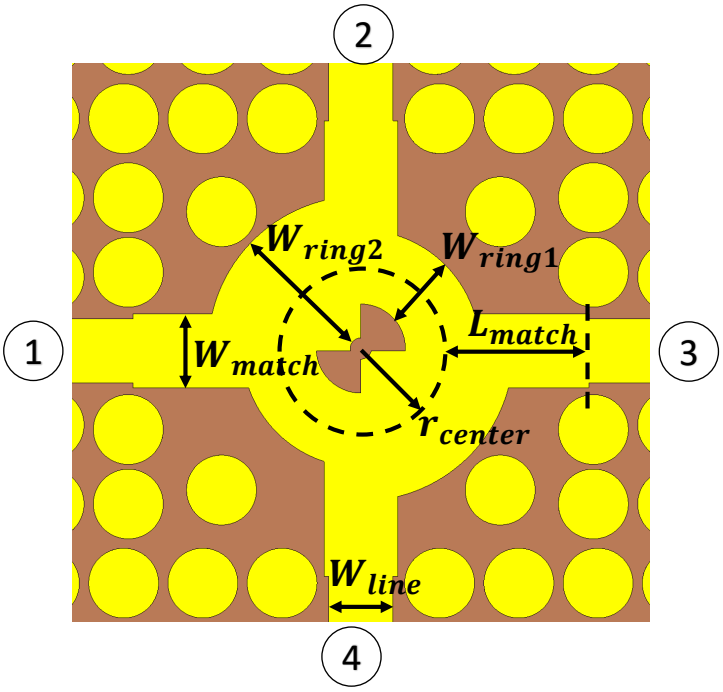

(b)

Figure 3.25: (a) 3D Geometry of the 3-dB coupler. (b) The structure of the coupler (Islam Afifi et al [J3], ©2020 IEEE.)

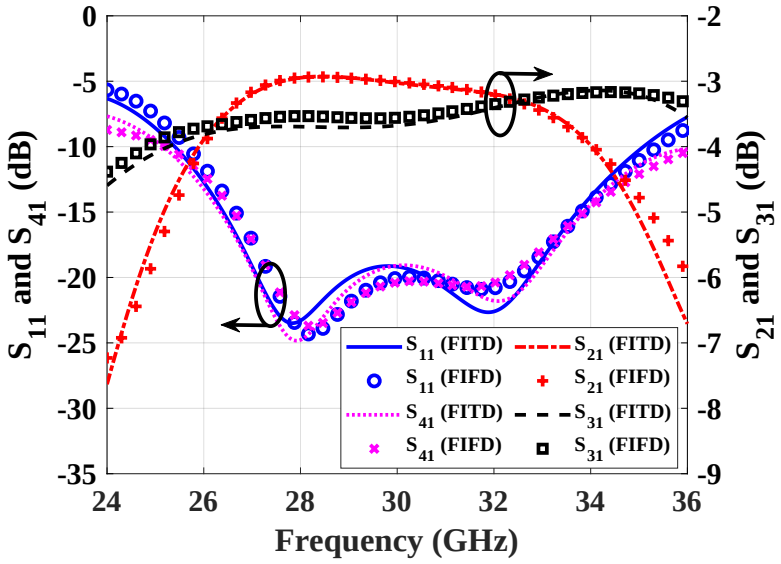

Figure 3.26: The simulated s-parameters of the 3-dB coupler (Islam Afifi et al [J3], ©2020 IEEE.)

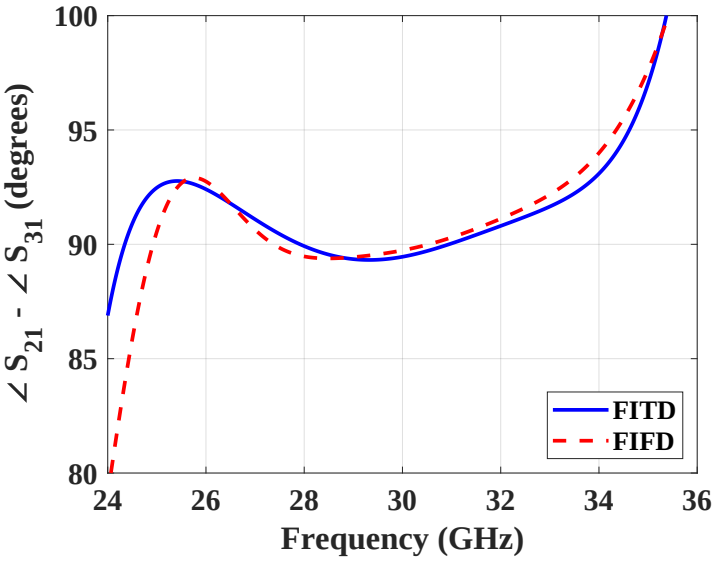

Figure 3.27: The simulated phase difference between output ports of the 3-dB coupler (Islam Afifi et al [J3], ©2020 IEEE.)

Table 3.6: Comparison between the proposed coupler and other couplers in the metal and printed ridge gap technologies

	Technology	Fractional bandwidth (%)	Return loss (dB)	Phase imbalance	Length
[118]	Metal	16.6%	14	-	$0.66\lambda_0 \times 0.7\lambda_0$
[119]	Printed	6%	10	$85° \pm 5°$	$0.41\lambda_0 \times 0.5\lambda_0$
[93]	Printed	12%	20	$90° \pm 2°$	$0.63\lambda_0 \times 0.7\lambda_0$
This work	Printed	24.5%	15	$90.9° \pm 1.62°$	$\lambda_0 \times \lambda_0$

3.5 Printed Ridge Gap Crossover

3.5.1 Design Procedure

The conventional technique for designing a planar crossover is to cascade two 3-dB directional couplers. However, the bandwidth of the resulting crossover is limited by the bandwidth of the 3-dB coupler. In this work, the proposed crossover design employs three cascaded quarter wavelength sections to have more design variables and the capability to achieve a wideband performance. The proposed crossover circuit is shown in Figure 3.28 where there is symmetry along the horizontal and vertical axes to have an identical response for each port. The genetic algorithm optimization is applied to a Matlab function that calculates the s-parameters of the crossover (using even and odd analysis), where the objective function that needs to be minimum is

$$Output = |S_{11}|^2 + |S_{21}|^2 + |S_{41}|^2 \tag{3.18}$$

which is the summation of the squares of the reflection and isolation coefficients.

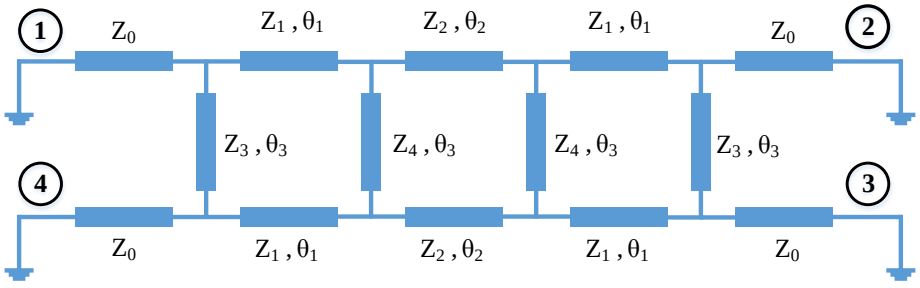

Figure 3.28: The circuit model of the proposed crossover

In order to prove that three cascaded couplers can work as a crossover, the following derivation is provided that gives conditions on the coupling coefficient of the three cascaded couplers. For the symmetry of the structure, the first and third couplers have the same coupling coefficient, as shown in Figure 3.29. In this derivation, the used couplers

are matched and isolated. Therefore, when an input signal is applied to one port of the first coupler, we can calculate the outputs a_3 and b_3 at the output of the end coupler as follows

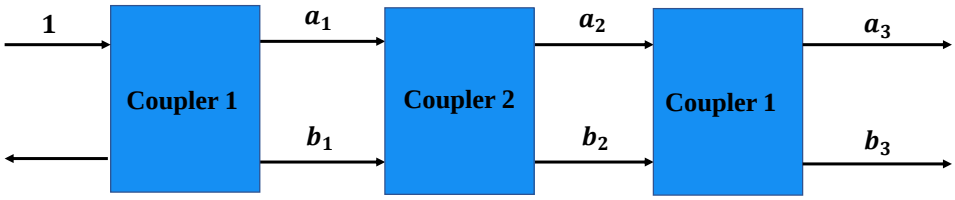

Figure 3.29: Three cascaded couplers model

$$a_1 = \sqrt{1 - C_1^2}e^{-j\pi/2} \tag{3.19}$$

$$b_1 = C_1 e^{-j\pi} \tag{3.20}$$

$$a_2 = a_1\sqrt{1 - C_2^2}e^{-j\pi/2} + b_1 C_2 e^{-j\pi} \tag{3.21}$$

$$b_2 = a_1 C_2 e^{-j\pi} + b_1\sqrt{1 - C_2^2}e^{-j\pi/2} \tag{3.22}$$

$$a_3 = a_2\sqrt{1 - C_1^2}e^{-j\pi/2} + b_2 C_1 e^{-j\pi} \tag{3.23}$$

$$b_3 = a_2 C_1 e^{-j\pi} + b_2\sqrt{1 - C_1^2}e^{-j\pi/2} \tag{3.24}$$

For a_3

$$a_3 = (a_1\sqrt{1 - C_2^2}e^{-j\pi/2} + b_1 C_2 e^{-j\pi})\sqrt{1 - C_1^2}e^{-j\pi/2} + (a_1 C_2 e^{-j\pi} + b_1\sqrt{1 - C_2^2}e^{-j\pi/2})C_1 e^{-j\pi} \tag{3.25}$$

$$a_3 = (\sqrt{1 - C_1^2}e^{-j\pi/2}\sqrt{1 - C_2^2}e^{-j\pi/2} + C_1 e^{-j\pi}C_2 e^{-j\pi})\sqrt{1 - C_1^2}e^{-j\pi/2} + (\sqrt{1 - C_1^2}e^{-j\pi/2}C_2 e^{-j\pi} + C_1 e^{-j\pi}\sqrt{1 - C_2^2}e^{-j\pi/2})C_1 e^{-j\pi} \tag{3.26}$$

$$a_3 = \left(-(1-C_1^2)\sqrt{1-C_2^2} + C_1C_2\sqrt{1-C_1^2} + \sqrt{1-C_1^2}C_1C_2 + C_1^2\sqrt{1-C_2^2} \right) e^{-j\pi/2} \tag{3.27}$$

$$a_3 = \left((2C_1^2-1)\sqrt{1-C_2^2} + 2C_1C_2\sqrt{1-C_1^2} \right) e^{-j\pi/2} \tag{3.28}$$

for crossover condition $a_3 = 0$

$$(1-2C_1^2)^2(1-C_2^2) = 4C_1^2C_2^2(1-C_1^2) \tag{3.29}$$

$$C_2 = \sqrt{\frac{(1-2C_1^2)^2}{(1-2C_1^2)^2 + 4C_1^2(1-C_1^2)}} \tag{3.30}$$

From the last equation and the circuit model, Figure 3.30 is produced where the relation between the coupling coefficients (C_1 and C_2) to have a crossover device is presented along with the associated 15 dB return loss and isolation bandwidth. It is clear that the bandwidth decreases with increasing the coupling coefficient (C_1) and reaches its minimum value when $C_1 = 0.707$, which is corresponding to have only two 3-dB couplers. Also, coupling values of C_1 between 0.5 and 0.645 give an almost constant bandwidth of about 22.9 %.

Figures 3.31 shows the s-parameters of the crossover, which are calculated using the three cascaded coupler model. Figure 3.32 shows the s-parameter of the optimized circuit where the genetic algorithm is used to have a wide bandwidth ($\geq$ 30%). Table 3.7 shows the optimized parameters along with that obtained from the three-coupler model. It is observed that a small change in the circuit parameters has greatly improved the bandwidth from 23% in the three-coupler model to 33.3% in the optimized circuit.

Table 3.7: The optimum parameters of the crossover

Line impedance	Z_1	Z_2	Z_3	Z_4
Value calculated (Ω)	41.4246	46.3956	73.9726	46.3956
Value optimized (Ω)	45	47	74	57

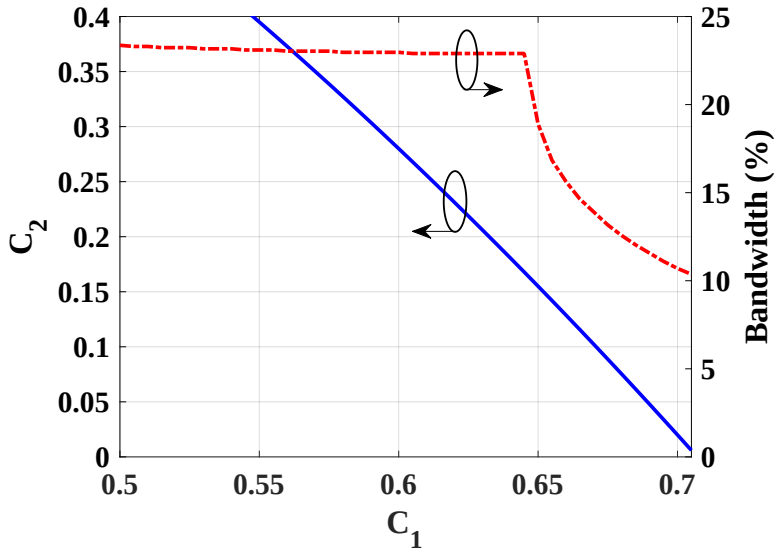

Figure 3.30: Coupling values that satisfy the crossover condition and the associated bandwidth.

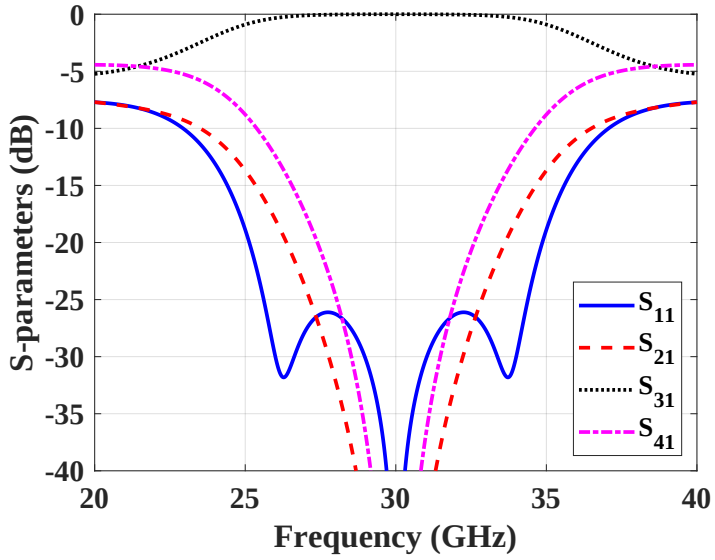

Figure 3.31: S-parameters of the crossover using the three couplers circuit model with $C_1 = 0.56$ and $C_2 = 0.3728$

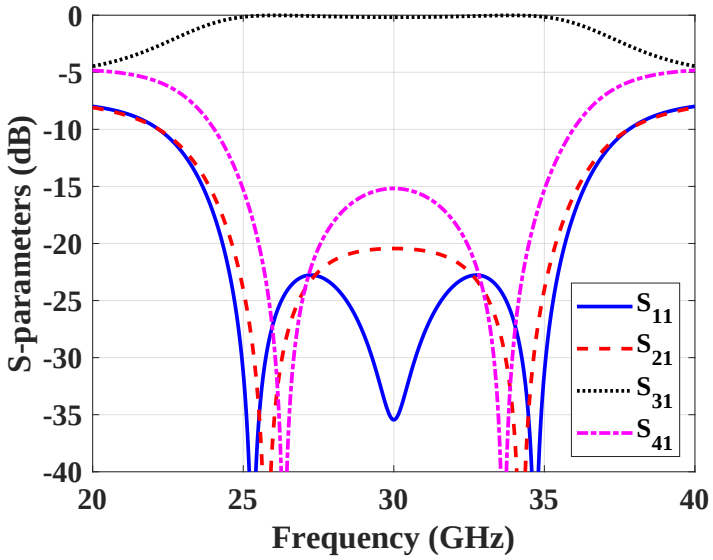

Figure 3.32: S-parameters of the crossover using optimization.

Now, as the operation concept of the crossover has been illustrated, the next step is to implement the crossover in the PRGW technology. The CST is used for the simulation and bandwidth from 26.8 to 33.9 GHz (23.4 %) is achieved with return loss and isolation better than 14 dB. Moreover, the insertion loss is better than 0.5 dB over the operating bandwidth. Figure 3.33 shows the geometry of the PRGW crossover, and the dimensions are in Table 3.8. Finally, the simulated s-parameters for the PRGW crossover is presented in Figure 3.34.

Table 3.8: The dimensions of the PRGW crossover (Islam Afifi et al [J3], ©2020 IEEE.)

Parameter	W_{line}	W_1	W_2	W_3	W_4	L_1	L_2	L_3
Value(mm)	1.38	1.56	1.49	0.52	1.23	3.65	3.65	3.65

3.5.2 Discussion

Theoretical comparison between the conventional crossover (which consist of two cascaded 3-dB couplers) and the proposed one shows that the proposed one has a wider bandwidth and a lower phase error, as shown in Figures 3.35 and 3.36. Moreover, the proposed crossover is a planar structure with a compact size and a wide bandwidth compared to the device in [124], which is implemented in the same technology and the same

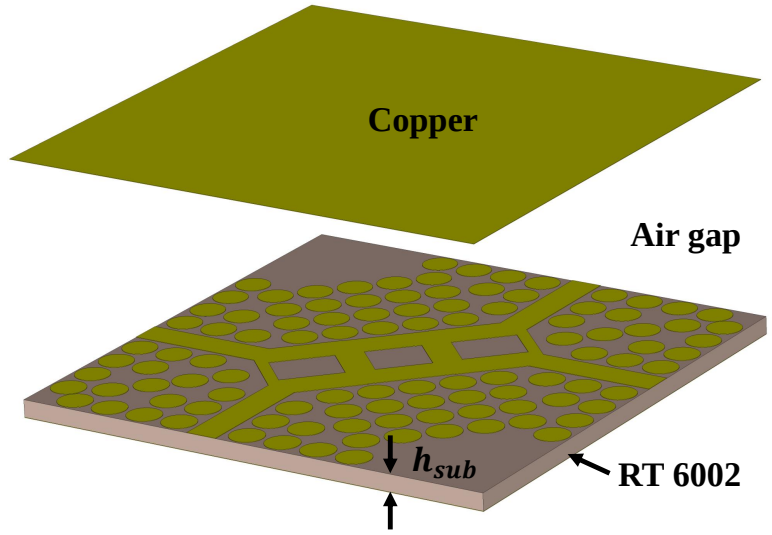

(a)

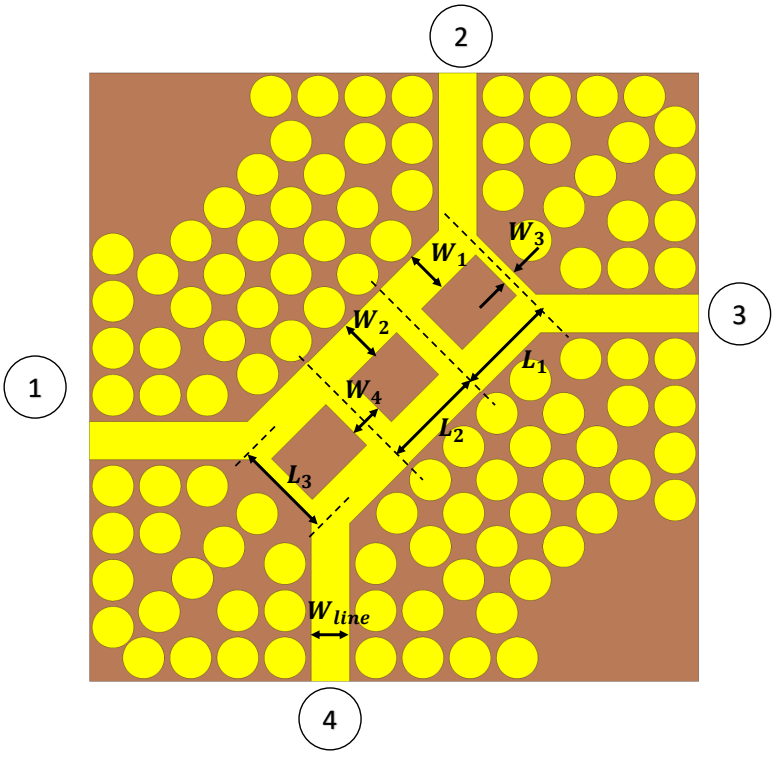

(b)

Figure 3.33: (a) 3D Geometry of the proposed PRGW crossover. (b) The ridge layer of the proposed PRGW crossover (Islam Afifi et al [J3], ©2020 IEEE.)

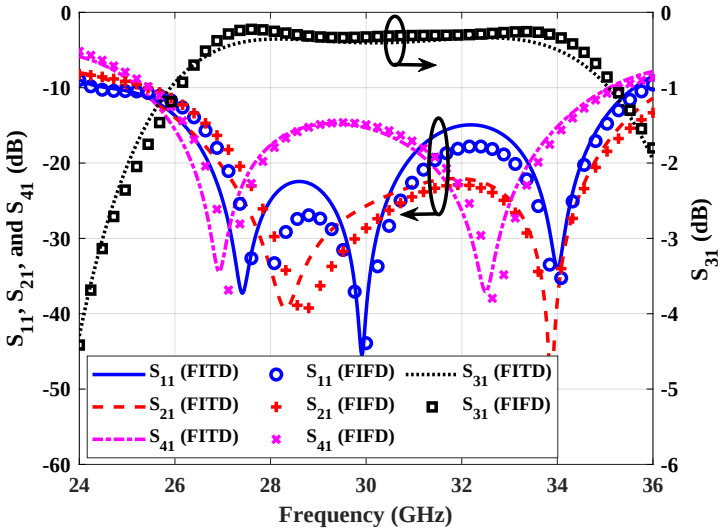

Figure 3.34: The simulated s-parameters of the printed ridge gap crossover (Islam Afifi et al [J3], ©2020 IEEE.)

center frequency. Also, it is compact in size compared to [49] (less than half of it), while the achieved bandwidth is comparable to it (the proposed work has 23.4% bandwidth while the work in [49] has 26% bandwidth). The implementation of the device on the PRGW technology gives the device the advantage of low losses and the support of Q-TEM mode. The prototyping of the proposed crossover is done as part of the integrated 4×4 Butler matrix in Chapter 4.

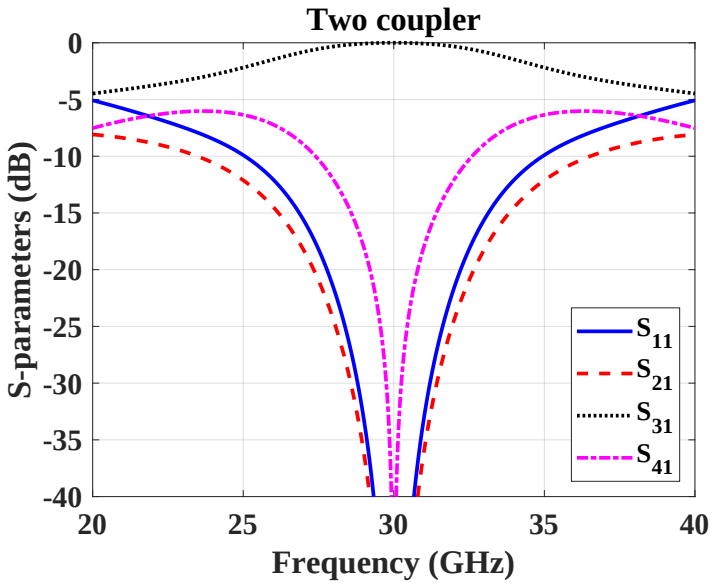

Figure 3.35: The s-parameters of two cascaded 3-dB coupler (9.33% bandwidth with return loss and isolation better than 15 dB.

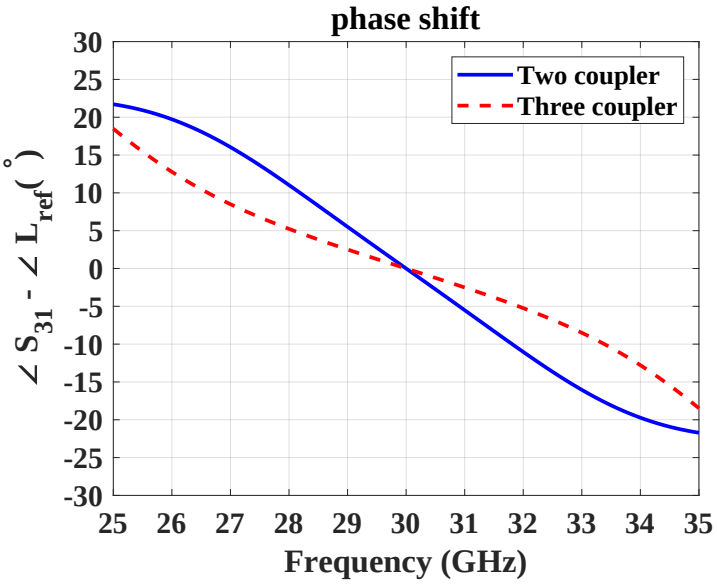

Figure 3.36: The phase difference between the transmission port and the reference line for the two-3dB coupler case and the optimized crossover case.

Table 3.9: Comparison between the proposed crossover and other crossovers in the printed ridge gap technology

	Technology	Fractional bandwidth (%)	Return loss (dB)	Frequency (GHz)	Length
[49]	Printed	26%	10	13.54	$5.18\lambda_0 \times 2.14\lambda_0$
[124]	Printed	13.33%	20	30.5	$1.5\lambda_0 \times 1.5\lambda_0$
This work	Printed	23.4%	15	30	$1.1\lambda_0 \times 0.5\lambda_0$

3.6 Printed Ridge Gap 45° Phase Shifter

3.6.1 Design Procedure

The design of a phase shifter is based on having a coupled line coupler with ports 2 and 3 connected to each other [143]. This gives a device with only two ports and a phase shift between the input and the output ports. The analysis regarding a 90° phase shifter is given in [143] for a Schiffman phase shifter. In this work, a 45° phase shifter is needed for the standard 4×4 Butler matrix, so the analysis of coupled line coupler is used to

determine the value of the coupling length that produces a wideband 45° phase shift. The structure is given in Figure 3.37. The simulated s-parameters and phase shift are in Figure 3.38. Table 3.10 presents the final optimized dimensions of the phase shifter, where the optimization is set for having a wide bandwidth ($\geq$ 20%) and a low phase imbalance around 45° ($\leq$ 3°).

Table 3.10: The dimensions of the phase shifter (Islam Afifi et al [J3], ©2020 IEEE.)

Parameter	W_{line}	W_{line2}	W_1	W_2	W_3	W_4	L_1	L_2	S
Value(mm)	1.38	1.35	1.49	1.28	0.88	1.4	5.99	10.64	0.15

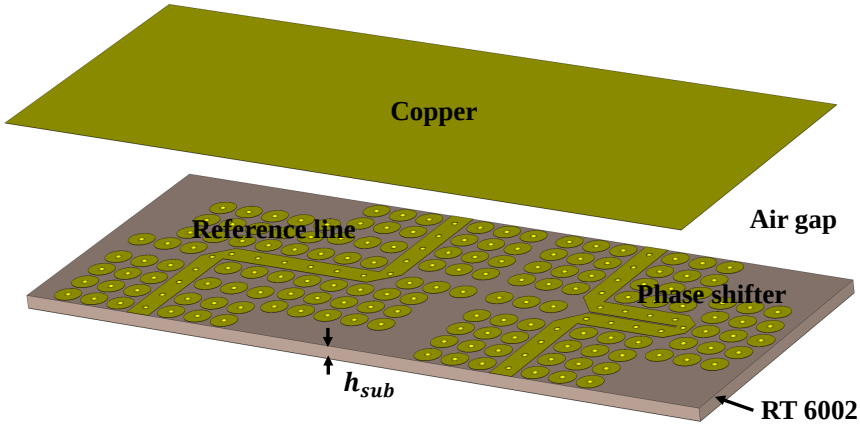

(a)

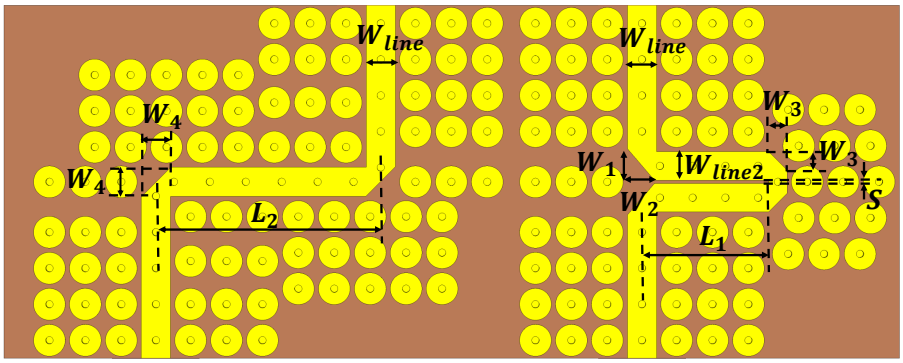

(b)

Figure 3.37: (a) 3D Geometry of the proposed phase shifter and the reference line. (b) The ridge layer of the proposed phase shifter and the reference line (Islam Afifi et al [J3], ©2020 IEEE.)

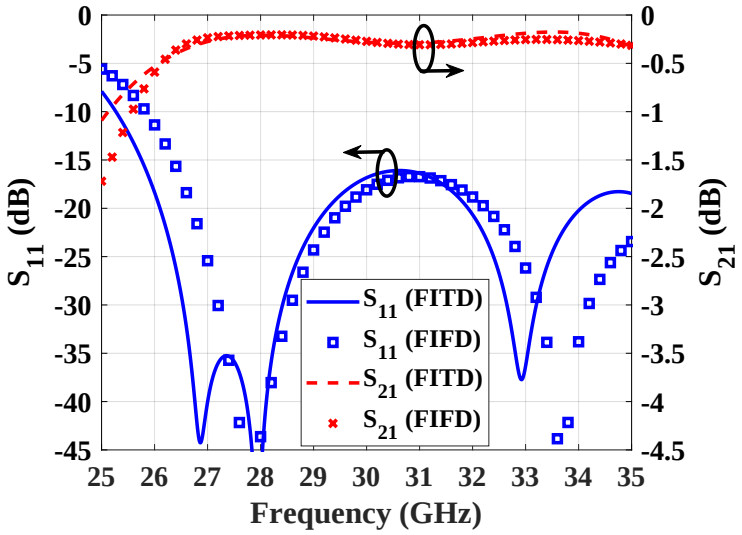

(a)

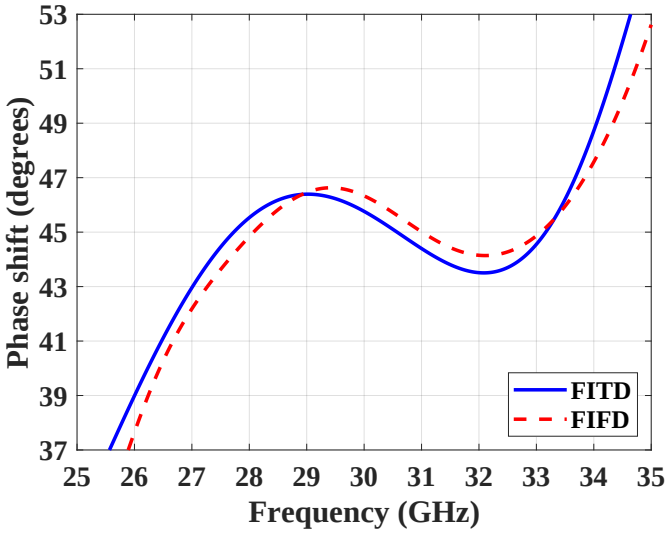

(b)

Figure 3.38: (a) The simulated s-parameters of the phase shifter. (b) The simulated phase shift between the coupled line and the reference line. (Islam Afifi et al [J3], ©2020 IEEE.)

In the proposed work, a wideband phase shifter with low variation is essential for a wideband and high performance Butler matrix. The designed phase shifter has a wideband from 27 to 33.6 GHz with an output phase shift of $45^\circ \pm 2^\circ$, return loss better than 15 dB, and $S_{21} > -0.4$ dB.

3.6.2 Discussion

The proposed phase shifter is based on the Schiffman phase idea. It is implemented in the PRGW technology, which is a new and promising technology for MMW band applications. It has a wideband of 21.7% around 30 GHz and a phase shift of 45°, which makes it suitable for the standard 4×4 Butler matrix. The prototyping of the proposed phase shifter is done as part of the integrated 4×4 Butler matrix in Chapter 4.

3.7 Rat-Race Coupler Design

3.7.1 Design Procedure

The proposed design employing an open stub at the middle of the $3\lambda/4$ branch line and quarter wavelength lines at all the ports of the rat-race. The objective of the added stub is to separate the output ports amplitudes around the -3 dB level by certain values depending on the required amplitude imbalance. This results in having two intersection points for the output ports instead of one, for the conventional coupler, and hence the amplitude imbalance bandwidth increases. The objective of the added quarter wavelength lines is to improve the matching and isolation bandwidths.

First, the general equations of the proposed coupler (shown in Figure 3.39) are used to make a circuit model as in [J2]. The s-parameters of the rat-race is calculated from the

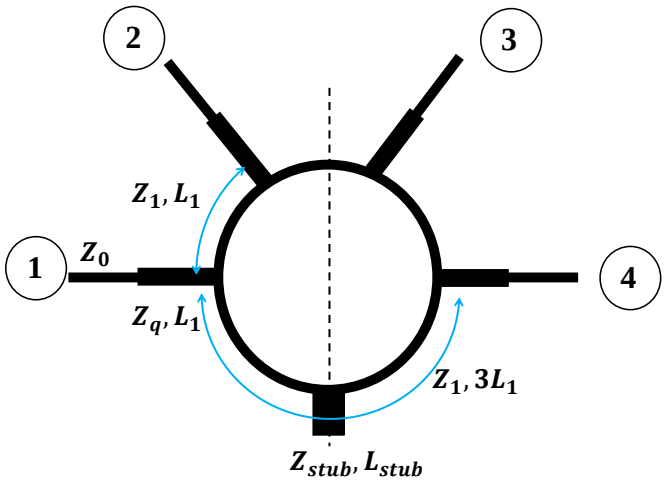

(a)

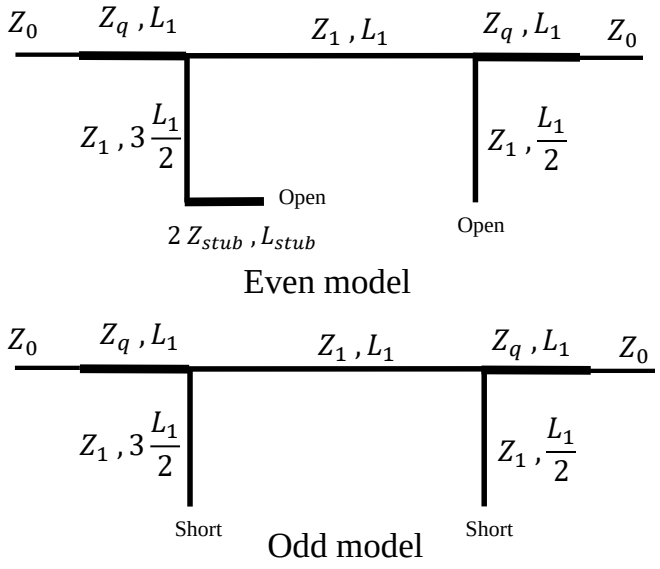

(b)

Figure 3.39: (a) Geometry of the proposed Rat race coupler. (b) Equivalent even and odd circuits of the proposed rat race. (Islam Afifi et al [J2], ©2020 IEEE.)

even and odd analysis as follows [109].

$$S_{11} = \frac{S_{11e} + S_{11o}}{2} \tag{3.31}$$

$$S_{21} = \frac{S_{21e} + S_{21o}}{2} \tag{3.32}$$

$$S_{31} = \frac{S_{21e} - S_{21o}}{2} \tag{3.33}$$

$$S_{41} = \frac{S_{11e} - S_{11o}}{2} \tag{3.34}$$

Where S_{11e} ,S_{21e}, S_{11o}, and S_{21e} are calculated by applying the even and odd symmetry respectively on the rat race. The even symmetry leaves open stubs while the odd symmetry leaves short stubs. The ABCD matrices of different sections of the rat-race for even symmetry are [109]

$$ABCD_{1e} = \begin{bmatrix} \cos(\beta L_1) & jZ_q \sin(\beta L_1) \\ jY_q \sin(\beta L_1) & \cos(\beta L_1) \end{bmatrix} \tag{3.35}$$

$$ABCD_{2e} = \begin{bmatrix} 1 & 0 \\ \frac{Z1+2Z_{stub}\cot(\beta L_{stub})\tan(3\beta L_1/2))}{Z_1(-2jZ_{stub}\cot(\beta L_{stub})+jZ_1\tan(3\beta L_1/2))} & 1 \end{bmatrix} \tag{3.36}$$

$$ABCD_{3e} = \begin{bmatrix} \cos(\beta L_1) & jZ_1 \sin(\beta L_1) \\ jY_1 \sin(\beta L_1) & \cos(\beta L_1) \end{bmatrix} \tag{3.37}$$

$$ABCD_{4e} = \begin{bmatrix} 1 & 0 \\ jY_1 \tan(\beta L_1/2) & 1 \end{bmatrix} \tag{3.38}$$

The total ABCD matrix for the even mode is given by

$$ABCD_{even\ total} = ABCD_{1e}\ ABCD_{2e}\ ABCD_{3e}\ ABCD_{4e}\ ABCD_{1e} \tag{3.39}$$

For the odd mode analysis, the second and forth ABCD matrix are

$$ABCD_{2o} = \begin{bmatrix} 1 & 0 \\ -jY_1 \cot(3\beta L_1/2) & 1 \end{bmatrix} \tag{3.40}$$

$$ABCD_{4o} = \begin{bmatrix} 1 & 0 \\ -jY_1 \cot(\beta L_1/2) & 1 \end{bmatrix} \tag{3.41}$$

The total ABCD matrices for the odd case is

$$ABCD_{odd\,total} = ABCD_{1e}\ ABCD_{2o}\ ABCD_{3e}\ ABCD_{4o}\ ABCD_{1e} \tag{3.42}$$

In order to illustrate the effect of the added stub on the amplitude imbalance, we take $Z_{stub} = \frac{1}{\sqrt{2}} Z_0$,and $Z_q = Z_0$. Therefore the $ABCD_{2e}$ can be written as

$$ABCD_{2e} = \begin{bmatrix} 1 & 0 \\ jY_1 \tan\left(\beta\left(\frac{3L_1}{2} + L_{stub}\right)\right) & 1 \end{bmatrix} \tag{3.43}$$

For small value of L_{stub} and at the center frequency,

$$\tan\left(\beta\left(\frac{3L_1}{2} + L_{stub}\right)\right) = \tan\left(\frac{3\pi}{4} + \Delta\theta\right) \tag{3.44}$$

where $\Delta\theta = \beta L_{stub}$, and using the trigonometric identity that

$$\tan(a+b) = \frac{\tan a + \tan b}{1 - \tan a \tan b} \tag{3.45}$$

then

$$\tan\left(\frac{3\pi}{4} + \Delta\theta\right) \approx \frac{\Delta\theta - 1}{\Delta\theta + 1} \tag{3.46}$$

After that we substitute in the ABCD matrix and get the s-parameters as follows

$$S_{11} = \frac{\frac{1}{2}\Delta\theta(1+j2\sqrt{2})}{-2\Delta\theta+j\sqrt{2}(\Delta\theta+2)} \tag{3.47}$$

$$S_{21} = \frac{2+\frac{3}{2}\Delta\theta+j\frac{1}{\sqrt{2}}\Delta\theta}{-2\Delta\theta+j\sqrt{2}(\Delta\theta+2)} \tag{3.48}$$

$$S_{31} = \frac{\frac{1}{2}\Delta\theta(1-j\sqrt{2})}{-2\Delta\theta+j\sqrt{2}(\Delta\theta+2)} \tag{3.49}$$

$$S_{41} = \frac{-2-\frac{1}{2}\Delta\theta}{-2\Delta\theta+j\sqrt{2}(\Delta\theta+2)} \tag{3.50}$$

By taking the absolute values, the following equations are obtained.

$$|S_{11}|^2 = \Delta\theta^2\frac{2.25}{6\Delta\theta^2+8\Delta\theta+8} \tag{3.51}$$

$$|S_{21}|^2-1/2 = \Delta\theta\frac{2-0.25\Delta\theta}{6\Delta\theta^2+8\Delta\theta+8} \tag{3.52}$$

$$|S_{31}|^2 = \Delta\theta^2\frac{0.75}{6\Delta\theta^2+8\Delta\theta+8} \tag{3.53}$$

$$|S_{41}|^2-1/2 = -\Delta\theta\frac{2.75\Delta\theta+2}{6\Delta\theta^2+8\Delta\theta+8} \tag{3.54}$$

These equations illustrate that the amplitude of S_{21} is greater than $\frac{1}{\sqrt{2}}$ and increases with proportion to the added stub length. Also, the amplitude of S_{41} becomes less than $\frac{1}{\sqrt{2}}$ and decreases with proportion to the stub length. From the known behavior of the S_{21} and S_{41} (makes $\frown$ shape and $\smile$ shape around the center frequency respectively), they will intersect again at two different points around the center frequency and hence increase the amplitude imbalance bandwidth. Moreover, it is observed that the change of the matching and isolation is very small and proportional to $\Delta\theta^2$.

In order to prove the concept that adding a stub and quarter wave transformers improves the bandwidth for the general case, a parametric study on the effect of the stub is carried out using the ABCD matrix circuit model with $Z_q = Z_0/\sqrt[4]{2}$ and $Z_1 = Z_0$. Figure 3.40 (a) shows the effect of the stub length on the amplitude imbalance of the output ports, while its effect on the matching and isolation levels is depicted in Figure 3.40 (b). Unlike

the conventional rat race, which has one intersection point between the output ports, the addition of the stub provides a wide amplitude imbalance bandwidth. This is achieved by having the outputs intersect at two points instead of one. On the other hand, as the stub length increases, the separation between the intersection points increases, resulting in a deterioration of the output amplitude imbalance, the matching, and the isolation. Therefore, optimization is needed to have a wide bandwidth with an acceptable amplitude imbalance, matching, and isolation. Figure 3.41 shows the geometry of the designed rat-race coupler where $W_q = 1.7$ mm, $L_q = 2.5$ mm, $R_1 = 1.85$ mm, $R_2 = 3.35$ mm, $W_{stub} = 0.8$ mm, and $L_{stub} = 2.4$ mm. These values are optimized using the genetic algorithm in the CST to have a wide bandwidth ($\geq 25\%$) and a low amplitude imbalance (≤ 1 dB).

The designed coupler and the fabricated prototype are shown in Figure 3.42, where the ridgeline layer, the upper copper layer, and the spacer are manufactured using the conventional printed circuit board technology (PCB). The metal base has been drilled also with the PCB machining and used to hold the 2.4 coaxial connectors. After that, the whole structure is assembled with plastic screws. The measured results, along with the simulated ones, are shown in Figure 3.43. The behavior of the measured results matches very well with simulation results as there are two intersection points in the output ports, which improve the output amplitude imbalance bandwidth. The proposed coupler has 27.96% bandwidth around 30 GHz, the operating bandwidth is determined by having the return loss and the isolation better than 15 dB, and a coupling imbalance less than 1 dB (peak-to-peak).

3.7.2 Discussion

In Table 3.11, a brief comparison between the proposed coupler and other couplers is presented where the focused is on the SIW and RGW structures as they are the promising technologies for the millimeter-wave band.

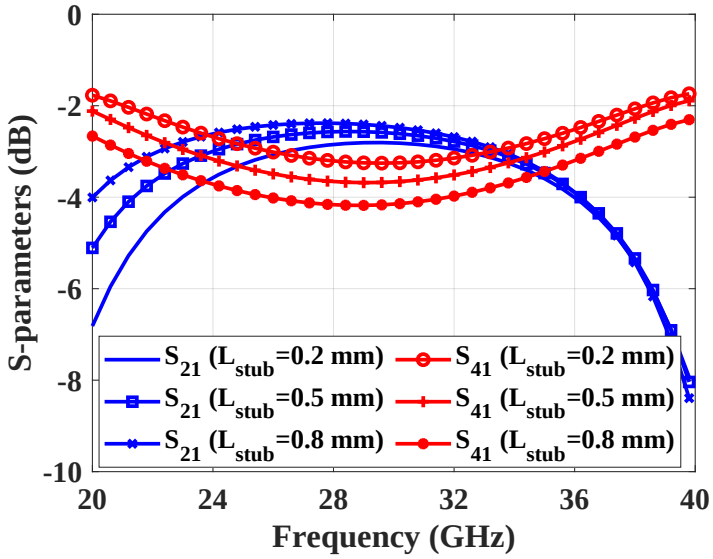

(a)

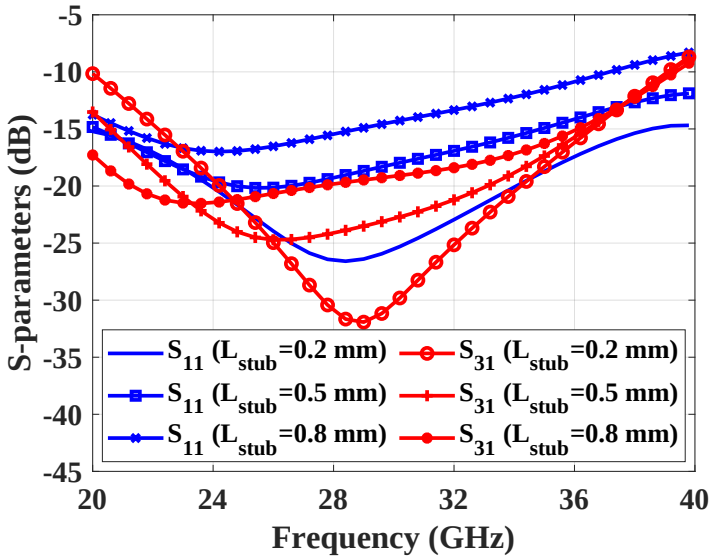

(b)

Figure 3.40: S-parameters of the proposed rat race with different values of L_{stub} while the other parameters are fixed ($Z_q = Z_0/\sqrt[4]{2}$, $Z_1 = Z_0$, and $Z_{stub} = 30\Omega$). (a) S_{21} and S_{41}. (b) S_{11} and S_{31}. (Islam Afifi et al [J2], ©2020 IEEE.)

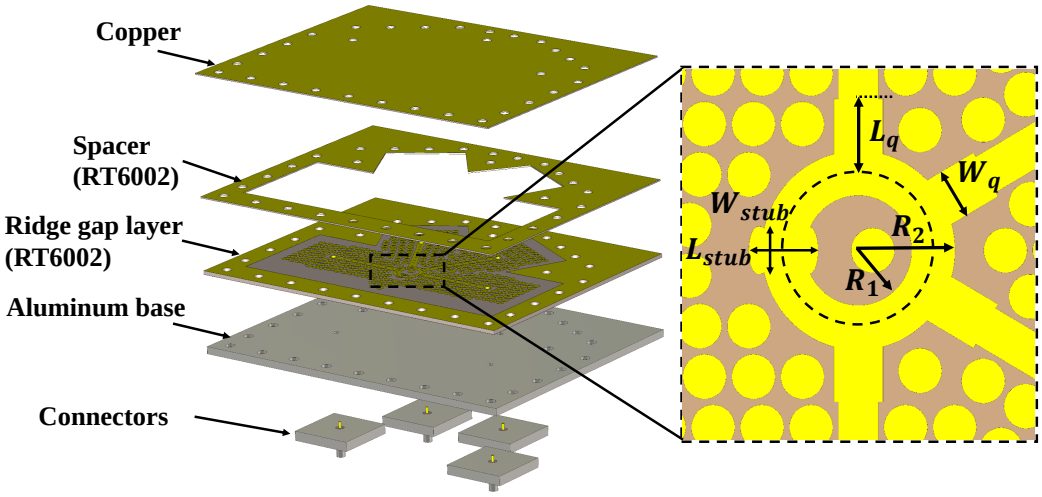

Figure 3.41: Geometry of the printed ridge gap rat-race coupler with a quarter wave transformer and a stub in the $3\lambda/4$ branch. (Islam Afifi et al [J2], ©2020 IEEE.)

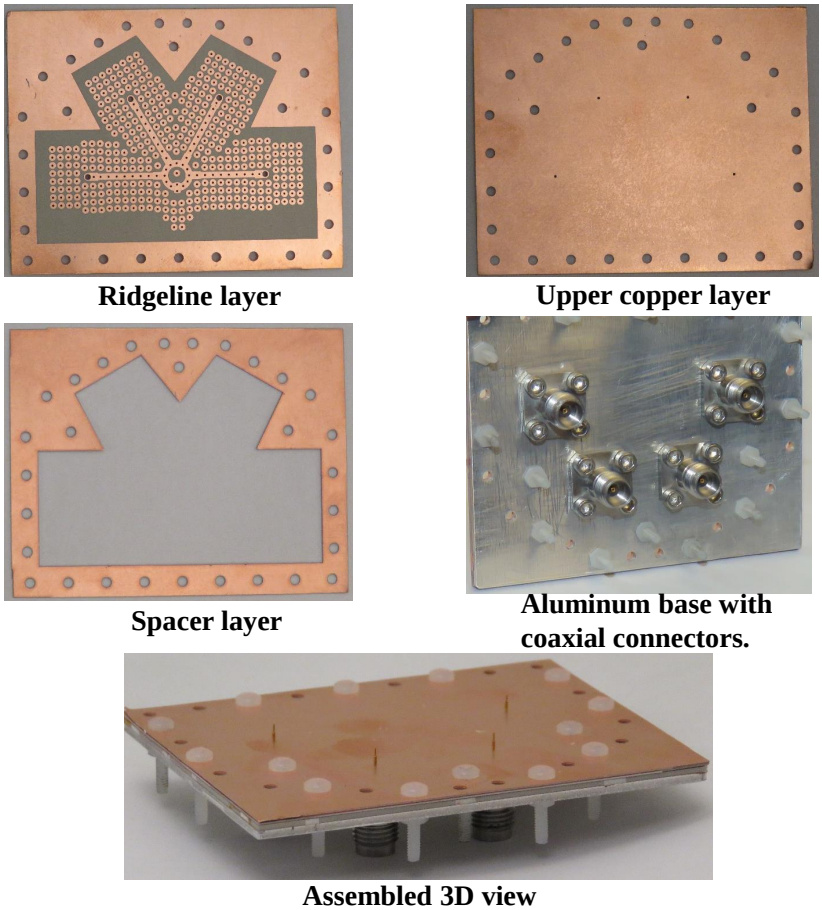

Figure 3.42: Fabricated parts of the printed ridge gap rat-race coupler. (Islam Afifi et al [J2], ©2020 IEEE.)

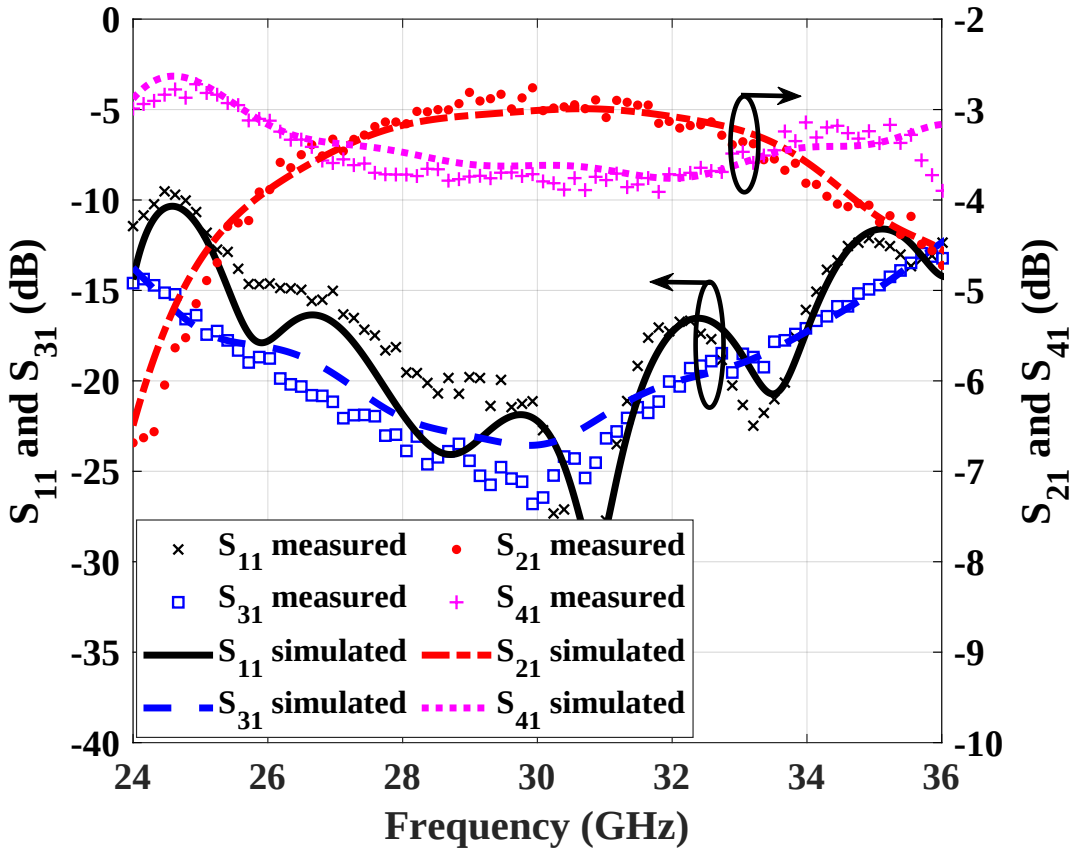

Figure 3.43: Compare simulated and measured results (Islam Afifi et al [J2], ©2020 IEEE.)

Table 3.11: Comparison between the proposed rat-race and other works (Islam Afifi et al [J2], ©2020 IEEE.)

	Technology	Center frequency (GHz)	Bandwidth	return loss (dB)	Isolation (dB)	Amplitude imbalance (dB)
[76]	SIW	13	30%	18	20	-3.35 ± 1.35
[77]	HMSIW	10.15	24.6 %	12	15	-3.8 ± 0.5
[78]	TFSIW	25.7	12.7%	20	20	$-4.3 \pm -$
[79]	RSIW	8	12.5 %	12	20	-3.79 ± 0.5
[80]	RGW	16.5	12.1%	10	20	-
This work	PRGW	30	27.9%	15	16.5	-3.39 ± 0.5

Chapter 4

30 GHz Imaging System: Transmitting and Receiving Antennas Integration

In this chapter, the hardware components of the imaging system are designed, fabricated, and measured. For the transmitting part, a planar differential feeding antenna is designed. Then the rat-race coupler is added to form the transmitting part. For the receiving part, the 3-dB coupler, the crossover, and the 45° phase shifter are combined to form the Butler matrix. Then, a semi-log periodic antenna is designed and added to the Butler matrix to form the receiving part.

4.1 Transmitter: Differential Feeding Antenna

In this section, a wideband differential feeding PRGW planar aperture antenna is designed as the transmitting part of the proposed imaging system. The differential feeding is used to have a stable broadside radiation pattern. Also, capacitive feeding is used to have a wide bandwidth. The use of a planar aperture allows having a high gain with a low profile structure.

The design is based on a planar aperture with a patch in the middle and backed by the mushroom shaped structure of the ridge gap unit cells (Artificial magnetic conductor). The structure is shown in Figure 4.1, where two cross-shaped patches are placed in the middle of the planar aperture, both sides of the top layer, to maintain the E-field density along the aperture, as shown in Figure 4.2. A tapered line and stub matching sections are

used for matching. The optimized dimensions of the proposed antenna and its feeding are in Table 4.1 where the dimensions of the patch at the back of the top layer are larger than that at the front by 0.15 mm. The simulated s-parameters and the realized gain are shown in Figure 4.3. The antenna has a bandwidth of 28.5 % with $S_{11} \leq -10$ dB and a peak gain of 12.39 dBi. Moreover, the 3 dBi gain bandwidth is from 26.1 to 34.1 GHz (26.58%). The drop in the gain at high frequencies is referred to the appearance of the third mode in the aperture of the antenna, as shown in Figure 4.4, which reduces the broadside gain and results in an increase in the sidelobe level.

Table 4.1: The dimensions of the planar differential feeding antenna.

Parameter	L_T	W_T	L_{x1}	L_{y1}	L_{px}
Value (mm)	23.8	25.5	12.45	10.94	11.09
Parameter	L_{py}	W_{px}	W_{py}	L_s	W_s
Value (mm)	4.36	1.7	2.97	5.47	1.68
Parameter	p	d	L_{m1}	L_{m2}	L_{m3}
Value (mm)	0.84	0.3	4.83	1.49	0.94
Parameter	W_{m1}	W_{m2}	W_{m3}	W_{line}	d_{cap}
Value (mm)	0.95	1.33	0.76	1.38	1.5

4.2 Transmitter: Differential Feeding Antenna with Rat-Race Coupler

The designed differential feeding antenna, the rat-race coupler, and the coaxial-to-PRGW transition are combined together to form the transmitting antenna of the imaging system, the isolation port of the rat-race coupler has been terminated with an open stub. The geometry of the transmitting antenna is shown in Figure 4.5. The structure has been fabricated, as shown in Figure 4.6. The multilayer PCB technology has been used to fabricate the ridge layer, the spacer layer(air gap), and the antenna aperture layer. The PCB drilling machine has been used to drill the metal base and cover those hold the connector and then they have been cut by hand tools. The measure and simulated s-parameters and gain are shown in Figure 4.8 where the matching bandwidth is from 25.62 to 34.34 GHz with return loss higher than 10 dB. The peak gain is 12.28 dBi, while

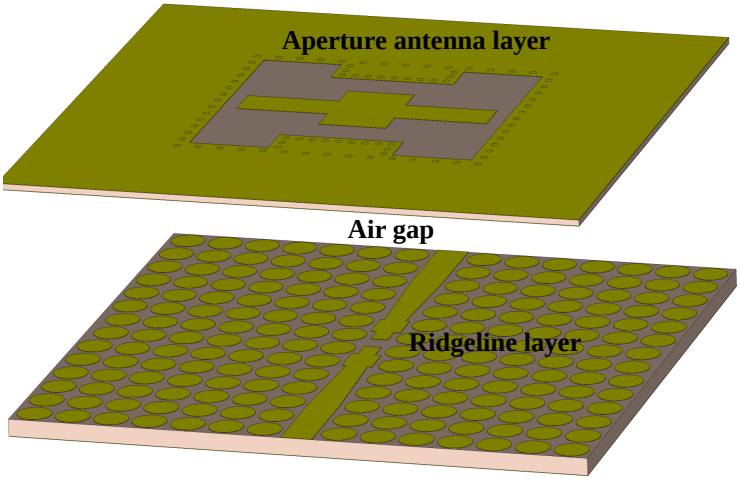

(a)

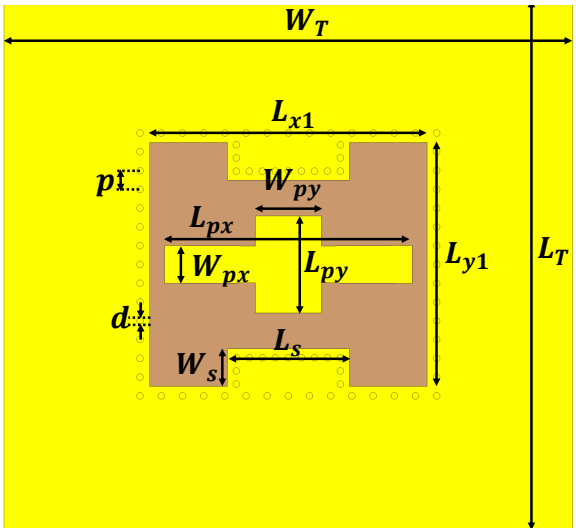

(b)

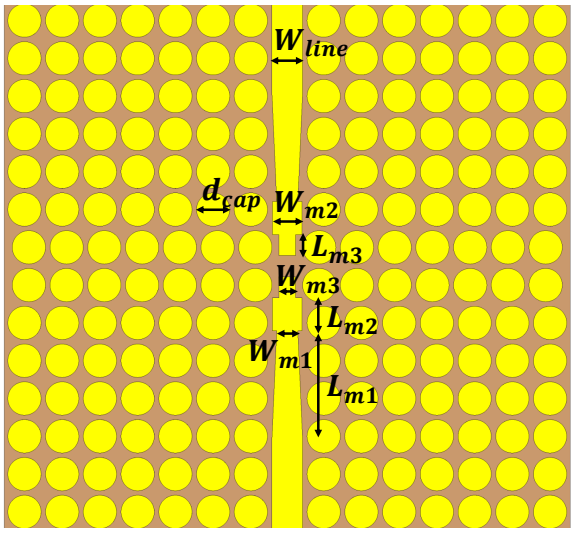

(c)

Figure 4.1: Geometry of the ridge gap planar aperture antenna. (a) The 3d geometry. (b) The top layer. (c) The bottom layer

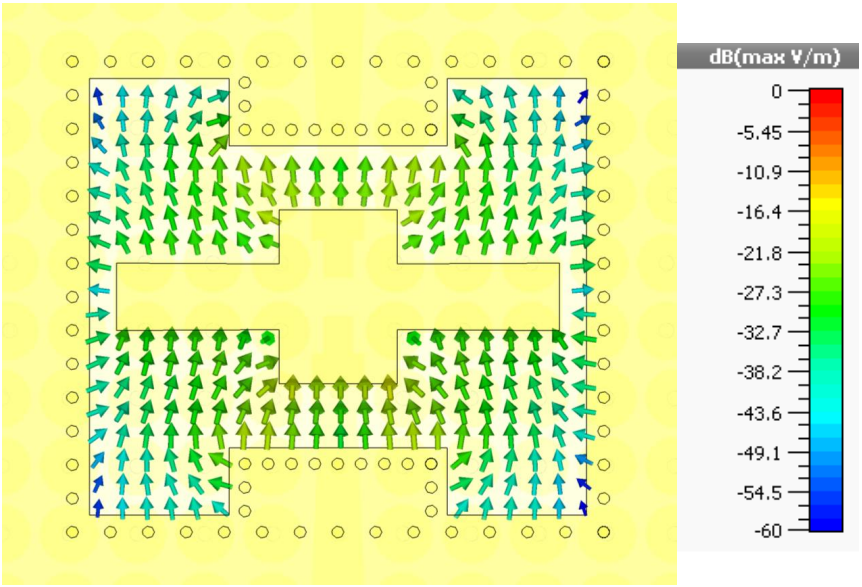

Figure 4.2: The E-field distribution in the aperture area at 30 GHz.

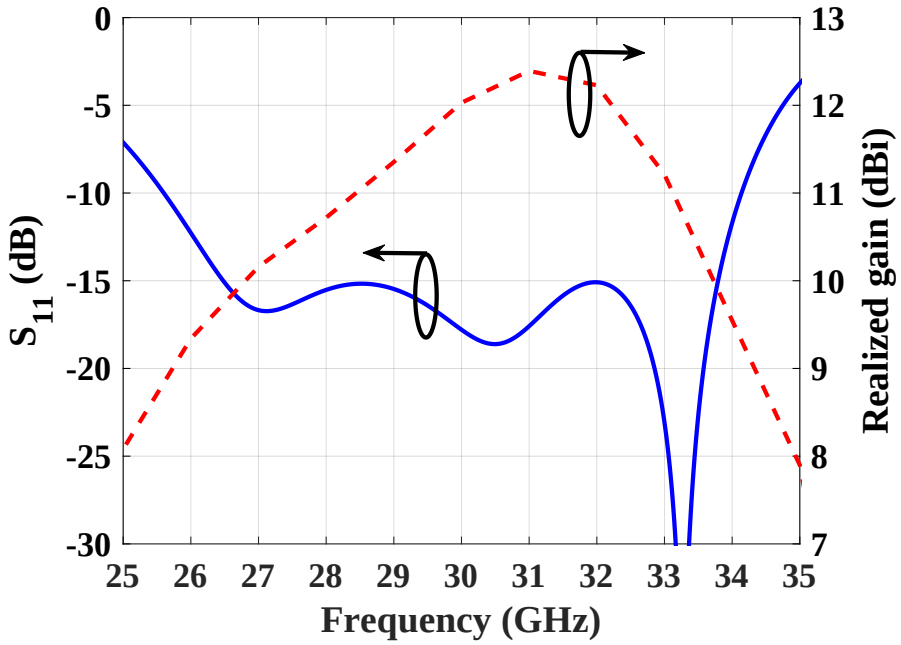

Figure 4.3: The simulated S_{11} and the realized gain for the differential feeding antenna.

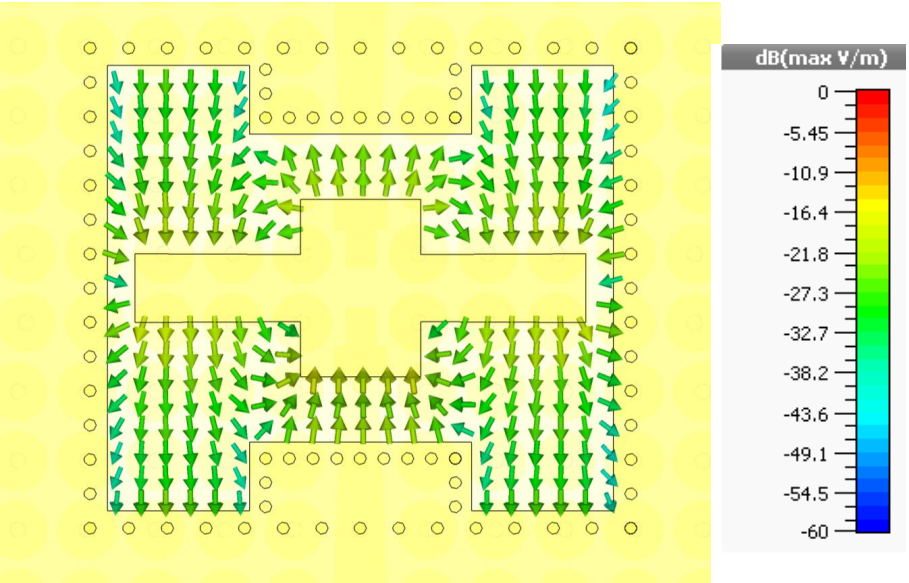

Figure 4.4: The E-field distribution in the aperture area at 33 GHz.

the 3-dB gain bandwidth is from 25.62 to 33.77 GHz. The far field measurement set up is shown in Figure 4.7. The measured and simulated radiation patterns at 28, 30, and 32 GHz are shown in Figure 4.9.

4.3 Receiver: Wideband PRGW Butler Matrix

4.3.1 Design Procedure

The Butler matrix designed in the PRGW technology is presented in this section. The basic components designed in the previous chapter are used to build the Butler matrix. The arrangement of the components follows the architecture shown in Figure 1.1. The critical point is the consistency of the geometric length and the phase matching of the crossover and the phase shifter to have a good performance. The geometry of the proposed Butler matrix is shown in Figure 4.10. There are two sets of equations: one set is for the geometric consistency and the other for the phase consistency. The geometric equations are:

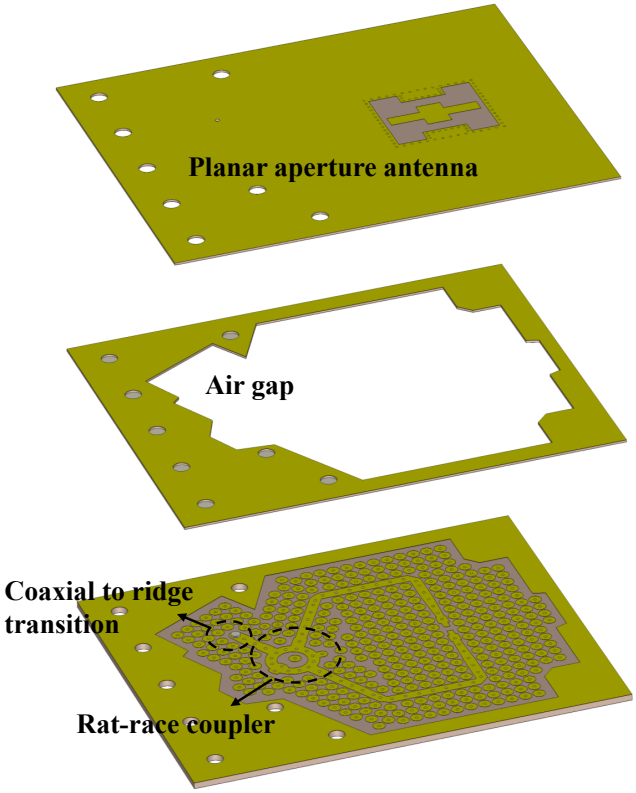

Figure 4.5: The geometry of the differential feeding antenna with the rat-race coupler and coaxial feeding.

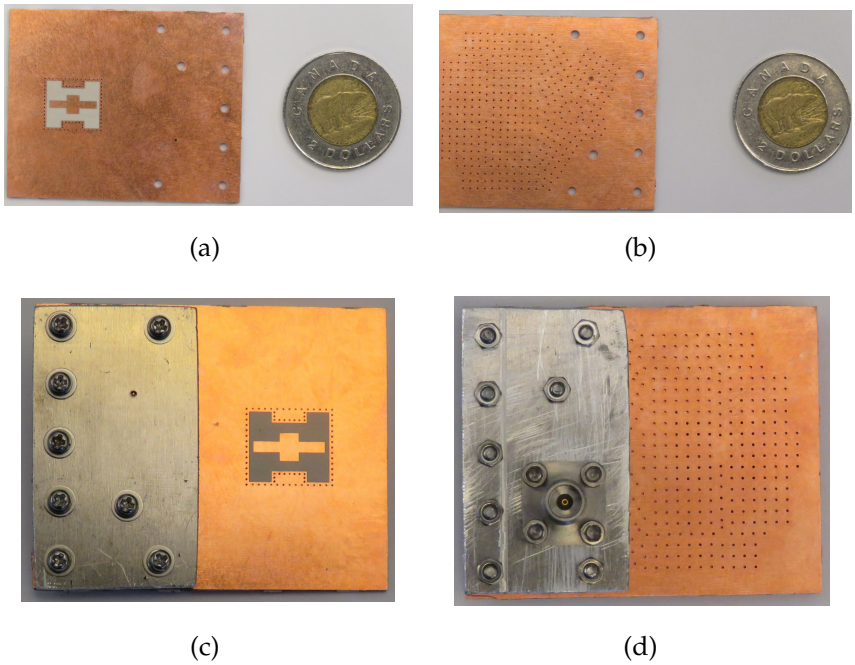

(a) (b)

(c) (d)

Figure 4.6: The fabricated prototype of the differential feeding ridge gap planar aperture antenna. (a) The top view of the multilayer PCB. (b) The bottom view of the multilayer PCB. (c) The top view of the antenna with the top metal holder. (d) The bottom view of the antenna with the bottom holder and coaxial connector.

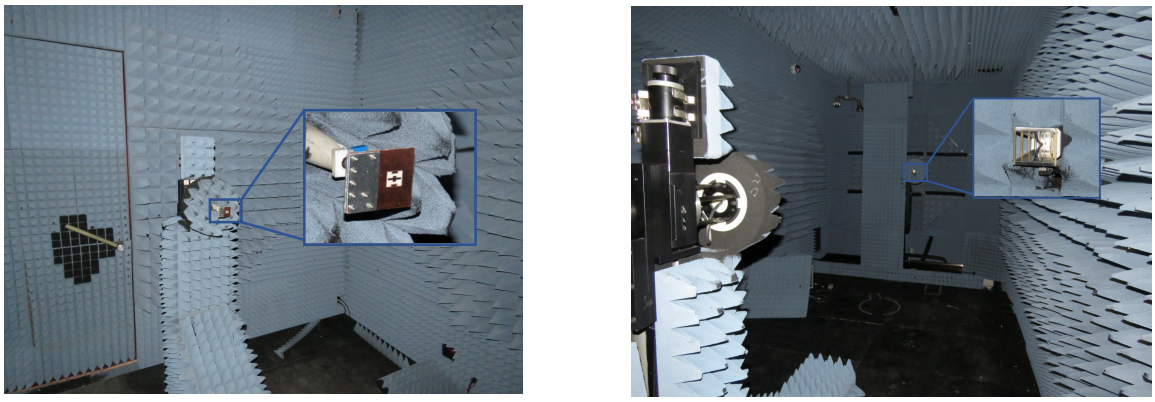

(a) (b)

Figure 4.7: Radiation pattern measurement set up of the differential feeding antenna.

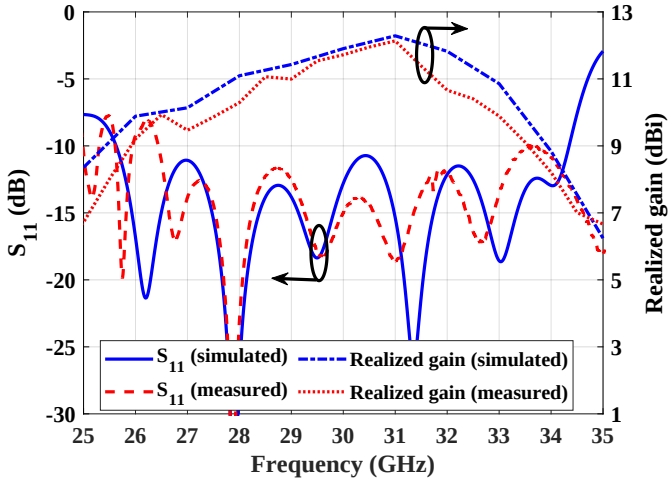

Figure 4.8: The simulated and measured S_{11} and the realized gain for the differential feeding antenna with the rat-race coupler and coaxial feeding.

$$L_{cp}\cos(\pi/4) + L_{pn} = L_{cc}\cos(\pi/4) + \frac{L_{cx}}{2} \tag{4.1}$$

$$(L_{o1} + L_{o2})\cos(\pi/4) + L_{oH} = L_{cc}\cos(\pi/4) + L_{cx} + L_{o3}\cos(\pi/4) \tag{4.2}$$

$$L_{o3}\cos(\pi/4) = d/2 \tag{4.3}$$

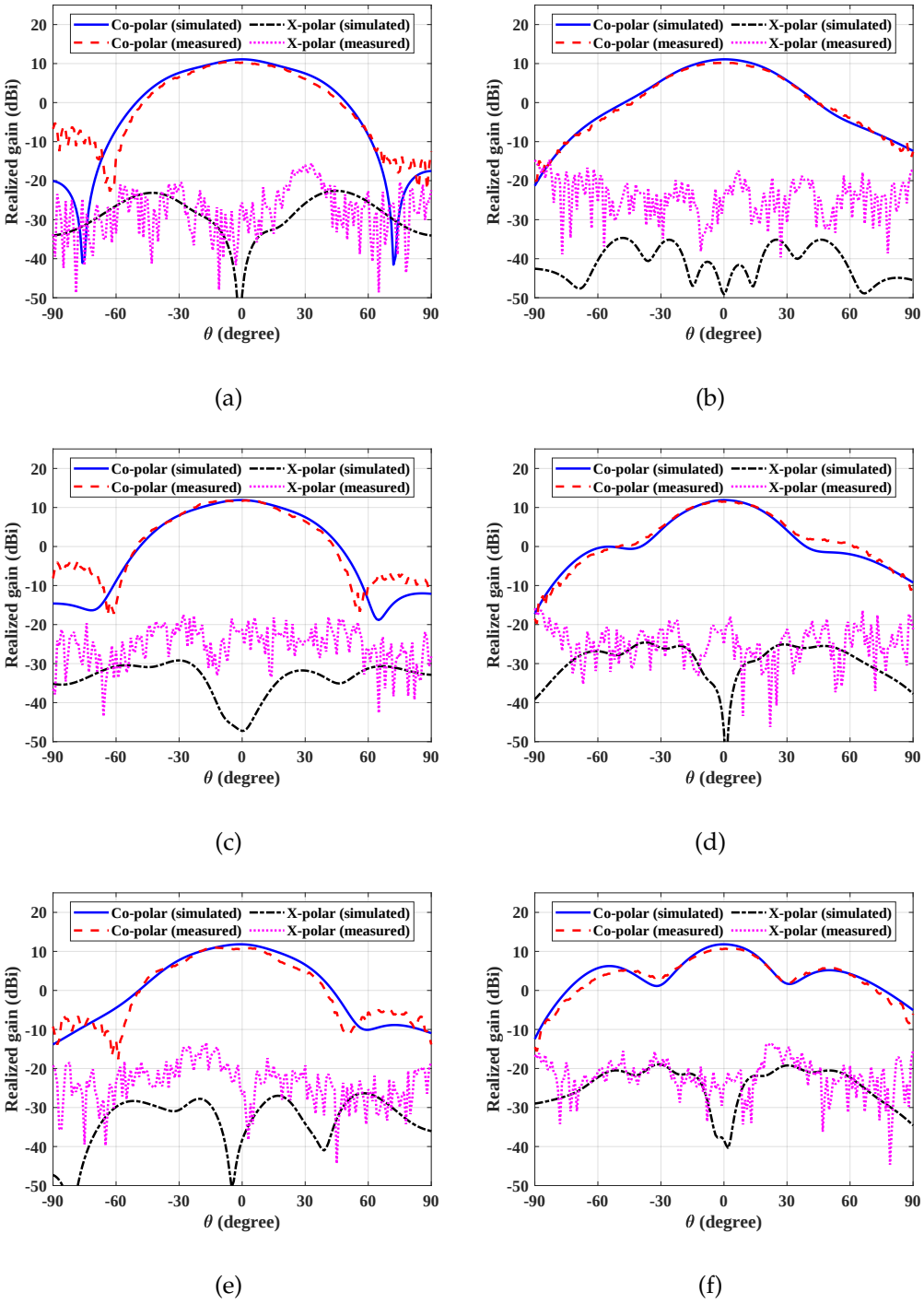

Figure 4.9: Measured and simulated radiation pattern. (a) E-plane radiation pattern at 28 GHz. (b) H-plane radiation pattern at 28 GHz. (c) E-plane radiation pattern at 30 GHz. (d) H-plane radiation pattern at 30 GHz. (e) E-plane radiation pattern at 32 GHz. (f) H-plane radiation pattern at 32 GHz.

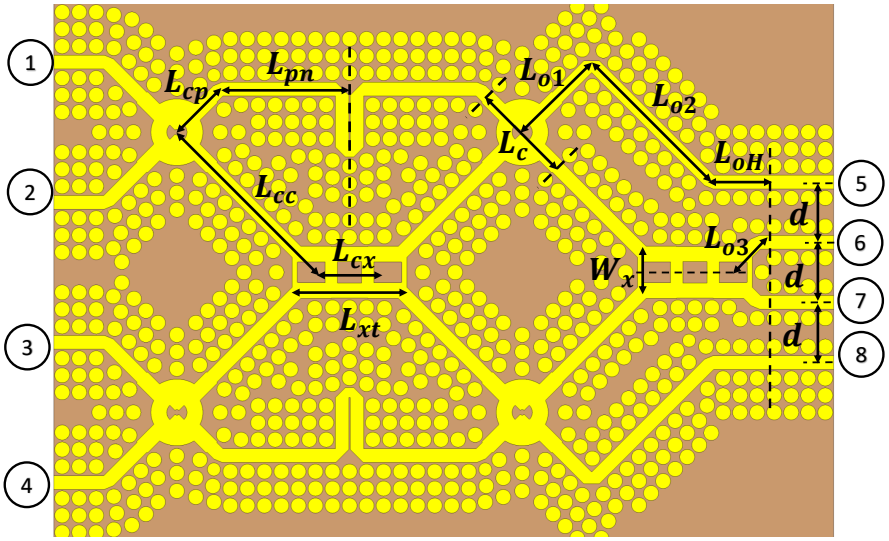

Figure 4.10: The geometry of the Butler matrix (Islam Afifi et al [J3], ©2020 IEEE.)

$$(L_{cc} + L_{o1} - L_{o2})\cos(\pi/4) = \frac{3\,d}{2}. \tag{4.4}$$

The constraints that have to be taken into consideration are:

1) $d > (W_x)$

2) $L_{o1} > (L_c/2)$ to build the coupler

3) $L_{cp} > (L_c/2)$ to build the coupler

4) $(L_{cc} - \frac{L_c}{2})\cos(\pi/4) > \frac{1}{2}(L_{xt} - L_{cx})$ to build the crossover

Equation 4.1 ensures that the output lines of the first coupler (near to the input of the Butler matrix) will reach the second coupler (near to the output of the Butler matrix) with the same x position. Equation 4.2 ensures that the output of the second coupler (near to the output of the Butler matrix) will reach the antenna feeding point at the same x position. Equations 4.3 and 4.4 are used to ensure equal y-spacing (d) between the feeding points of the antennas.

The second set of equations for the phase consistency are:

$$2L_{cp} + 2L_{pn} - 2W_{line2} - s + L_{phase\,eq} = \quad 2\left(L_{cc} - \frac{L_{xt} - L_{cx}}{2\cos(\pi/4)}\right) + L_{x\,phase\,eq} + 1.25 \quad (4.5)$$

$$L_{o1} + L_{o2} + L_{oH} = L_{cc} + L_{o3} - \frac{L_{xt} - L_{cx}}{\cos(\pi/4)} + L_{x\,phase\,eq} \quad (4.6)$$

where $L_{phase\,eq}$ is the length equivalent to the phase shift of the 45° phase shifter and $L_{x\,phase\,eq}$ is the length equivalent to the phase shift of the crossover.

Equation 4.5 ensures that there is a phase shift of 45° between the output lines of the first coupler when reaching the second coupler. Equation 4.6 ensures that the output lines from the second coupler reach the antenna feeding points at the same phase.

Here we have six equations and seven unknowns (L_{cp}, L_{pn}, L_{cc}, L_{o3}, L_{o1}, L_{o2}. and L_{o3}), so we choose one unknown (L_{cp})and solve for the others. These values are shown in Table 4.2

Table 4.2: The dimensions of the Butler matrix configuration (Islam Afifi et al [J3], ©2020 IEEE.)

Parameter	L_{cp}	L_{pn}	L_{cc}	L_{cx}	L_{xt}	L_c
Value(mm)	6.1	12.73	19.78	6.5	10.95	9.88
Parameter	L_{o1}	L_{o2}	L_{o3}	L_{oH}	W_x	d
Value(mm)	9.8	16.85	4.24	4.64	3.65	6

The output phases of the Butler matrix with respect to the input port are in Table 4.3.

Table 4.3: The output phases corresponding to each input port.

		Output port phase			
		5	6	7	8
Input ports	1	$-45°$	$-90°$	$-135°$	$-180°$
	2	$-135°$	$0°$	$-225°$	$-90°$
	3	-90°	$-225°$	$0°$	$-135°$
	4	$-180°$	$-135°$	$-90°$	$-45°$

Figure 4.11 shows the simulated s-parameters of the Butler matrix for the excitation from port 1 and 2, while Figure 4.12 shows the simulated output phase difference between the output ports for each excitation of the input port.

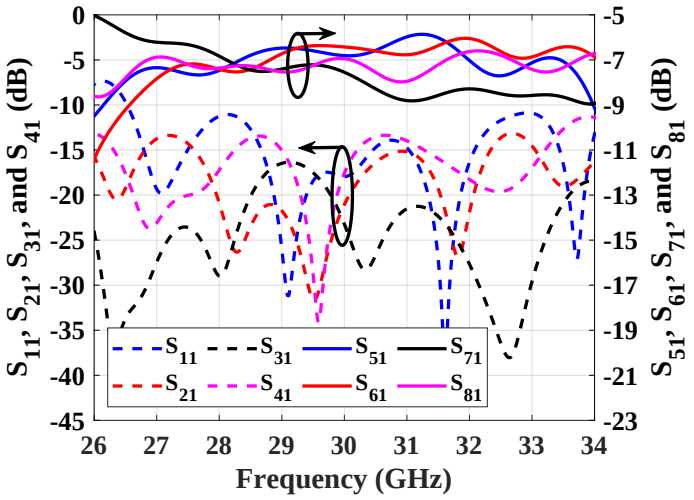

(a)

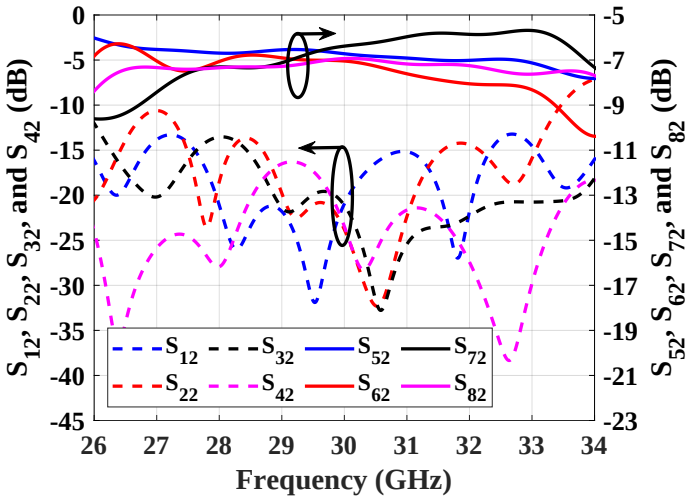

(b)

Figure 4.11: (a) Simulated s-parameters of the Butler matrix, for feeding from Port 1. (b) Simulated s-parameters of the Butler matrix, for feeding from Port 2. (Islam Afifi et al [J3], ©2020 IEEE.)

4.3.2 Discussion

The proposed Butler matrix has many advantages over other reported Butler matrix. It is built in the PRGW technology, which has very low losses and is compatible with PCB

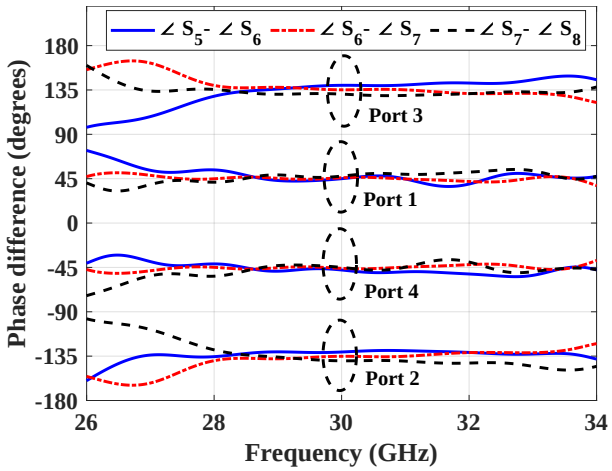

Figure 4.12: Simulated phase difference between the output ports for each excitation of the input ports of the Butler matrix (Islam Afifi et al [J3], ©2020 IEEE.)

technology for easy integration with other system components. Also, it has a wide bandwidth of 20% around 30 GHz. The amplitude imbalance is about ± 1.6 dB over the whole frequency band. The phase error is about $\pm 10^{\circ}$ when feeding from ports 1 and 4 over the whole frequency band. The phases error when feeding from ports 2 and 3 is within $\pm 10^{\circ}$ for the frequency range from 28 to 33 GHz, while there is a higher phase error from 27 to 28 GHz. Its performance overcomes most of the reported works in the 1D scanning standard Butler matrix, as shown in Table 4.4.

Table 4.4: Comparison between 1-D planar Butler matrices working in the millimeter-wave band (Islam Afifi et al [J3], ©2020 IEEE.)

	Technology	size	center frequency (GHz)	Bandwidth	amplitude imbalance (dB)	phase error (degree)
[98]	Microstrip	8×8	25	4%	± 0.5	± 7.7
[99]	Microstrip	4×4	60	4.9%	± 1	-
[95]	SIW	4×4	60	6.67%	± 1.7	± 24
[96]	SIW	4×4	28	7.15%	-	± 15
This work	PRGW	4×4	30	21.25%	± 1.6	± 10

4.4 Receiver: Semi-Log Periodic Antenna Fed by PRGW

A modified version of the semi-log periodic dipole antenna designed in [C1] is implemented using Roger RT6002 ($\varepsilon_r = 2.94$, and $\tan\delta = 0.0012$) with a thickness of 0.254 mm and a copper cladding of 0.017 mm. The geometry of the antenna with the PRGW inputs is shown in Figure 4.13 and the dimensions are listed in Table 4.5. The antenna is designed within an array of four elements to be fed by the 4×4 Butler matrix. However, there was an asymmetry in the radiation pattern for the edge elements. Therefore, two dummy antenna elements are used to have a symmetry radiation pattern for all the array elements. The simulated s-parameters of the antenna array is shown in Figure 4.14 (a) for excitation from port 1, where a bandwidth from 25.85 to 34.86 GHz is achieved with isolation better than 20 dB and $S_{11} \leq -15$ dB. The radiation patterns at different frequencies are shown in Figure 4.14 (b), where the 3-dB beamwidth is ranging from 117° at 27 GHz to 92° at 33 GHz, which is the frequency band of interest.

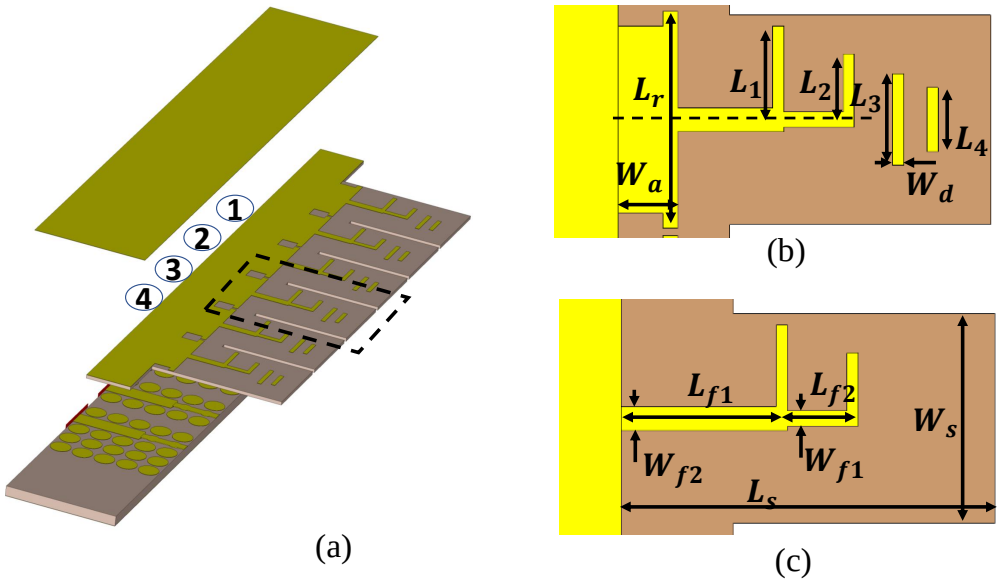

Figure 4.13: The geometry of the radiating elements of the Butler matrix. (a) The antenna array feed by the PRGW lines. (b) The top view of the single antenna element. (c) The bottom view of the single antenna element. (Islam Afifi et al [J3], ©2020 IEEE.)

Table 4.5: The dimensions of the semi-log periodic antenna (Islam Afifi et al [J3], ©2020 IEEE.)

Parameter	W_{f1}	W_{f2}	W_a	W_s	W_d
Value(mm)	0.64	0.412	1.6	5.6	0.3
Parameter	L_s	L_{f1}	L_{f2}	L_r	L_1
Value(mm)	8.4	2.7	1.89	5.8	2.5
Parameter	L_2	L_3	L_4		
Value(mm)	1.75	2.45	1.715		

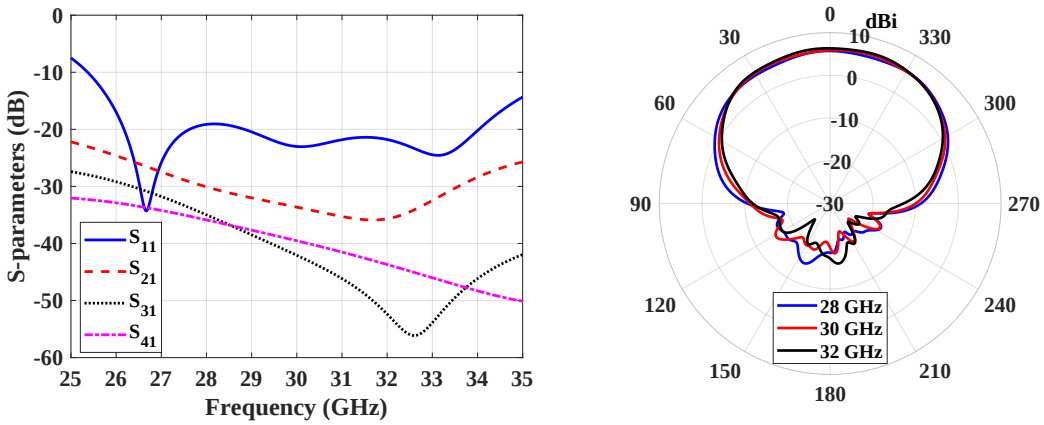

(a) (b)

Figure 4.14: (a) Simulated s-parameters of the antenna array when feeding from port 1 (Islam Afifi et al [J3], ©2020 IEEE.) (b) The radiation pattern of the antenna array when feeding from port 2 at different frequencies (28, 30, 32 GHz).

4.5 Receiver: Beamforming Results

In this section, the antenna and the Butler matrix are combined together to form the beamforming network, as shown in Figure 4.15 (a), where our previously designed coaxial feed [J1] is used for feeding. The main structure is fabricated using the multi-layer PCB technology. Two Aluminum pieces are fabricated to hold the coaxial connectors, and they are attached to the PCB circuit by screws. The fabricated structure is shown in Figure 4.15.

The simulated and measured s-parameters are shown in Figure 4.16. The return losses and isolations are better than 13 dB at the center frequency (30 GHz) and are better than 10 dB for the frequency range from 26.1 to 33.5 GHz. There is a good matching between the measured and simulated results.

The radiation measurement set up is shown in Figure 4.17. The simulated and measured radiation patterns at different frequencies are shown in Figure 4.18, where there is

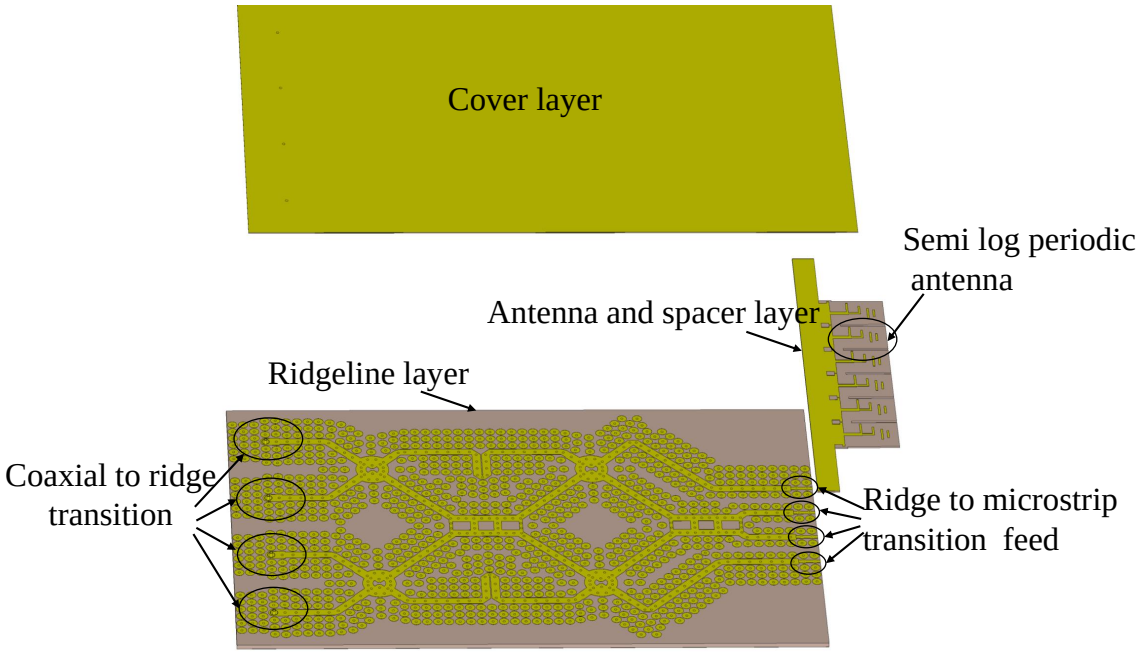

(a)

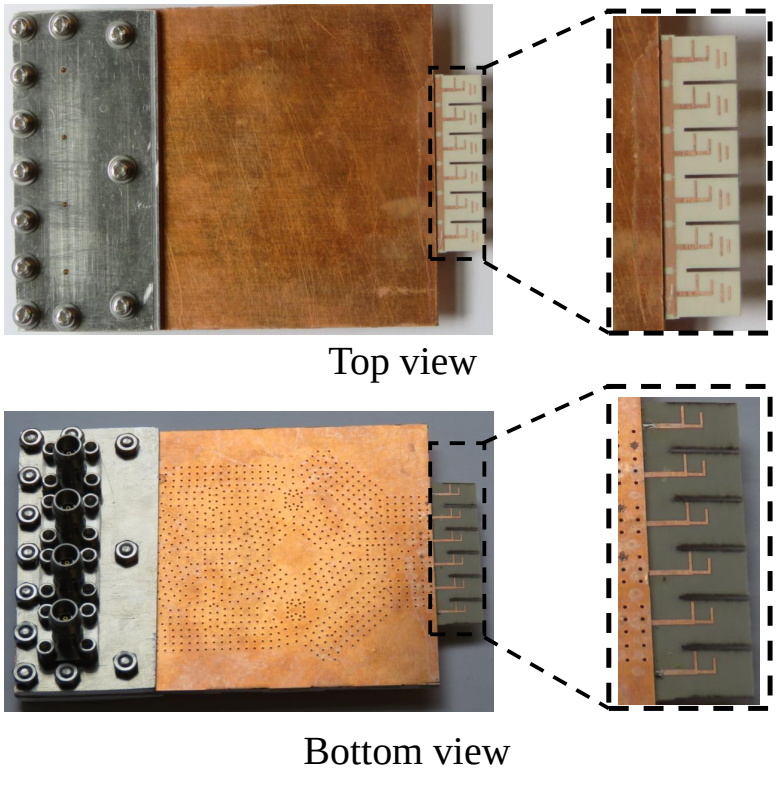

(b)

Figure 4.15: (a) The whole Butler beamforming network consists of the coaxial feed, the Butler matrix, and the antenna array. (b) The fabricated Butler matrix (Islam Afifi et al [J3], ©2020 IEEE.)

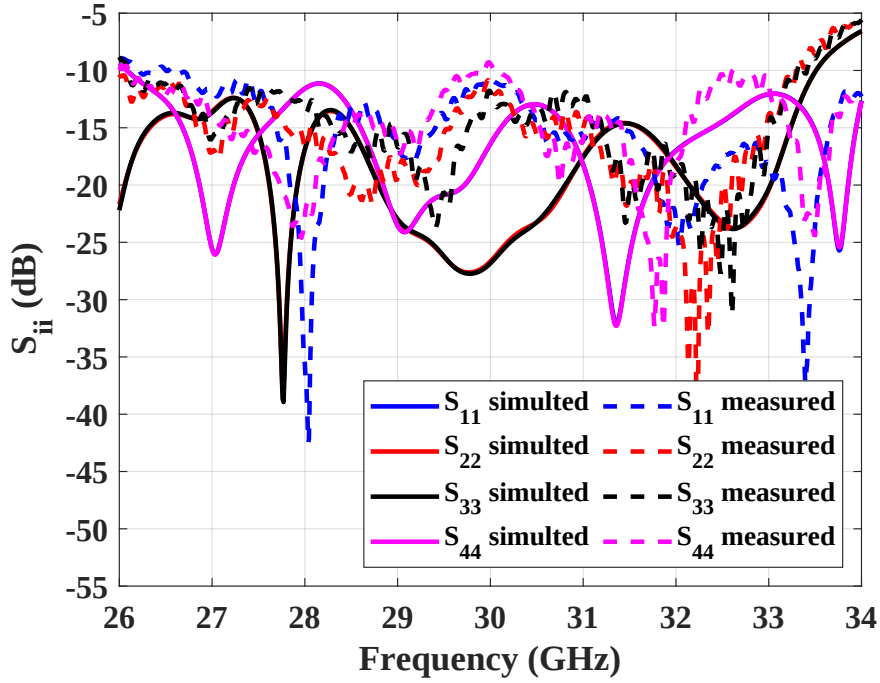

(a)

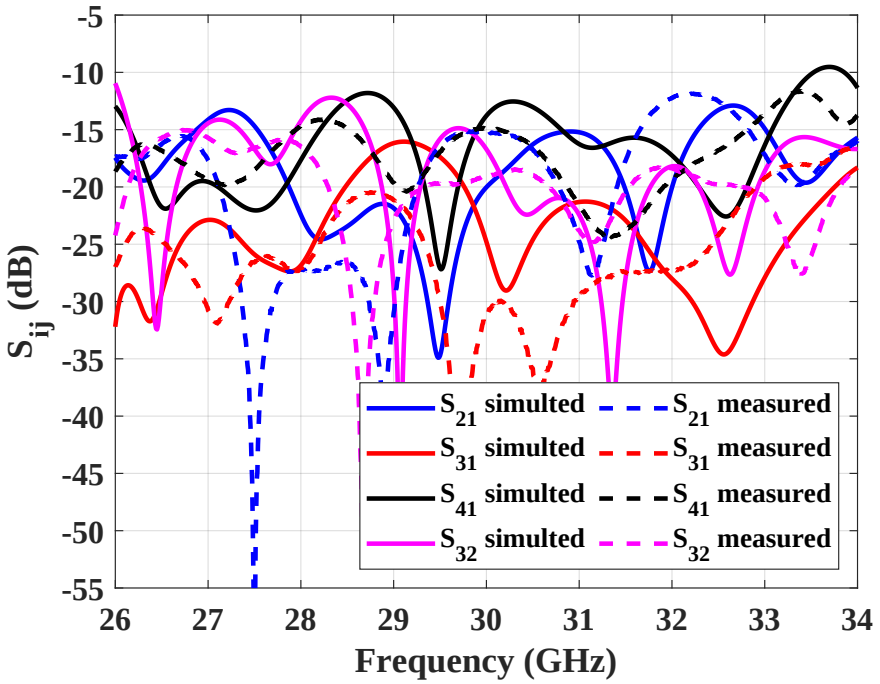

(b)

Figure 4.16: (a) The simulated and measured reflection coefficient of the proposed Butler matrix. (b) The simulated and measured isolations of the proposed Butler matrix. (Islam Afifi et al [J3], ©2020 IEEE.)

a good agreement between the simulated and measured patterns. The beams' directions at the center frequency (30 GHz) are $\pm 13^{\circ}$ for excitation from ports 4 and 1, while it is $\pm 36^{\circ}$ for excitation from ports 2 and 3. The radiation efficiency is better than 78% over the whole frequency band. The gain is ranging from 10.2 to 11.35 dBi for excitation from port 1, and ranging from 8.4 to 10.2 dBi for excitation from port 2, as shown in Figure 4.19. An average gain difference of 1.23 dB between the simulated inner beams and the outer beams is found, which is related to the scan loss and the increase of the sidelobe level for the outer beams.

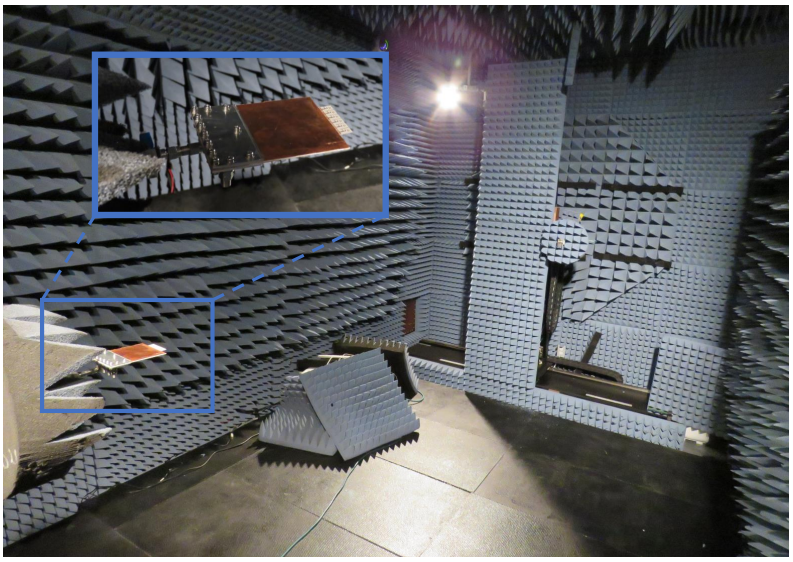

Figure 4.17: Radiation pattern set up in the chamber.

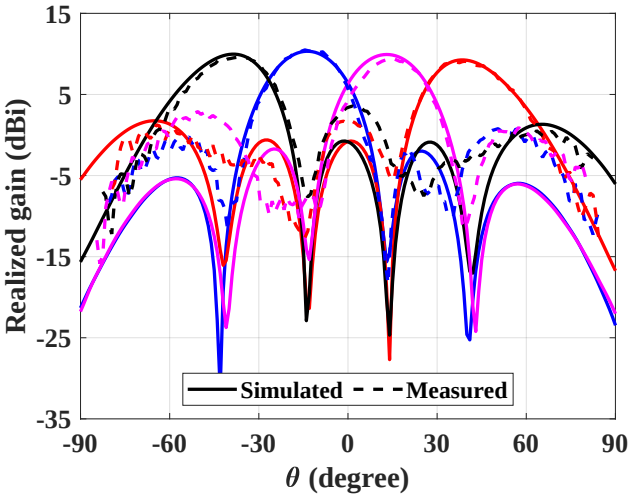

(a)

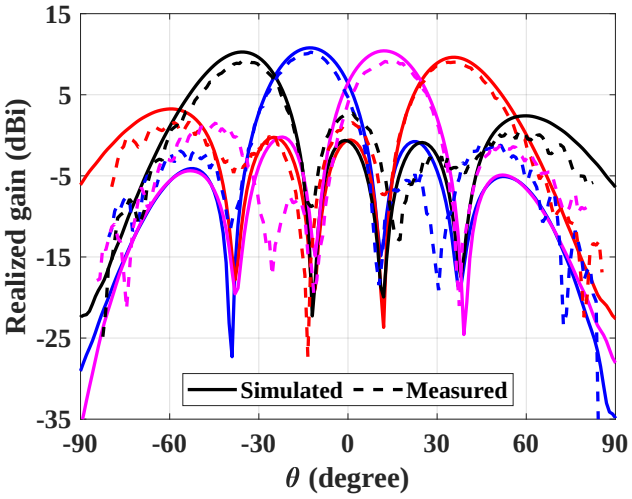

(b)

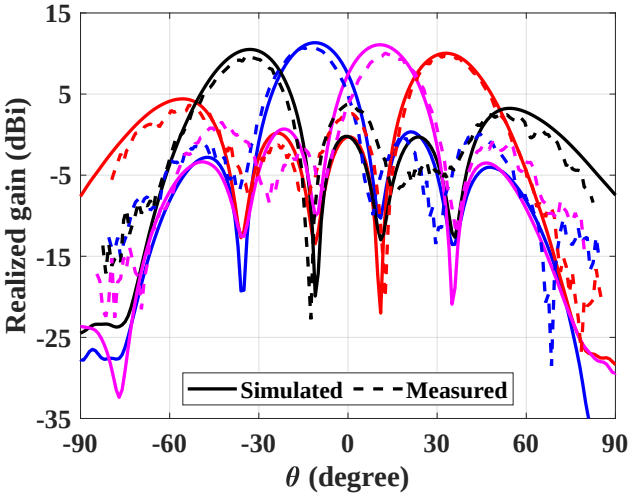

(c)

Figure 4.18: Simulated and measured radiation patterns at different frequencies. (a) 28 GHz. (b) 30 GHz (Islam Afifi et al [J3], ©2020 IEEE.) (c) 32 GHz.

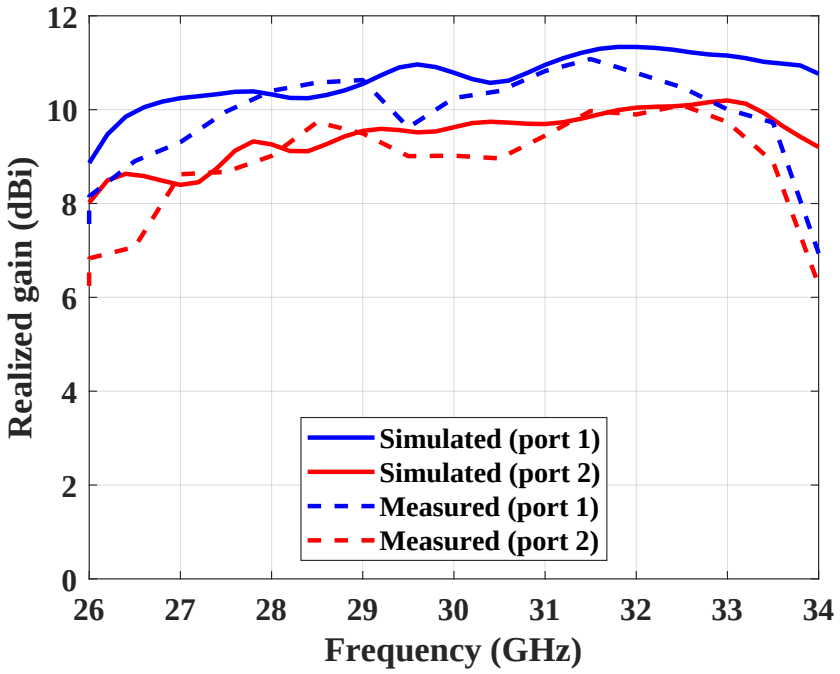

Figure 4.19: Measured and simulated realized gain for excitation from ports 1 and 2 (Islam Afifi et al [J3], ©2020 IEEE.)

Chapter 5

30 GHz Imaging System: Image Reconstruction - Algorithm and Results

In this chapter, the millimeter-wave imaging concept and results are presented. First, the equations for imaging reconstruction are presented. Then, the imaging algorithm has been validated using CST software and measurement. After that, the set up for the proposed imaging system is illustrated. Finally, the proposed imaging system results are shown.

5.1 Imaging Reconstruction Algorithm

There are many imaging reconstruction techniques that can be used with active imaging systems. In [17], the used imaging reconstruction technique depends on using a high gain antenna to measure the reflected signal at a certain position. However, this technique requires a large mechanical scanning area, the same as the imaged area. Another system that uses the transmission signal to reconstruct the image is in [18]. It has the same drawback of needing a large mechanical scanning area. The imaging reconstruction algorithm based on a synthetic aperture radar technique developed by Martin Ryle, who take the Noble prize for this in 1974, is used in this work. This technique has the advantage that the scanning area and the imaging area do not have to be the same size, hence allows the proposed system that has a low mechanical scanning area. The concept stats that using a number of small antennas distributed on an area can give the same angular resolution

of a large antenna occupying the whole area by synchronizing the signals of the small antennas. Figure 5.1 shows the synthetic aperture radar configuration used in this thesis. A planar target is placed with a distance of R from the transmitting and receiving antenna plane. The algorithm presented in this thesis is originated from [1, 12, 144, 145]. The received signal $S_0(x_{Rx}, y_{Rx}, x_{Tx}, y_{Tx})$, at the receiver point $Rx(x_{Rx}, y_{Rx})$ when a transmitter at point $(Tx(x_{Tx}, y_{Tx}))$ illuminates the object, can be calculated as follows

$$S_0(x_{Rx}, y_{Rx}, x_{Tx}, y_{Tx}) = \sum_{x_t \in L_{xT}} \sum_{y_t \in L_{yT}} f(x_t, y_t) \times e^{-jk_0\left(\sqrt{(x_t - x_{Rx})^2 + (y_t - y_{Rx})^2 + R^2} + \sqrt{(x_t - x_{Tx})^2 + (y_t - y_{Tx})^2 + R^2}\right)} \quad (5.1)$$

where x_t and y_t are the coordinates of the target point, $f(x_t, y_t)$ is the reflection of the target at point (x_t, y_t), k_0 is the wavenumber, R is the distance between the target plane and the transmitter and receiver plane, L_{xT} is the length of the target in the x-direction, L_{yT} is the length of the target in the y-direction, x_{Rx} and y_{Rx} are the coordinates of the receiving antenna, and x_{Tx} and y_{Tx} are the coordinates of the transmitting antenna. Using the following equation from reference [12], the target reflection $f(x_t, y_t)$ is calculated

$$f(x_t, y_t) = \sum_{x_{Rx} \in L_x} \sum_{y_{Rx} \in L_y} S_0(x_{Rx}, y_{Rx}, x_{Tx}, y_{Tx}) \times e^{jk_0(\sqrt{(x_t - x_{Rx})^2 + (y_t - y_{Rx})^2 + R^2} + \sqrt{(x_t - x_{Tx})^2 + (y_t - y_{Tx})^2 + R^2})} \quad (5.2)$$

where L_x and L_y are the lengths of the receiver scanning area in x and y-directions, respectively.

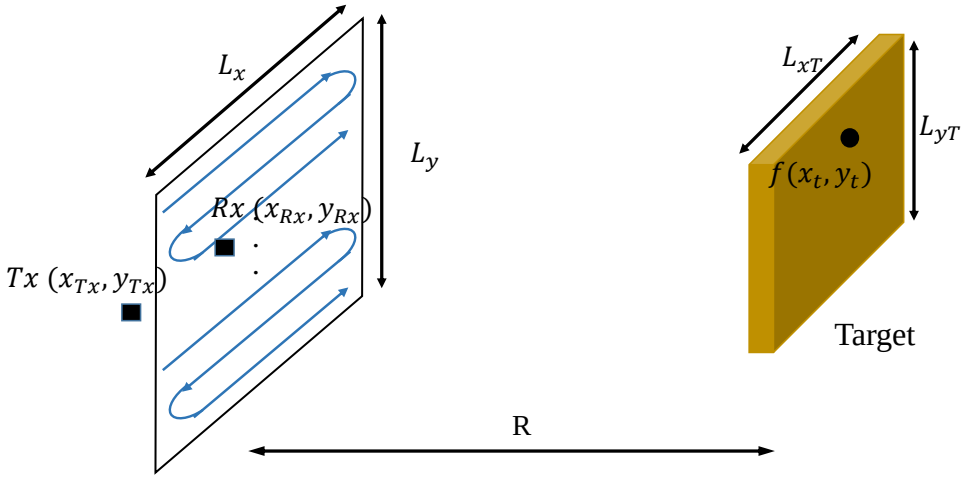

Figure 5.1: Synthetic aperture radar configuration.

5.2 Preliminarily Results: Reconstruction Algorithm

Millimeter-wave imaging is implemented either by using mono-static or bi-static techniques. In this thesis, the bi-static is used. For the proof of concept and validating the imaging algorithm, the mono-static case is used first as the validation of the used coding. From the simulation (CST), two open ended rectangular waveguides are used, one as the transmitter and the other as the receiver. Figure 5.2 shows the geometry of the PEC imaged objects, where the distance between the object plane and the TX and RX plane is 147 mm. The imaging area is 280 mm$\times$280 mm, while the TX and RX are moving with a step of $\lambda_0/4$ at 30 GHz. The collected data are shown in Figure 5.3 (a). After collecting the data, the synthetic aperture technique is used to produce the millimeter-wave image, as shown in Figure 5.3 (b).

After the mono-static concept has been validated by the simulation, the implementation of it in the lab is presented, as shown in Figures 5.4 and 5.5. Two log periodic antennas (as that of the Butler matrix antenna) are used as the transmitter and the receiver and moved by a step of 1.5 mm in a 300 mm $\times$ 300 mm area. The distance between the imaged object and the transmitter/receiver plane is 155 mm. It is shown that a small circle of diameter 6 mm can be observed.

For the bi-static case, a simulation has been carried out in CST. The transmitter is fixed

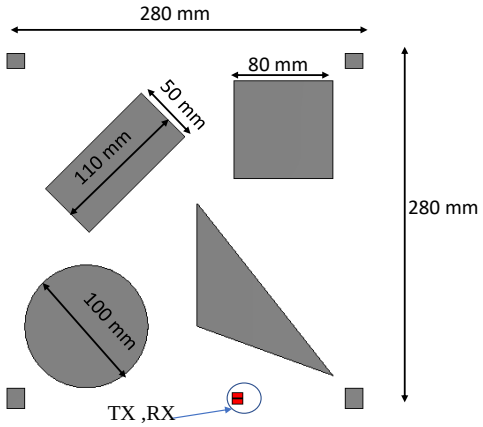

Figure 5.2: Geometry of the imaged objects in the simulation.

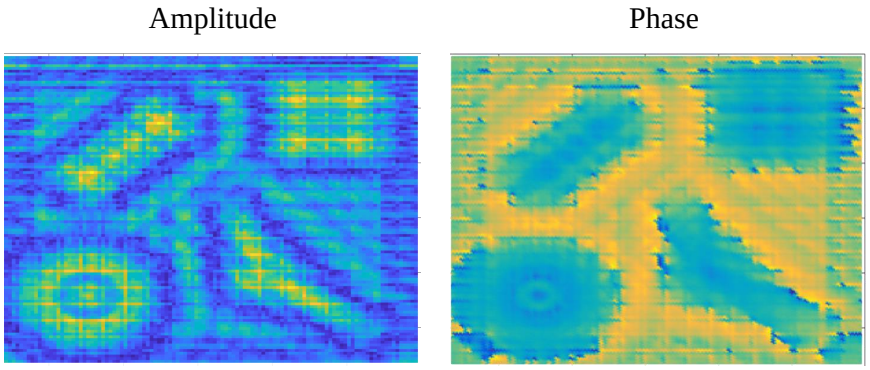

(a)

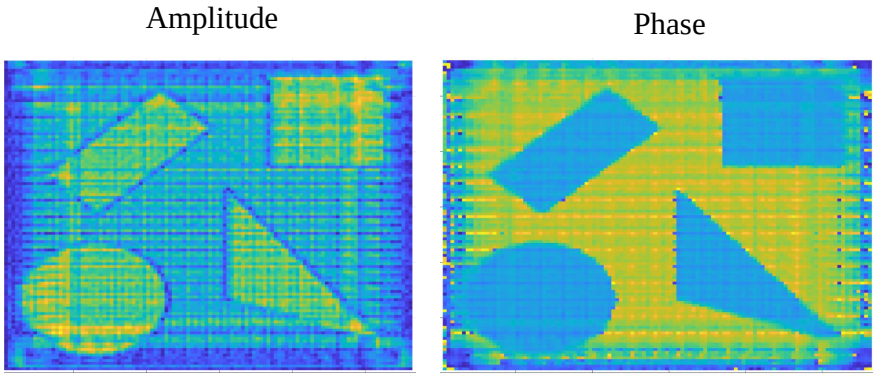

(b)

Figure 5.3: (a) Raw data. (b) synthetic image data.

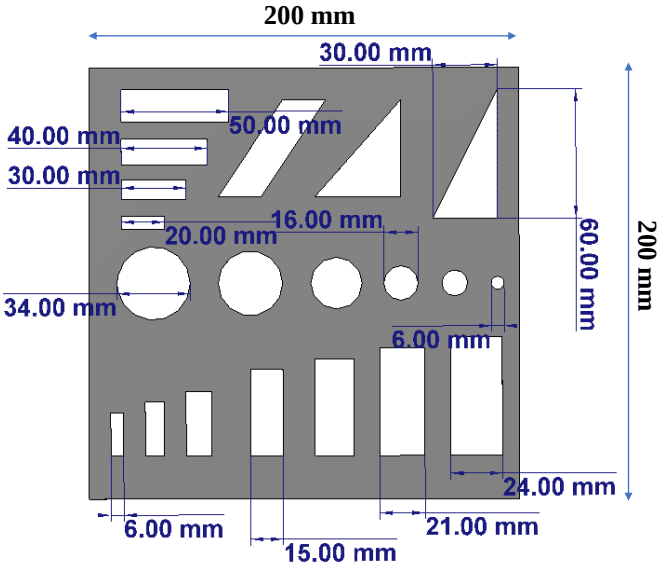

Figure 5.4: Geometry of the fabricated object for imaging.

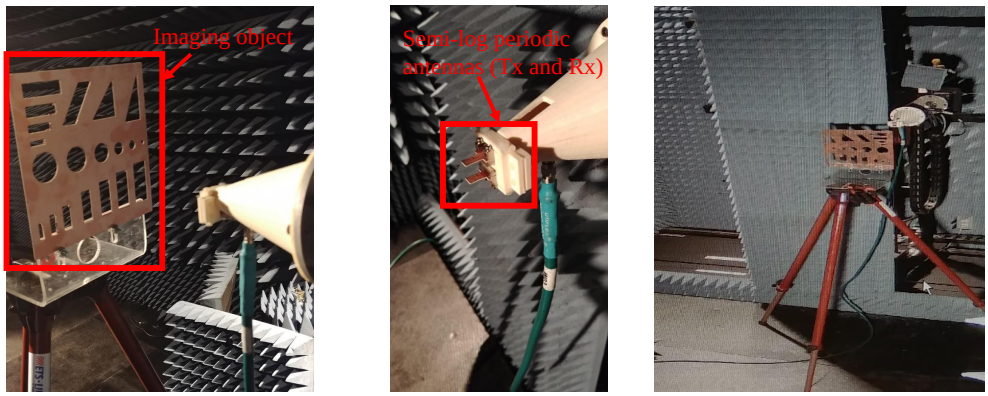

Figure 5.5: Imaging experimental setup.

at a certain position while the receiver is moving in xy-plane. In the simulation set up, both the transmitter and the receiver antennas are tilted by a certain angle to image the desired part of the object. The setup and the results are shown in Figure 5.7. It is clear that the bi-static can be used to image offset areas, which is used in our proposed imaging system. The resolution is not high in this case as it is just introduced as a test (the scanning area of the receiver is small, and hence low resolution is obtained).

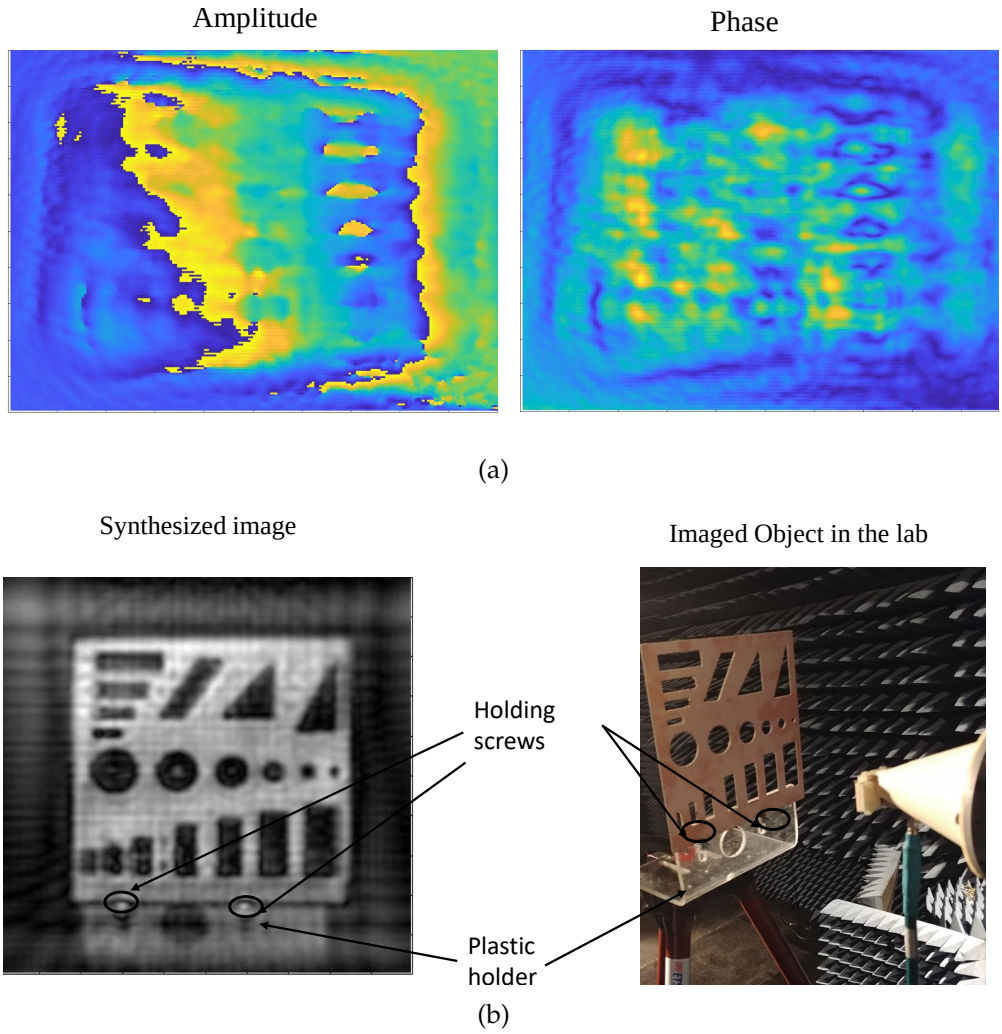

Figure 5.6: Measurement of mono-static imaging. (a) Raw data. (b) synthetic image data.

5.3 Imaging Results

In this section, the imaging system set up for the proposed system is illustrated as a first step. Then, the results of the imaging system are presented. After that, a solution to improve the image quality by using a technique similar to the super resolution technique is presented. Finally, a comparison between the mono-static and the bi-static imaging is presented.

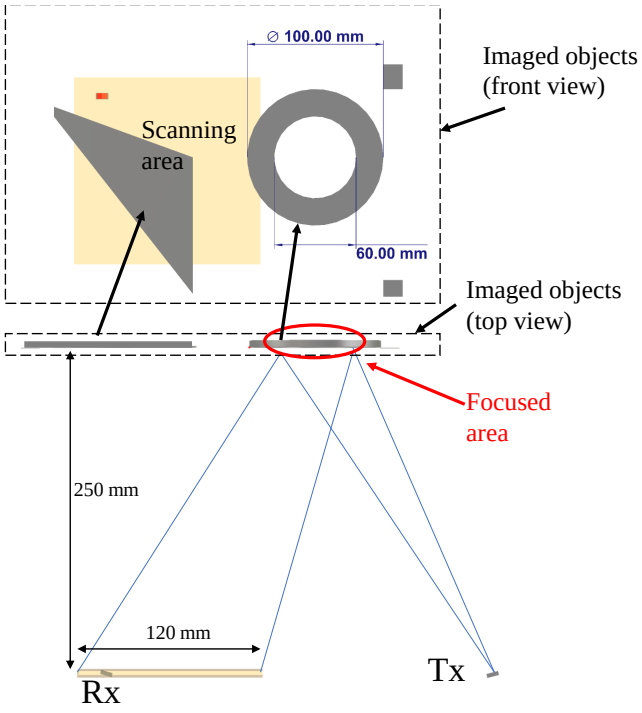

(a)

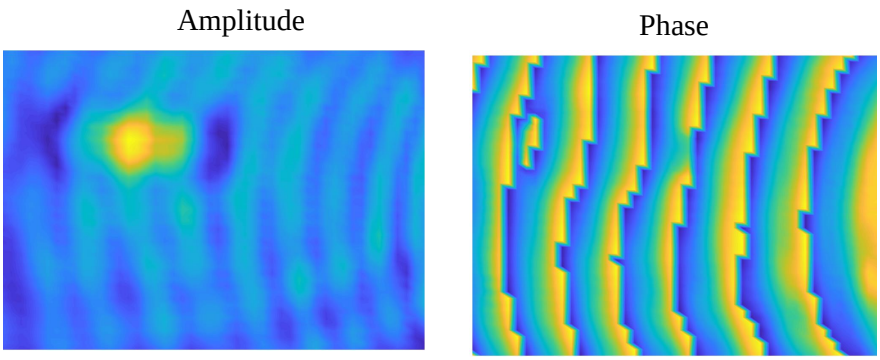

(b)

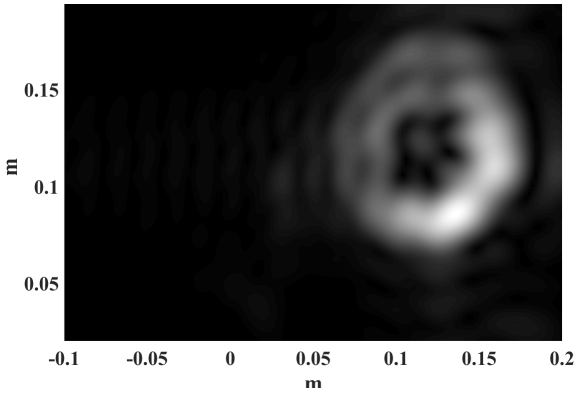

(c)

Figure 5.7: Simulation of bi-static imaging. (a) Geometry and set up. (b) Raw data. (c) Resulted image.

5.3.1 Imaging System Set up

In this part, the imaging system set up is presented. Figure 5.8 shows the positions of the transmitter antennas and the scanning area that the receiver is moving in to collect the reflected signals. Also, Figure 5.8 shows the division of the imaging scene into eight parts. The aim of the proposed work is to be able to image an area of $1m \times 2m$ that is suitable for a full body scan. However, due to the available chamber size limitation, the proposed system is implemented to image an area of $0.6m \times 1.2m$.

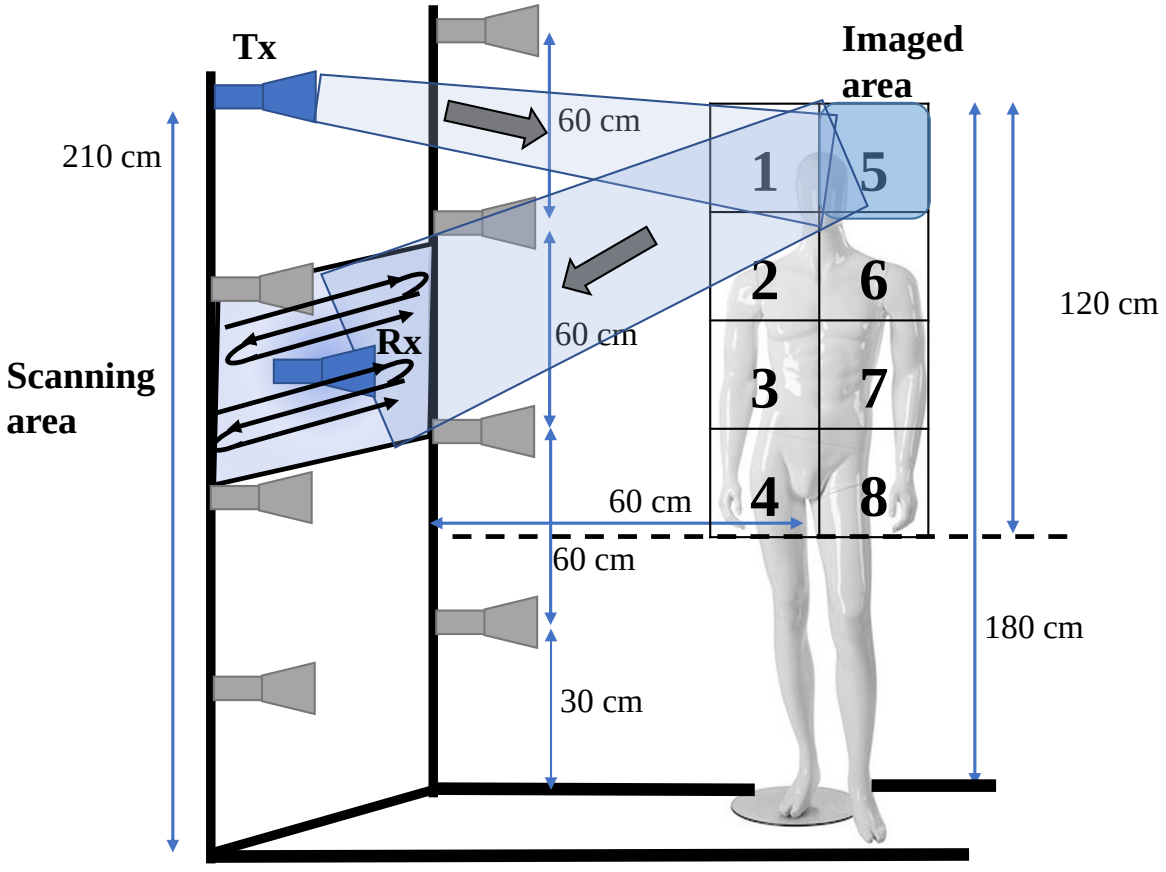

Figure 5.8: Proposed system set up. (a) Dimension of and positions of the system. (b) The division of the imaging area.

The data collecting procedure is:

1. Fixing the transmitting antennas at fixed positions.

2. Connecting the antennas to the PNA, one port for one of the transmitting antennas and the other to the corresponding port of Butler matrix in the receiving antenna.

3. Using the mechanical system (NSI 5913), the performance network analyzer (PNA), and the NSI2000 software available in the micro/millimeter-wave lab to set up the scanning and obtain the data.

4. Repeat for the number of transmitting antennas.

5. Produce the final millimeter-wave image by combining it from the different images (produced before in the sense that each transmitter illuminates a part from the image).

Figure 5.9 illustrates the system set up in the millimeter-wave chamber. The transmitter antenna is the differential feeding aperture antenna designed in the previous chapter. It is mounted on a long stick and can be moved along it to fix it at certain positions as shown in Figure 5.8. Also, it is attached to the stick by a stepped gear that allows rotation by a step of 12°, which allows fixing the antenna angle at $\pm 12^\circ$ and $\pm 36^\circ$ that are close to the theoretical values $\pm 11.25^\circ$ and $\pm 36.88^\circ$, respectively. The receiving antenna is the Butler matrix designed in Chapter 4, where each port is used to image two parts of the imaged object. The receiving antenna is moved in the xy-plane with a step of 2 mm that is less than $\lambda_0/4$ at the center frequency (30 GHz). Figure 5.10 shows the imaged object which is a fiberglass mannequin with a knife and a plastic pistol (covered by Aluminum foil) attached to it. Figure 5.11 shows the inner structure of the mannequin legs as the inner supporter will affect the resulted MMW images.

The data collection is done in two steps. First, the object is placed in front of the imaging system at a certain distance. Then, the data is collected using the PNA and the NSI2000 software. After that, the object is removed, and another data collection has been done. The first measurement has both the scattering from the object in addition to the background scattering and the coupling between the transmitter and the receiver antennas. The second measurement contains the background scattering and the coupling

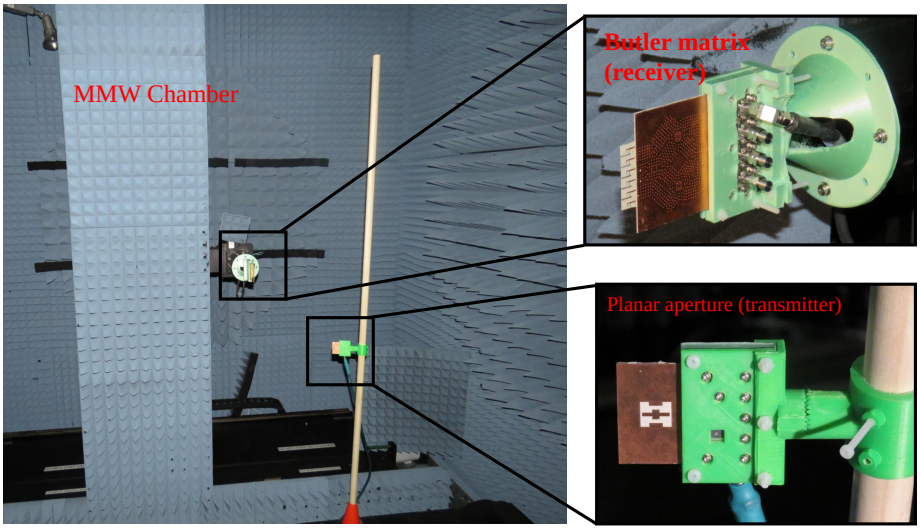

Figure 5.9: Imaging system set up in the chamber.

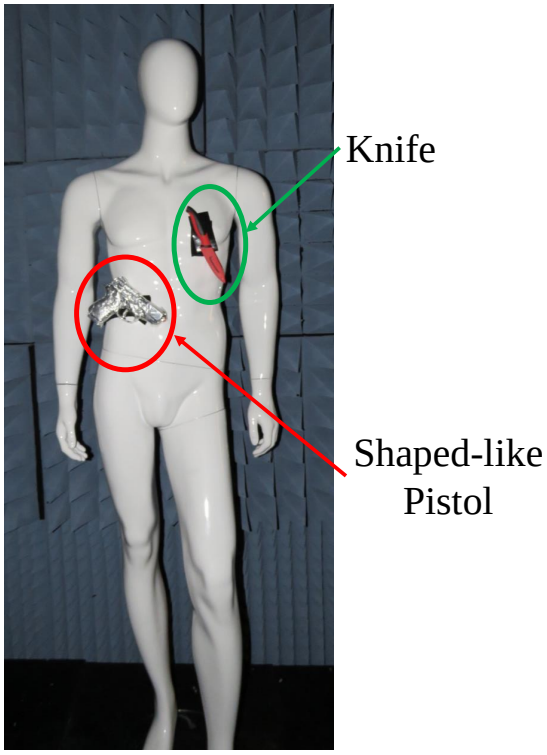

Figure 5.10: Imaging object, a mannequin with a knife and a plastic pistol covered by Aluminum foil.

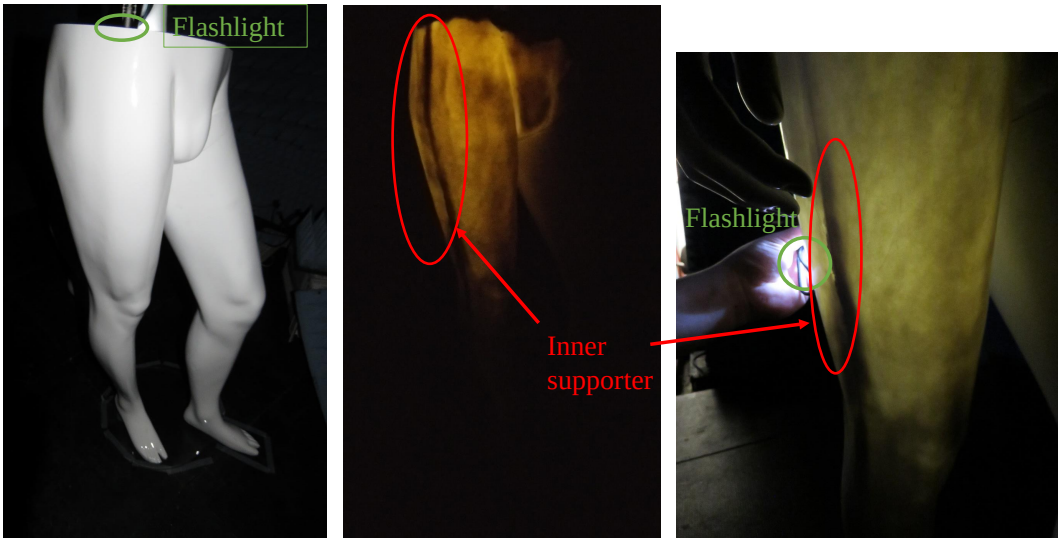

Figure 5.11: The inner structure of the mannequin legs (shows the presence of supporter).

between the transmitter and the receiver antennas only. In order to have the data for the scattering from the object only, a subtraction between the two measurements is done. Figures 5.12, and 5.13 show the measured data ((a) and (b)) and the subtraction data (c) when part 2 is illuminated at 30.5 GHz, for the amplitude and the phase, respectively.

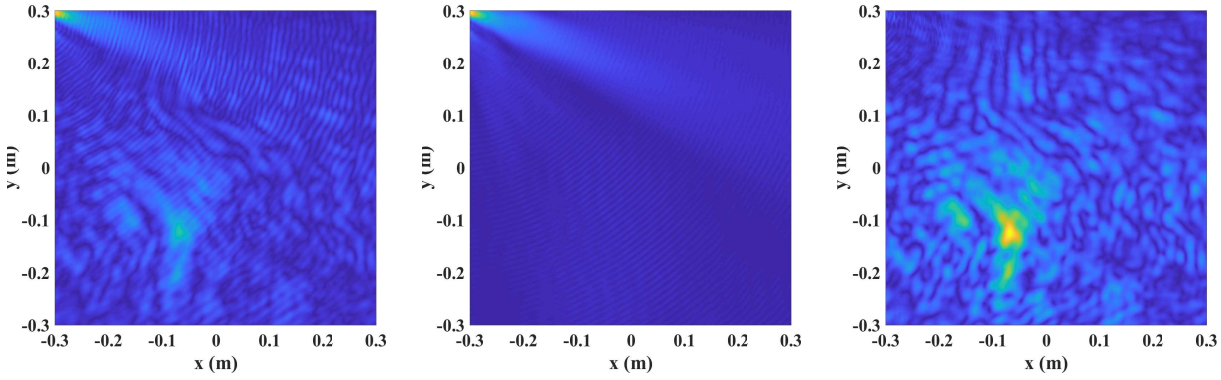

(a) (b) (c)

Figure 5.12: Absolute value of data at 30.5 GHz when part 2 is measured. (a) Measured data. (b) Calibration data. (c) Calibrated data.

5.3.2 Imaging Using Frequency Multiplexing and Beamforming

In this part, the imaging of the scene is divided into eight parts; each is imaged by a different frequency. As the resolution depends on the operating frequency, the outer parts

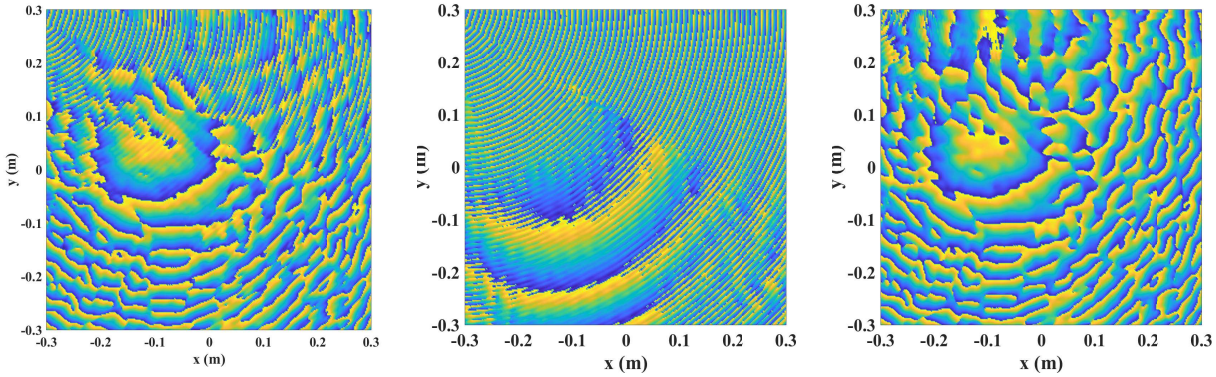

(a) (b) (c)

Figure 5.13: Phase of data at 30.5 GHz when part 2 is measured. (a) Measured data. (b) Calibration data. (c) Calibrated data.

of the scene (less important parts) are imaged by low frequencies, while the inner parts (most important parts) are imaged with high frequencies. The frequencies used for the outer parts 1, 4, 5, and 8 are 28.5, 29.5, 29, and 30 GHz, respectively. The frequencies used for the inner parts 2, 3, 6, and 7 are 30.5, 31, 31.5, and 32 GHz, respectively. The reconstructed images at different frequencies for different parts are shown in Figure 5.14, while Figure 5.15 shows the full image of the scene by combining parts from each image in Figure 5.14.

5.3.3 Imaging by Summation over Frequencies

The reconstruction of the image using summation over multiply frequencies is used to have a better resolution than a single frequency image. That is similar to the case of the super resolution reconstruction (SRR) technique [146] in which multiply low resolution images with a small shift are used to obtain a high resolution image. The reconstructed images for different parts of the image scene after summation over frequencies from 27.5 to 32.5 GHz with 0.5 GHz spacing are presented in Figure 5.16. Figure 5.17 shows the full image of the scene by combining parts from each image in Figure 5.16.

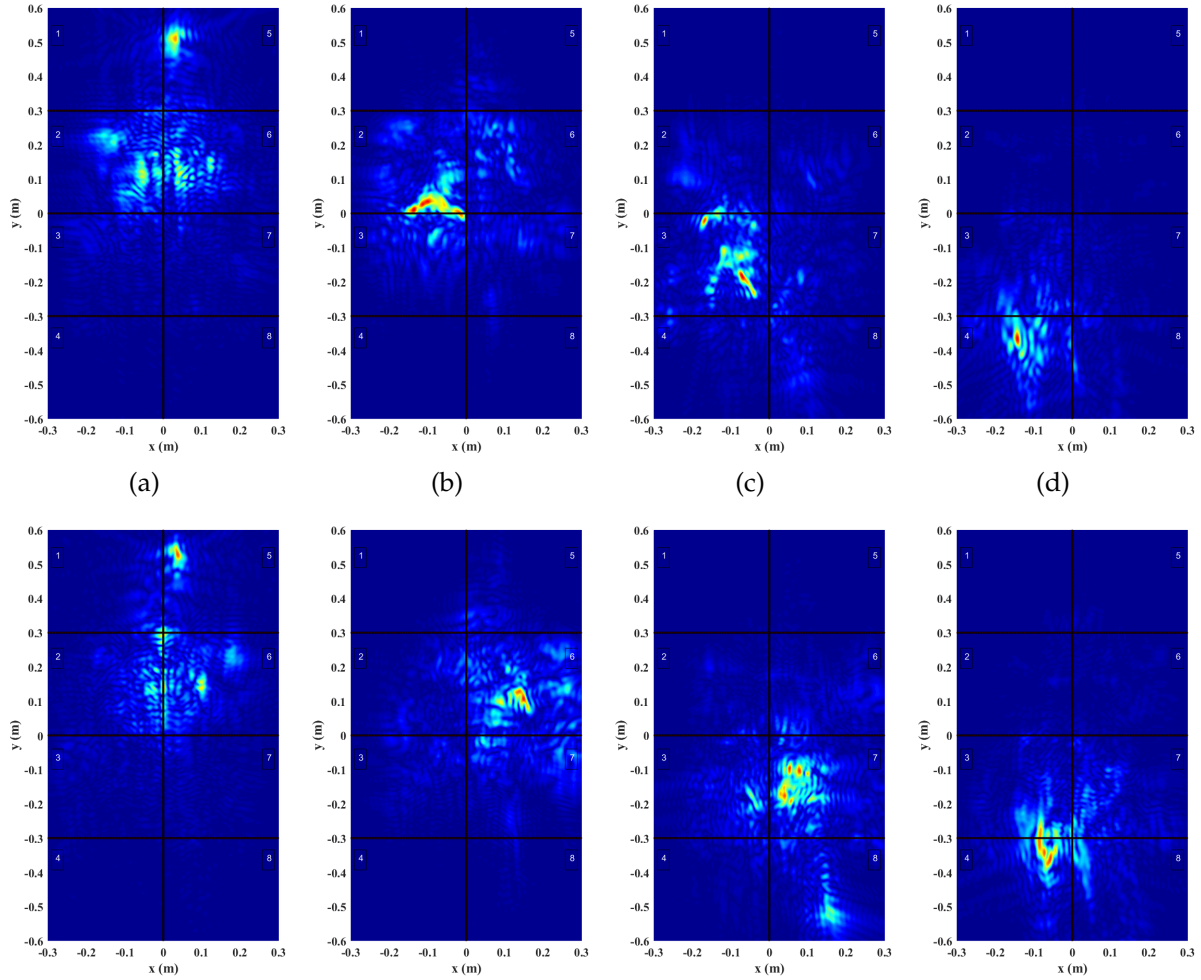

Figure 5.14: Resulted image from each part at a single frequency. (a) Part 1 at 28.5 GHz. (b) Part 2 at 30.5 GHz. (c) Part 3 at 31 GHz. (d) Part 4 at 29.5 GHz. (e) Part 5 at 29 GHz. (f) Part 6 at 31.5 GHz. (g) Part 7 at 32 GHz. (h) Part 8 at 30 GHz.

5.3.4 Mono-Static Imaging

The mono-static imaging setup of the mannequin is shown in Figure 5.18. Two semi-log periodic antennas, as those used in the Butler matrix, are used as the transmitting and receiving antennas. The imaged area is $0.6m \times 1.2m$, which is the same as the scanning area. The collected data is shown in Figure 5.19 for the amplitude and the phase. The reconstructed image at 33 GHz is shown in Figure 5.20 where the knife and the covered plastic pistol are shown.

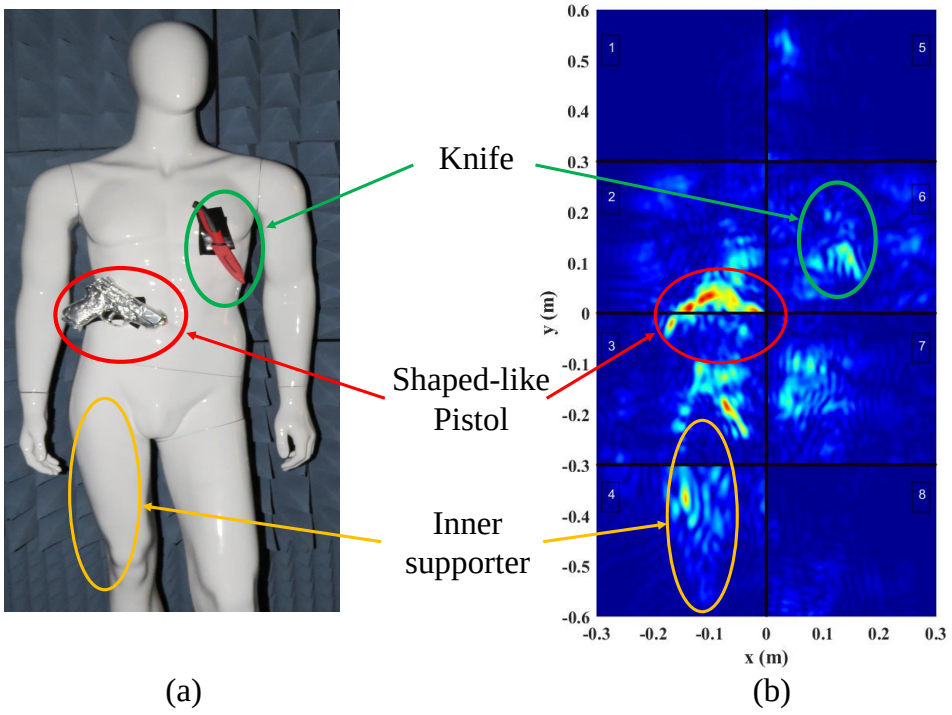

Figure 5.15: (a) Original image. (b) Resulted image by combining all the parts (in the sense that one part is taken from each image.)

5.4 Discussion of The Imaging System

The proposed imaging system has many advantages compared to the conventional mono-static imaging systems. The mechanical scanning area of the receiving antenna is half that of the mono-static, $0.6m \times 0.6m$ compared to $1.2m \times 0.6m$ in mono-static. This saves a lot of time as the mechanical scanning is the most time consuming part of the imaging system. Regarding the computational resources, the proposed system requires $8 \times 150 \times 150 \times 300 \times 300$ operations (300×300 for the scanning area, 150×150 for the imaged area, and 8 for the number of parts of the imaging area) while the mono-static requires $600 \times 300 \times 600 \times 300$ operations (600×300 for each scanning and imaging areas). This means that the proposed system has a number of operations equal to half of the mono-static case.

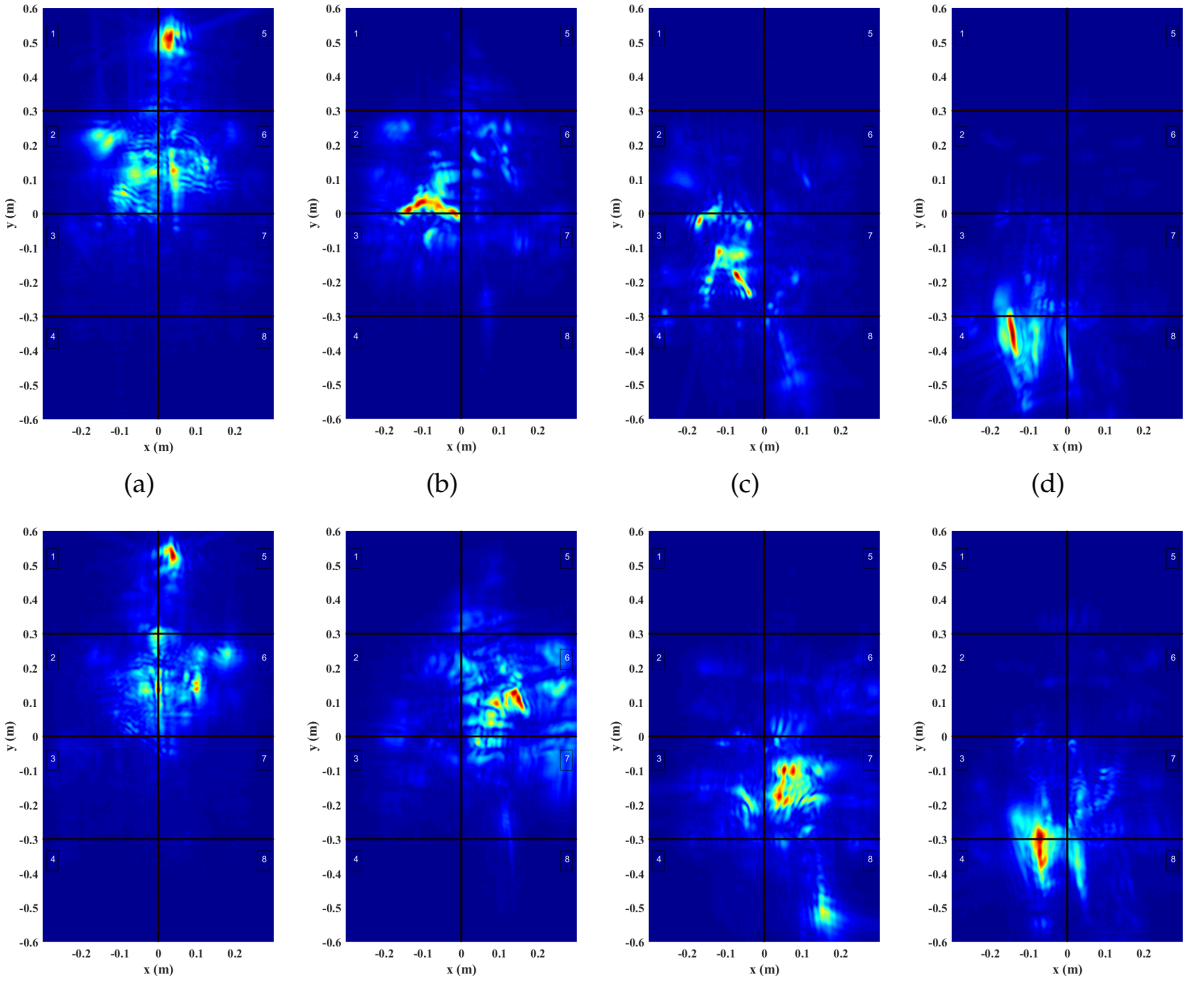

Figure 5.16: Resulted image from each part by summation over frequencies from 27.5 to 32.5 GHz by 0.5 GHz step. (a) Part 1. (b) Part 2. (c) Part 3. (d) Part 4. (e) Part 5. (f) Part 6. (g) Part 7. (h) Part 8.

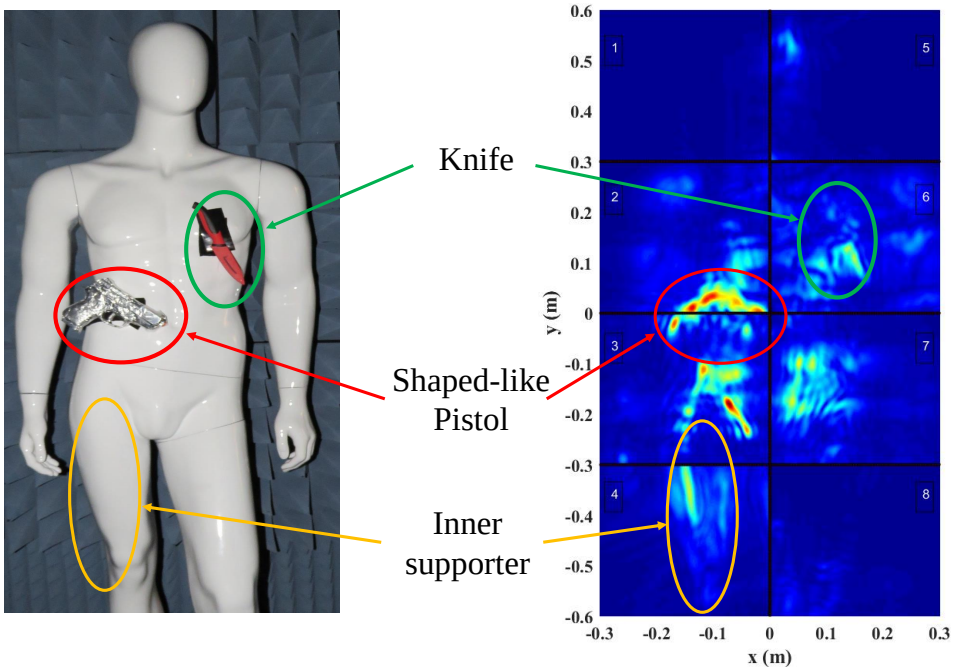

(a) (b)

Figure 5.17: (a) Original image. (b) Resulted image by combining all the parts after summing over all frequencies from 27.5 to 32.5 GHz with 0.5 GHz step (in the sense that one part is taken from each image.)

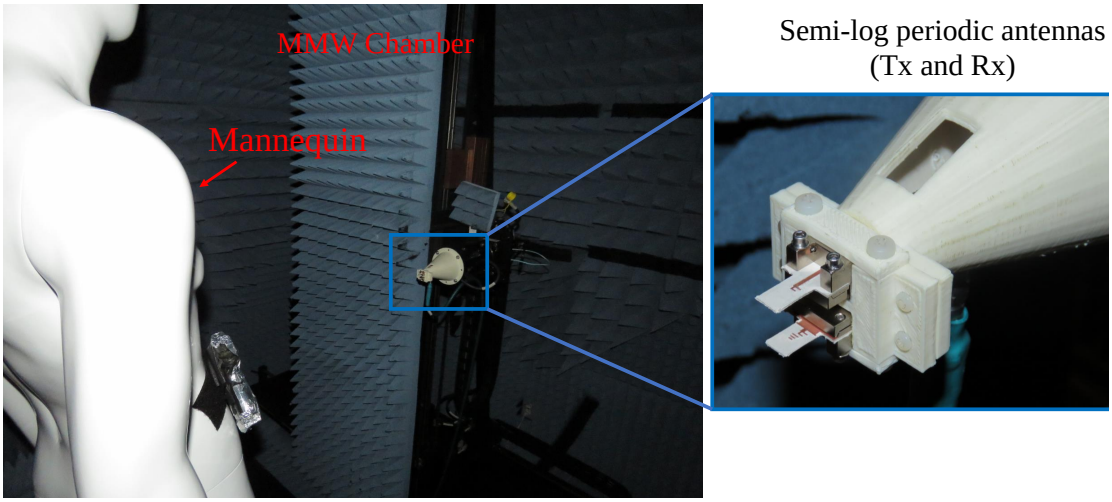

Figure 5.18: Mono-static imaging set up in the Chamber.

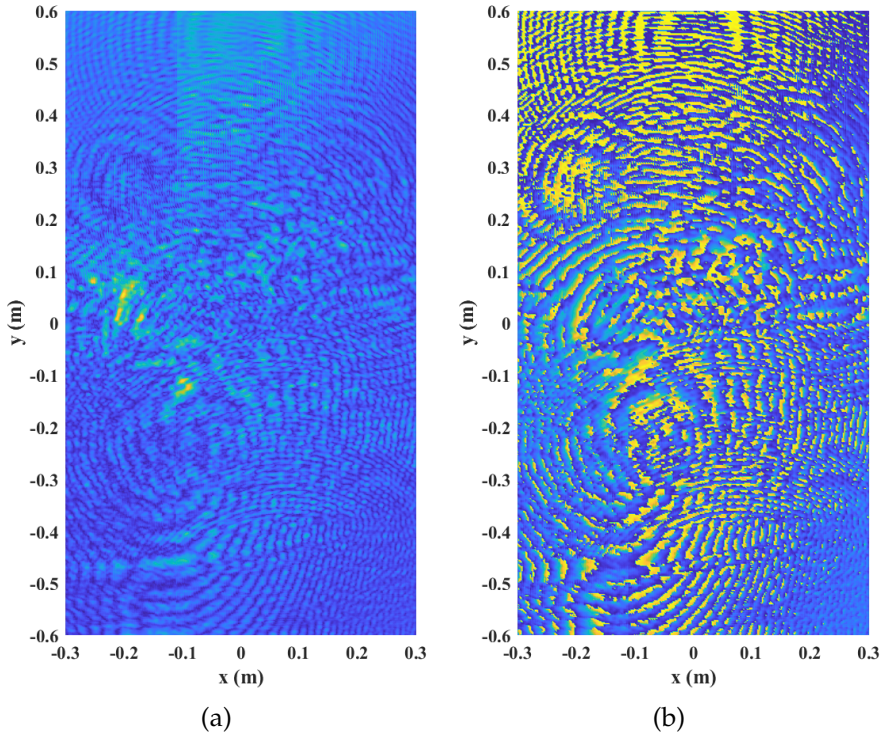

Figure 5.19: Collected raw data of mono-static imaging at 33 GHz. (a) Amplitude. (b) Phase.

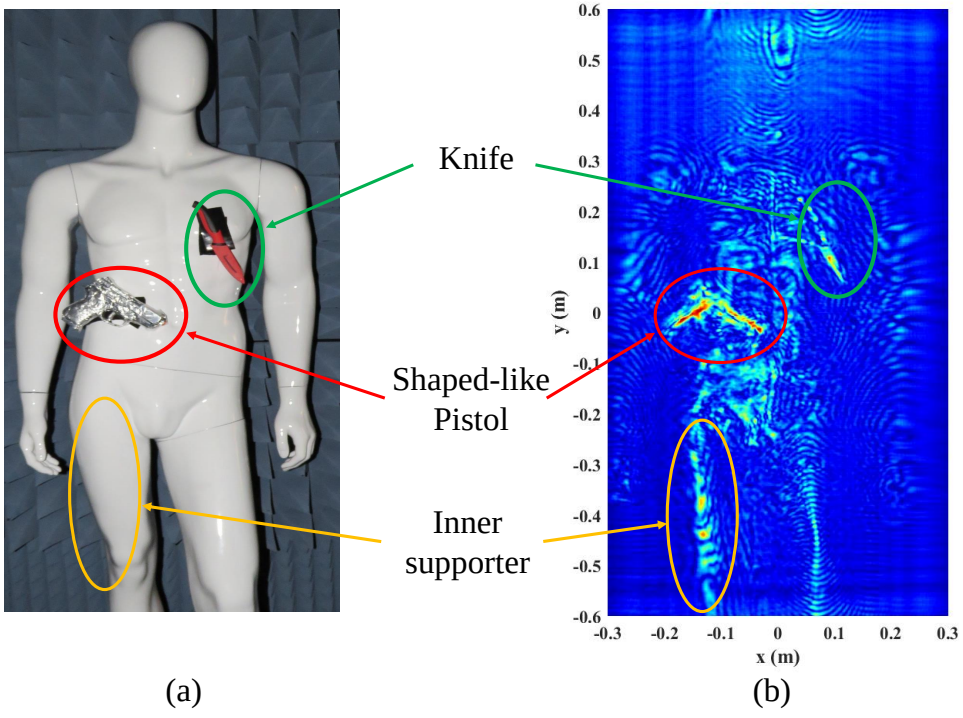

Figure 5.20: (a) Original image. (b) Resulted image using mono-static imaging at 33 GHz.

Chapter 6

Conclusion and future work

6.1 Conclusion

A millimeter-wave imaging system is designed and implemented for a wide-viewing angle. It consists of three parts: 1) the MMW components and antennas, 2) the mechanical scanning system, and 3) the imagining reconstruction algorithm.

The millimeter-wave components and antennas of the imaging system are designed to operate at 30 GHz with a wideband performance. The printed ridge gap waveguide technology is used to reduce the radiation and dielectric losses in the designed structures. A wideband coaxial to ridge gap transition is designed, fabricated, and measured to feed these structures. The design procedure and the equivalent circuit model are presented here for the ideal case with PMC and PEC boundary conditions, realized using bandgap unit cells for both the metal and printed RGW. The wideband coaxial to ridge gap transition, even with its very small size, covers an octave band with very small size and incurs very low losses compared to other approaches that are either bulky in size or that introduce some losses, as in the microstrip transitions. The designed transition has a 59.22% bandwidth with $S_{11} \leq -10$ dB and $S_{21} \geq -0.5$ dB.

For the transmitting part of the imaging system, a moderate gain differential feeding planar antenna is designed in PRGW. Its feeding network is designed using a rat-race coupler to provide the differential feeding. The rat-race coupler is designed by incorporating a stub in the middle of the $3\lambda/4$ line and quarter wave transformers at all the ports. A wideband of 27.96 % around 30 GHz is achieved with an amplitude imbalance of ± 0.5 dB

and return loss and isolation greater than 15 dB. The differential feeding antenna uses capacitive coupling to achieve wide bandwidth. The designed antenna bandwidth is from 25.6 to 34.13 GHz with $S_{11} \leq -10$ dB and a maximum gain of 12.39 dBi. It has a stable radiation pattern over a wide frequency band. Moreover, the 3 dBi gain bandwidth is from 26.1 to 34.1 GHz (26.58 %). The antenna, the rat-race coupler, and the coaxial transition are combined to build the transmitting part. A prototype is fabricated and measured. The resulted bandwidth is from 25.62 to 34.34 GHz with $S_{11} \leq -10$ dB with a maximum gain of 12.28 dBi and a 3 dB bandwidth from 25.62 to 33.77 GHz.

For the receiving part of the imaging system, a beamforming network is designed. The main components of the beamforming network include a 3-dB coupler, a crossover, and a 45° phase shifter. A wideband directional coupler with 7.35 GHz bandwidth is designed using PRGW technology (S_{11} and $S_{41} < -15$ dB and an output phase difference of 90.9 ± 1.62 degrees). This design has the widest bandwidth and the smallest phase difference among all the reported couplers in both metal RGW and PRGW. A wideband PRGW crossover from 26.8 to 33.9 GHz with return loss and isolation more than 14 dB and insertion loss less than 0.5 dB is designed. This design has the smallest size among the reported crossovers and it maintains wide bandwidth. A wideband phase shifter is designed with the same technology and has a bandwidth from 27 to 33.6 GHz ($S_{11} < -15$ dB and the output phase difference is 45 ± 2 degrees) depending on the coupled line coupler concept. All the components are combined to build a 4×4 Butler matrix. The simulated results show a bandwidth of 21.25% with return loss and isolation better than 10 dB and an output amplitude difference of ± 1.6 dB. A semi-log periodic antenna array is then designed as a radiating element. It has a matching bandwidth of 29.68 % ($S_{11} \leq -15$ dB) and its isolation level is more than 20 dB. All of these elements are combined to form the receiving part of the imaging system (the Butler matrix, the coaxial transition, and the antenna) then fabricated and measured. The resulting beam directions are at $\pm 13°$ and $\pm 36°$, at the center frequency (30 GHz). The return loss and the isolations are more than 10 dB over the frequency range from 26.1 to 33.5 GHz.

The proposed imaging system is implemented and the system set up has been illustrated. An image reconstruction algorithm is used to produce the final image where a resolution of 6 mm (0.6λ) has been obtained.

6.2 Future Work

Several possible future avenues could be explored to improve the active imaging system developed here.

1. For faster processing, a Wilkinson power divider and narrow band filters could be used to feed the transmitting antennas simultaneously each with a different frequency. A Wilkinson power divider could also be used in the receiving antenna to combine the signals from all the ports at the same time. These will allow all the measurements to be taken simultaneously. However, a Wilkinson power divider is not compatible with PRGW technology (the main technology in the proposed work), as it requires a lumped resistance element. Another solution for faster processing is to use multiple PNAs with standard power dividers to collect the data simultaneously.

2. A 2D Butler matrix could be implemented to further increase the spatial multiplexing and hence increase the quality of the produced image.

3. An imaging construction algorithm could be developed to produce 3D images by using multiple frequencies at each transmitter

4. More tests could be conducted to identify the sensitivity of the system for plastic and liquid objects.

5. Various types of textiles and leather could be used to cover the mannequin to make more realistic measurements.

Bibliography

[1] D. M. Sheen, D. L. McMakin, and T. E. Hall, "Three-dimensional millimeter-wave imaging for concealed weapon detection," *IEEE Transactions on Microwave Theory and Techniques*, vol. 49, no. 9, pp. 1581–1592, Sept 2001.

[2] X. Zhuge and A. G. Yarovoy, "A sparse aperture mimo-sar-based uwb imaging system for concealed weapon detection," *IEEE Transactions on Geoscience and Remote Sensing*, vol. 49, no. 1, pp. 509–518, 2011.

[3] J. Accardo and M. A. Chaudhry, "Radiation exposure and privacy concerns surrounding full-body scanners in airports," *Journal of Radiation Research and Applied Sciences*, vol. 7, no. 2, pp. 198 – 200, 2014. [Online]. Available: http://www.sciencedirect.com/science/article/pii/S1687850714000168

[4] "https://www.canada.ca/en/health-canada/services/health-risks-safety/radiation/everyday-things-emit-radiation/airport-full-body-scanners.html."

[5] "https://copublications.greenfacts.org/en/x-ray-full-body-scanners-for-airport-security/citizen-summary-securityscanners.pdf."

[6] "https://www.propublica.org/article/scanning-the-scanners-a-side-by-side-comparison."

[7] "https://www.propublica.org/article/tsa-removes-x-ray-body-scanners-from-major-airports."

[8] L. Yujiri, M. Shoucri, and P. Moffa, "Passive millimeter wave imaging," *IEEE Microwave Magazine*, vol. 4, no. 3, pp. 39–50, Sep. 2003.

[9] H. Zamani and M. Fakharzadeh, "1.5-d sparse array for millimeter-wave imaging based on compressive sensing techniques," *IEEE Transactions on Antennas and Propagation*, vol. 66, no. 4, pp. 2008–2015, April 2018.

[10] P. Chen and A. Babakhani, "3-d radar imaging based on a synthetic array of 30-ghz impulse radiators with on-chip antennas in 130-nm sige bicmos," *IEEE Transactions on Microwave Theory and Techniques*, vol. 65, no. 11, pp. 4373–4384, Nov 2017.

[11] J. Grzyb, K. Statnikov, N. Sarmah, and U. R. Pfeiffer, "3-d high-resolution imaging at 240 ghz with a single-chip fmcw monostatic radar in sige hbt technology," in *2016 41st International Conference on Infrared, Millimeter, and Terahertz waves (IRMMW-THz)*, Sep. 2016, pp. 1–2.

[12] A. A. Farsaee, Z. Kavehvash, and M. Shabany, "Efficient millimetre-wave imaging structure for detecting axially rotated objects," *IET Microwaves, Antennas Propagation*, vol. 12, no. 3, pp. 416–424, 2018.

[13] C. M. Watts, P. Lancaster, A. Pedross-Engel, J. R. Smith, and M. S. Reynolds, "2d and 3d millimeter-wave synthetic aperture radar imaging on a pr2 platform," in *2016 IEEE/RSJ International Conference on Intelligent Robots and Systems (IROS)*, Oct 2016, pp. 4304–4310.

[14] S. S. Ahmed, A. Genghammer, A. Schiessl, and L.-P. Schmidt, "Fully electronic active e-band personnel imager with 2 m^2 aperture," *2012 IEEE/MTT-S International Microwave Symposium Digest*, pp. 1–3, 2012.

[15] A. Pedross-Engel, D. Arnitz, J. N. Gollub, O. Yurduseven, K. P. Trofatter, M. F. Imani, T. Sleasman, M. Boyarsky, X. Fu, D. L. Marks, D. R. Smith, and M. S. Reynolds, "Orthogonal coded active illumination for millimeter wave, massive-mimo computational imaging with metasurface antennas," *IEEE Transactions on Computational Imaging*, vol. 4, no. 2, pp. 184–193, 2018.

[16] M. T. Ghasr, S. Kharkovsky, R. Bohnert, B. Hirst, and R. Zoughi, "30 ghz linear high-resolution and rapid millimeter wave imaging system for nde," *IEEE Transactions on Antennas and Propagation*, vol. 61, no. 9, pp. 4733–4740, 2013.

[17] Z. Briqech, S. Gupta, A. Beltayib, A. Elboushi, A. R. Sebak, and T. A. Denidni, "57-64 ghz imaging/detection sensor–part i: System setup and experimental evaluations," *IEEE Sensors Journal*, vol. 20, no. 18, pp. 10 824–10 832, 2020.

[18] C. Zech, A. Hülsmann, I. Kallfass, A. Tessmann, M. Zink, M. Schlechtweg, A. Leuther, and O. Ambacher, "Active millimeter-wave imaging system for material analysis and object detection," in *Millimetre Wave and Terahertz Sensors and Technology IV*, K. A. Krapels, N. A. Salmon, and E. Jacobs, Eds., vol. 8188, International Society for Optics and Photonics. SPIE, 2011, pp. 87 – 95. [Online]. Available: https://doi.org/10.1117/12.898796

[19] S. Dill, M. Peichl, and H. Süß, "Study of passive MMW personnel imaging with respect to suspicious and common concealed objects for security applications," in *Millimetre Wave and Terahertz Sensors and Technology*, K. A. Krapels and N. A. Salmon, Eds., vol. 7117, International Society for Optics and Photonics. SPIE, 2008, pp. 72 – 79. [Online]. Available: https://doi.org/10.1117/12.800096

[20] C. Guangbin, Z. Chonghui, W. Haihan, X. Wei, and L. Zhaoyang, "Millimeter wave passive imaging system using reflector antenna," in *IET International Radar Conference 2015*, Oct 2015, pp. 1–5.

[21] J.-Y. Son, S. Yeom, J.-H. Chun, V. P. Guschin, and D.-S. Lee, "Characteristics of stereo images from detectors in focal plane array," *J. Opt. Soc. Am. A*, vol. 28, no. 7, pp. 1482–1488, Jul 2011. [Online]. Available: http://josaa.osa.org/abstract.cfm?URI=josaa-28-7-1482

[22] J. A. Lovberg, C. Martin, and V. Kolinko, "Video-rate passive millimeter-wave imaging using phased arrays," in *2007 IEEE/MTT-S International Microwave Symposium*, June 2007, pp. 1689–1692.

[23] S. S. Ahmed, A. Schiessl, F. Gumbmann, M. Tiebout, S. Methfessel, and L. Schmidt, "Advanced microwave imaging," *IEEE Microwave Magazine*, vol. 13, no. 6, pp. 26–43, Sep. 2012.

[24] W. TAN, P. Huang, Z. Huang, Y. Qi, and W. Wang, "Three-dimensional microwave imaging for concealed weapon detection using range stacking technique," *International Journal of Antennas and Propagation*, vol. 2017, pp. 1–11, 08 2017.

[25] M. Jones, D. Sheen, and J. Tedeschi, "Wideband archimedean spiral antenna for millimeter-wave imaging array," in *2017 IEEE International Symposium on Antennas and Propagation USNC/URSI National Radio Science Meeting*, 2017, pp. 845–846.

[26] F. Gumbmann, P. Tran, and L. Schmidt, "Sparse linear array design for a short range imaging radar," in *2009 European Radar Conference (EuRAD)*, Sep. 2009, pp. 176–179.

[27] M. Kazemi, Z. Kavehvash, and M. Shabany, "K-space aware multi-static millimeter-wave imaging," *IEEE Transactions on Image Processing*, vol. 28, no. 7, pp. 3613–3623, July 2019.

[28] J. Gao, Y. Qin, B. Deng, H. Wang, and X. Li, "Novel efficient 3d short-range imaging algorithms for a scanning 1d-mimo array," *IEEE Transactions on Image Processing*, vol. 27, no. 7, pp. 3631–3643, July 2018.

[29] E. Abbe, "Beitrage zur theorie des mikroskops und der mikroskopischen wahrnehmung," *Archiv für Mikroskopische Anatomie*, vol. 9, no. 1, pp. 413–418, dec 1873. [Online]. Available: https://doi.org/10.1007%2Fbf02956173

[30] "Martin ryle – facts. nobelprize.org. nobel media ab 2020. sun. 31 may 2020." https://www.nobelprize.org/prizes/physics/1974/ryle/facts/.

[31] "*https* : *//en.wikipedia.org/wiki/aperture_synthesis*."

[32] W. Stutzman and G. Thiele, *Antenna Theory and Design*, ser. Antenna Theory and Design. Wiley, 2012. [Online]. Available: https://books.google.ca/books?id=xhZRA1K57wIC

[33] A. U. Zaman, E. Rajo-Iglesias, E. Alfonso, and P. Kildal, "Design of transition from coaxial line to ridge gap waveguide," in *2009 IEEE Antennas and Propagation Society International Symposium*, June 2009, pp. 1–4.

[34] P. Kildal, "Three metamaterial-based gap waveguides between parallel metal plates for mm/submm waves," in *2009 3rd European Conference on Antennas and Propagation*, March 2009, pp. 28–32.

[35] P. Kildal, A. U. Zaman, E. Rajo-Iglesias, E. Alfonso, and A. Valero-Nogueira, "Design and experimental verification of ridge gap waveguide in bed of nails for parallel-plate mode suppression," *IET Microwaves, Antennas Propagation*, vol. 5, no. 3, pp. 262–270, Feb 2011.

[36] P. Kildal, "Definition of artificially soft and hard surfaces for electromagnetic waves," *Electronics Letters*, vol. 24, no. 3, pp. 168–170, Feb 1988.

[37] P. Kildal, "The hat feed: A dual-mode rear-radiating waveguide antenna having low cross polarization," *IEEE Transactions on Antennas and Propagation*, vol. 35, no. 9, pp. 1010–1016, Sep. 1987.

[38] A. Polemi, S. Maci, and P. Kildal, "Dispersion characteristics of a metamaterial-based parallel-plate ridge gap waveguide realized by bed of nails," *IEEE Transactions on Antennas and Propagation*, vol. 59, no. 3, pp. 904–913, March 2011.

[39] M. G. Silveirinha, C. A. Fernandes, and J. R. Costa, "Electromagnetic characterization of textured surfaces formed by metallic pins," *IEEE Transactions on Antennas and Propagation*, vol. 56, no. 2, pp. 405–415, Feb 2008.

[40] M. Vukomanovic, M. Bosiljevac, and Z. Sipus, "Analysis of arbitrary gap-waveguide structures based on efficient use of a mode-matching technique," *IEEE Antennas and Wireless Propagation Letters*, vol. 15, pp. 1844–1847, 2016.

[41] M. Sharifi Sorkherizi and A. A. Kishk, "Transition from microstrip to printed ridge gap waveguide for millimeter-wave application," in *2015 IEEE International Symposium on Antennas and Propagation USNC/URSI National Radio Science Meeting*, July 2015, pp. 1588–1589.

[42] B. Molaei and A. Khaleghi, "A novel wideband microstrip line to ridge gap waveguide transition using defected ground slot," *IEEE Microwave and Wireless Components Letters*, vol. 25, no. 2, pp. 91–93, Feb 2015.

[43] M. Sharifi Sorkherizi and A. A. Kishk, "Fully printed gap waveguide with facilitated design properties," *IEEE Microwave and Wireless Components Letters*, vol. 26, no. 9, pp. 657–659, Sep. 2016.

[44] U. Nandi, A. U. Zaman, A. Vosoogh, and J. Yang, "Millimeter wave contactless microstrip-gap waveguide transition suitable for integration of rf mmic with gap waveguide array antenna," in *2017 11th European Conference on Antennas and Propagation (EUCAP)*, March 2017, pp. 1682–1684.

[45] N. Bayat-Makou and A. A. Kishk, "Realistic air-filled tem printed parallel-plate waveguide based on ridge gap waveguide," *IEEE Transactions on Microwave Theory and Techniques*, vol. 66, no. 5, pp. 2128–2140, May 2018.

[46] F. Fan, J. Yang, V. Vassilev, and A. U. Zaman, "Bandwidth investigation on half-height pin in ridge gap waveguide," *IEEE Transactions on Microwave Theory and Techniques*, vol. 66, no. 1, pp. 100–108, Jan 2018.

[47] S. I. Shams and A. A. Kishk, "Wideband coaxial to ridge gap waveguide transition," *IEEE Transactions on Microwave Theory and Techniques*, vol. 64, no. 12, pp. 4117–4125, Dec 2016.

[48] M. A. Nasr and A. A. Kishk, "Wideband inline coaxial to ridge waveguide transition with tuning capability for ridge gap waveguide," *IEEE Transactions on Microwave Theory and Techniques*, vol. 66, no. 6, pp. 2757–2766, June 2018.

[49] S. Birgermajer, N. Janković, V. Crnojević-Bengin, M. Bozzi, and V. Radonić, "Forward-wave 0 db directional coupler based on microstrip-ridge gap waveguide technology," in *2017 13th International Conference on Advanced Technologies, Systems and Services in Telecommunications (TELSIKS)*, Oct 2017, pp. 154–157.

[50] S. Birgermajer, N. Janković, V. Radonić, V. Crnojević-Bengin, and M. Bozzi, "Microstrip-ridge gap waveguide filter based on cavity resonators with mushroom inclusions," *IEEE Transactions on Microwave Theory and Techniques*, vol. 66, no. 1, pp. 136–146, Jan 2018.

[51] F. Ahmadfard and S. A. Razavi, "Bandwidth and gain enhancement of ridge gap waveguide h-plane horn antennas using outer transitions," *IEEE Transactions on Antennas and Propagation*, vol. 66, no. 8, pp. 4315–4319, Aug 2018.

[52] D. Zarifi, A. Farahbakhsh, A. U. Zaman, and P. Kildal, "Design and fabrication of a high-gain 60-ghz corrugated slot antenna array with ridge gap waveguide distribution layer," *IEEE Transactions on Antennas and Propagation*, vol. 64, no. 7, pp. 2905–2913, July 2016.

[53] Z. Talepour and A. Khaleghi, "A k-band planar slot array antenna on a single layer ridge gap waveguide," in *2017 11th European Conference on Antennas and Propagation (EUCAP)*, March 2017, pp. 1685–1689.

[54] H. Raza, J. Yang, P. Kildal, and E. Alfonso Alós, "Microstrip-ridge gap waveguide–study of losses, bends, and transition to wr-15," *IEEE Transactions on Microwave Theory and Techniques*, vol. 62, no. 9, pp. 1943–1952, Sep. 2014.

[55] S. Liao, P. Wu, K. M. Shum, and Q. Xue, "Differentially fed planar aperture antenna with high gain and wide bandwidth for millimeter-wave application," *IEEE Transactions on Antennas and Propagation*, vol. 63, no. 3, pp. 966–977, 2015.

[56] N. Bayat-Makou and A. A. Kishk, "Millimeter-wave substrate integrated dual level gap waveguide horn antenna," *IEEE Transactions on Antennas and Propagation*, vol. 65, no. 12, pp. 6847–6855, 2017.

[57] M. M. M. Ali and A. Sebak, "Printed rgw circularly polarized differential feeding antenna array for 5g communications," *IEEE Transactions on Antennas and Propagation*, vol. 67, no. 5, pp. 3151–3160, 2019.

[58] S. A. Razavi, P. Kildal, L. Xiang, E. Alfonso Alós, and H. Chen, "2$\times$ 2-slot element for 60-ghz planar array antenna realized on two doubled-sided pcbs using siw cavity and ebg-type soft surface fed by microstrip-ridge gap waveguide," *IEEE Transactions on Antennas and Propagation*, vol. 62, no. 9, pp. 4564–4573, 2014.

[59] S. March, "A wideband stripline hybrid ring (correspondence)," *IEEE Transactions on Microwave Theory and Techniques*, vol. 16, no. 6, pp. 361–361, June 1968.

[60] M. . Murgulescu, P. Legaud, E. Moisan, E. Penard, M. Goloubkoff, and I. Zaquine, "New small size, wideband 180° ring couplers: Theory and experiment," in *1994 24th European Microwave Conference*, vol. 1, Sep. 1994, pp. 670–674.

[61] Chih-Wai Kao and Chun Hsiung Chen, "Novel uniplanar 180° hybrid-ring couplers with spiral-type phase inverters," *IEEE Microwave and Guided Wave Letters*, vol. 10, no. 10, pp. 412–414, Oct 2000.

[62] C.-Y. Chang and C.-C. Yang, "A novel broad-band chebyshev-response rat-race ring coupler," *IEEE Transactions on Microwave Theory and Techniques*, vol. 47, no. 4, pp. 455–462, April 1999.

[63] C.-W. Kao and C. H. Chen, "Miniaturized uniplanar 180° hybrid-ring couplers with 0.8 λ_g and 0.67 λ_g circumference," *2000 Asia-Pacific Microwave Conference*, pp. 217–220, 2000.

[64] Chun-Hsiang Chi and Chi-Yang Chang, "A compact wideband 180° hybrid ring coupler using a novel interdigital cps inverter," in *2007 European Microwave Conference*, Oct 2007, pp. 548–551.

[65] J. Sorocki, I. Piekarz, K. Wincza, and S. Gruszczynski, "Bandwidth improvement of rat-race couplers having left-handed transmission-line sections," *Int. J. RF Microw. Comput.-Aided Eng.*, vol. 24, no. 3, pp. 341–347, May 2014. [Online]. Available: http://dx.doi.org/10.1002/mmce.20766

[66] D. Kholodnyak, P. Kapitanova, S. Humbla, R. Perrone, J. Mueller, M. A. Hein, and I. Vendik, "180° power dividers using metamaterial transmission lines," in *2008 14th Conference on Microwave Techniques*, April 2008, pp. 1–4.

[67] K. Staszek, J. Kołodziej, K. Wilcza, and S. Gruszczyński, "Compact broadband rat-race coupler in multilayer technology designed with the use of artificial right- and left-handed transmission line," *Journal of Telecommunications and Information Technology*, vol. nr 2, pp. 107–112, 2012.

[68] J. Hou and Y. Wang, "Design of compact 90°and 180° couplers with harmonic suppression using lumped-element bandstop resonators," *IEEE Transactions on Microwave Theory and Techniques*, vol. 58, no. 11, pp. 2932–2939, Nov 2010.

[69] G. Brzezina and L. Roy, "Miniaturized 180° hybrid coupler in ltcc for l-band applications," *IEEE Microwave and Wireless Components Letters*, vol. 24, no. 5, pp. 336–338, May 2014.

[70] G. Slade, "Reduced-size octave-bandwidth microstrip/lumped-element rat-race coupler," 2008.

[71] I. Haroun, Y. Hsu, D. Chang, and C. Plett, "A novel reduced-size 60-ghz 180° coupler using lg-cpw transmission lines," in *Asia-Pacific Microwave Conference 2011*, Dec 2011, pp. 1750–1753.

[72] S. Koziel and P. Kurgan, "On elementary cell selection for miniaturized microstrip rat-race coupler design," in *2017 International Conference on Electromagnetics in Advanced Applications (ICEAA)*, Sep. 2017, pp. 836–839.

[73] K. V. P. Kumar, R. K. Barik, I. S. Krishna, and S. S. Karthikeyan, "Design of compact 180° hybrid coupler for unequal power division ratio using slow wave structures," in *2017 Twenty-third National Conference on Communications (NCC)*, March 2017, pp. 1–5.

[74] Kian Sen Ang, Yoke Choy Leong, and Chee How Lee, "A new class of multisection 180° hybrids based on cascadable hybrid-ring couplers," *IEEE Transactions on Microwave Theory and Techniques*, vol. 50, no. 9, pp. 2147–2152, Sep. 2002.

[75] W. Che, K. Deng, E. K. N. Yung, and K. Wu, "H-plane 3-db hybrid ring of high isolation in substrate-integrated rectangular waveguide (sirw)," *Microwave and Optical Technology Letters*, vol. 48, no. 3, pp. 502–505, 2006. [Online]. Available: https://onlinelibrary.wiley.com/doi/abs/10.1002/mop.21392

[76] R. Dehdasht-Heydari, K. Forooraghi, and M. Naser-Moghadasi, "Efficient and accurate analysis of a substrate integrated waveguide (siw) rat-race coupler excited by four u-shape slot-coupled transitions." *Applied Computational Electromagnetics Society Journal*, vol. 30, no. 1, pp. 42 – 49, 2015. [Online]. Available: https://lib-ezproxy.concordia.ca/login?url=http://search.ebscohost.com/login.aspx?direct=true&db=a9h&AN=101606532&site=eds-live

[77] X. Zou, C. Tong, C. Li, and W. Pang, "Wideband hybrid ring coupler based on half-mode substrate integrated waveguide," *IEEE Microwave and Wireless Components Letters*, vol. 24, no. 9, pp. 596–598, Sep. 2014.

[78] Yan Ding and K. Wu, "Miniaturized hybrid ring circuits using t-type folded substrate integrated waveguide (tfsiw)," in *2009 IEEE MTT-S International Microwave Symposium Digest*, June 2009, pp. 705–708.

[79] A. A. M. Ali, H. B. El-Shaarawy, and H. Aubert, "Miniaturized hybrid ring coupler using electromagnetic bandgap loaded ridge substrate integrated waveguide," *IEEE Microwave and Wireless Components Letters*, vol. 21, no. 9, pp. 471–473, Sep. 2011.

[80] J. Yang and H. Raza, "Empirical formulas for designing gap-waveguide hybrid ring coupler," *Microwave and Optical Technology Letters*, vol. 55, no. 8, pp. 1917–1920, 2013. [Online]. Available: https://onlinelibrary.wiley.com/doi/abs/10.1002/mop.27714

[81] S. Mosca, F. Bilotti, A. Toscano, and L. Vegni, "A novel design method for blass matrix beam-forming networks," *IEEE Transactions on Antennas and Propagation*, vol. 50, no. 2, pp. 225–232, Feb 2002.

[82] J. Ruze, "Wide-angle metal-plate optics," *Proceedings of the IRE*, vol. 38, no. 1, pp. 53–59, Jan 1950.

[83] W. Rotman and R. Turner, "Wide-angle microwave lens for line source applications," *IEEE Transactions on Antennas and Propagation*, vol. 11, no. 6, pp. 623–632, November 1963.

[84] M. Maddahali, Z. H. Firouzeh, and A. Hosseini Kishani, "Design of rotman lens antenna at ku-band based on substrate integrated technology," *Journal of Communication Engineering*, vol. 3, no. 1, pp. 33–44, 2016. [Online]. Available: http://jce.shahed.ac.ir/article_313.html

[85] J. Blass, "Multidirectional antenna - a new approach to stacked beams," in *1958 IRE International Convention Record*, vol. 8, March 1960, pp. 48–50.

[86] F. Casini, R. V. Gatti, L. Marcaccioli, and R. Sorrentino, "A novel design method for blass matrix beam-forming networks," in *2007 European Radar Conference*, Oct 2007, pp. 232–235.

[87] J. Butler, "Beam-forming matrix simplifies design of electronically scanned antennas," *Electron. Des.*, vol. 9, no. 8, pp. 170–173, 1961.

[88] P. I. Balanis, Constantine A.; Ioannides, *Introduction to Smart Antennas*. Morgan & Claypool, 2007.

[89] G. Boumediene, M. S. Mouhamed, F. Bendimerad, H. Salem, and A. Bekr, "Study of a planar topology butler matrix for printed multibeam antenna," *IJCSI International Journal of Computer Science Issues*, vol. 9, no. 3, pp. 184–193, November 2012.

[90] H. Moody, "The systematic design of the butler matrix," *IEEE Transactions on Antennas and Propagation*, vol. 12, no. 6, pp. 786–788, November 1964.

[91] W. M. Dyab, A. A. Sakr, and K. Wu, "Dually-polarized butler matrix for base stations with polarization diversity," *IEEE Transactions on Microwave Theory and Techniques*, vol. 66, no. 12, pp. 5543–5553, Dec 2018.

[92] I. M. Mohamed and A. Sebak, "60 ghz 2-d scanning multibeam cavity-backed patch array fed by compact siw beamforming network for 5g applications," *IEEE Transactions on Antennas and Propagation*, vol. 67, no. 4, pp. 2320–2331, April 2019.

[93] M. M. M. Ali and A. Sebak, "2-d scanning magnetoelectric dipole antenna array fed by rgw butler matrix," *IEEE Transactions on Antennas and Propagation*, vol. 66, no. 11, pp. 6313–6321, Nov 2018.

[94] K. Ding and A. A. Kishk, "2-d butler matrix and phase-shifter group," *IEEE Transactions on Microwave Theory and Techniques*, vol. 66, no. 12, pp. 5554–5562, Dec 2018.

[95] C. Chen and T. Chu, "Design of a 60-ghz substrate integrated waveguide butler matrix—a systematic approach," *IEEE Transactions on Microwave Theory and Techniques*, vol. 58, no. 7, pp. 1724–1733, July 2010.

[96] C. Lee, M. K. Khattak, and S. Kahng, "Wideband 5g beamforming printed array clutched by lte-a 4×4-multiple-input–multiple-output antennas with high isolation," *IET Microwaves, Antennas Propagation*, vol. 12, no. 8, pp. 1407–1413, 2018.

[97] J. Lian, Y. Ban, Q. Yang, B. Fu, Z. Yu, and L. Sun, "Planar millimeter-wave 2-d beam-scanning multibeam array antenna fed by compact siw beam-forming network,"

IEEE Transactions on Antennas and Propagation, vol. 66, no. 3, pp. 1299–1310, March 2018.

[98] F. Huang, W. Chen, and M. Rao, "Switched-beam antenna array based on butler matrix for 5g wireless communication," in *2016 IEEE International Workshop on Electromagnetics: Applications and Student Innovation Competition (iWEM)*, May 2016, pp. 1–3.

[99] C. Tseng, C. Chen, and T. Chu, "A low-cost 60-ghz switched-beam patch antenna array with butler matrix network," *IEEE Antennas and Wireless Propagation Letters*, vol. 7, pp. 432–435, 2008.

[100] Y. Wang, K. Ma, and Z. Jian, "A low-loss butler matrix using patch element and honeycomb concept on sisl platform," *IEEE Transactions on Microwave Theory and Techniques*, vol. 66, no. 8, pp. 3622–3631, Aug 2018.

[101] M. Kishihara, A. Yamaguchi, Y. Utsumi, and I. Ohta, "Fabrication of waveguide butler matrix for short millimeter-wave using x-ray lithography," in *2017 IEEE MTT-S International Microwave Symposium (IMS)*, June 2017, pp. 568–571.

[102] A. Algaba-Brazalez and E. Rajo-Iglesias, "Design of a butler matrix at 60ghz in inverted microstrip gap waveguide technology," in *2015 IEEE International Symposium on Antennas and Propagation USNC/URSI National Radio Science Meeting*, July 2015, pp. 2125–2126.

[103] S. Gruszczynski, K. Wincza, and K. Sachse, "Broadband 4×4 butler matrices utilizing tapered-coupled-line directional couplers," in *2011 MICROWAVES, RADAR AND REMOTE SENSING SYMPOSIUM*, Aug 2011, pp. 77–81.

[104] C. Tseng, J. Huang, and C. Tseng, "Design of planar 8-by-16 butler matrix for 16-element switch-beam antenna array," in *2018 Asia-Pacific Microwave Conference (APMC)*, Nov 2018, pp. 1534–1536.

[105] T. H. Jang, H. Y. Kim, and C. S. Park, "A 60 ghz wideband switched-beam dipole-array-fed hybrid horn antenna," *IEEE Antennas and Wireless Propagation Letters*, vol. 17, no. 7, pp. 1344–1348, July 2018.

[106] S. Trinh-Van, J. M. Lee, Y. Yang, K. Lee, and K. C. Hwang, "A sidelobe-reduced, four-beam array antenna fed by a modified 4×4 butler matrix for 5g applications," *IEEE Transactions on Antennas and Propagation*, vol. 67, no. 7, pp. 4528–4536, 2019.

[107] K. Wincza, A. Rydosz, I. Slomian, and S. Gruszczynski, "Reduced sidelobe multi-beam antenna array with broadside beam fed by 4×8 butler matrix," *2015 International Symposium on Antennas and Propagation (ISAP)*, pp. 1–3, 2015.

[108] H. N. Chu and T. Ma, "An extended 4×4 butler matrix with enhanced beam controllability and widened spatial coverage," *IEEE Transactions on Microwave Theory and Techniques*, vol. 66, no. 3, pp. 1301–1311, March 2018.

[109] D. Pozar, *Microwave Engineering, Fourth Edition Wiley E-Text Reg Card*. John Wiley & Sons, Incorporated, 2013. [Online]. Available: https://books.google.ca/books?id=N9W-kQEACAAJ

[110] Z. Qamar, S. Zheng, W. Chan, and D. Ho, "Coupling coefficient range extension technique for broadband branch-line coupler," *Journal of Electromagnetic Waves and Applications*, vol. 32, no. 1, pp. 92–112, 2018. [Online]. Available: https://doi.org/10.1080/09205071.2017.1369906

[111] S. Jung, R. Negra, and F. M. Ghannouchi, "A miniaturized double-stage 3db broadband branch-line hybrid coupler using distributed capacitors," in *2009 Asia Pacific Microwave Conference*, Dec 2009, pp. 1323–1326.

[112] S. Lee and Y. Lee, "Wideband branch-line couplers with single-section quarter-wave transformers for arbitrary coupling levels," *IEEE Microwave and Wireless Components Letters*, vol. 22, no. 1, pp. 19–21, Jan 2012.

[113] W. A. Arriola, J. Y. Lee, and I. S. Kim, "Wideband 3 db branch line coupler based on $\lambda/4$ open circuited coupled lines," *IEEE Microwave and Wireless Components Letters*, vol. 21, no. 9, pp. 486–488, 2011.

[114] M. A. Ashra, A. R. Sebak, Z. O. Al-Hekail, and M. A. Alkanhal, "B4. analysis and design of single section and three-section ultra-wideband quadrature hybrid couplers," in *2012 29th National Radio Science Conference (NRSC)*, April 2012, pp. 37–44.

[115] M. Farahani, T. A. Denidni, and M. Nedi, "Design of a low output-phase error ridge-gap coupler for antenna arrays applications," in *2018 IEEE International Symposium on Antennas and Propagation USNC/URSI National Radio Science Meeting*, July 2018, pp. 1099–1100.

[116] M. Farahani, M. Akbari, M. Nedil, T. A. Denidni, and A. R. Sebak, "A novel low-loss millimeter-wave 3-db 90° ridge-gap coupler using large aperture progressive phase compensation," *IEEE Access*, vol. 5, pp. 9610–9618, 2017.

[117] A. T. Hassan and A. A. Kishk, "Microstrip ridge gap waveguide hybrid coupler at 60 ghz," in *2018 IEEE International Symposium on Antennas and Propagation USNC/URSI National Radio Science Meeting*, July 2018, pp. 427–428.

[118] S. I. Shams and A. A. Kishk, "Design of 3-db hybrid coupler based on rgw technology," *IEEE Transactions on Microwave Theory and Techniques*, vol. 65, no. 10, pp. 3849–3855, 2017.

[119] M. M. M. Ali, S. I. Shams, and A. Sebak, "Printed ridge gap waveguide 3-db coupler: Analysis and design procedure," *IEEE Access*, vol. 6, pp. 8501–8509, 2018.

[120] Y. Wang, A. M. Abbosh, and B. Henin, "Broadband microwave crossover using combination of ring resonator and circular microstrip patch," *IEEE Transactions on Components, Packaging and Manufacturing Technology*, vol. 3, no. 10, pp. 1771–1777, Oct 2013.

[121] S. Y. Zheng and X. F. Ye, "Ultra-compact wideband millimeter-wave crossover using slotted siw structure," in *2016 IEEE International Workshop on Electromagnetics: Applications and Student Innovation Competition (iWEM)*, May 2016, pp. 1–2.

[122] A. B. Guntupalli, T. Djerafi, and K. Wu, "Ultra-compact millimeter-wave substrate integrated waveguide crossover structure utilizing simultaneous electric and magnetic coupling," in *2012 IEEE/MTT-S International Microwave Symposium Digest*, June 2012, pp. 1–3.

[123] K. Murai, H. Ikeuchi, T. Kawai, M. Kishihara, and I. Ohta, "Broadband design method of siw directional couplers," in *2011 China-Japan Joint Microwave Conference*, April 2011, pp. 1–4.

[124] M. M. M. Ali and A. Sebak, "Compact printed ridge gap waveguide crossover for future 5g wireless communication system," *IEEE Microwave and Wireless Components Letters*, vol. 28, no. 7, pp. 549–551, July 2018.

[125] N. J. G. Fonseca, "Printed s-band 4×4 nolen matrix for multiple beam antenna applications," *IEEE Transactions on Antennas and Propagation*, vol. 57, no. 6, pp. 1673–1678, June 2009.

[126] B. Yang, Z. Yu, R. Zhang, J. Zhou, and W. Hong, "Local oscillator phase shifting and harmonic mixing-based high-precision phased array for 5g millimeter-wave communications," *IEEE Transactions on Microwave Theory and Techniques*, vol. 67, no. 7, pp. 3162–3173, 2019.

[127] Y. Yin, F. Wu, Y. Chen, J. Zhou, and J. Zhai, "Design of a cascaded full 360° reflection-type phase shifter with 90° hybrid coupler," in *2018 IEEE MTT-S International Wireless Symposium (IWS)*, May 2018, pp. 1–3.

[128] N. Somjit, G. Stemme, and J. Oberhammer, "Deep-reactive-ion-etched wafer-scale-transferred all-silicon dielectric-block millimeter-wave mems phase shifters," *Journal of Microelectromechanical Systems*, vol. 19, no. 1, pp. 120–128, Feb 2010.

[129] Z. Briqech, A. Sebak, and T. A. Denidni, "Low-cost wideband mm-wave phased array using the piezoelectric transducer for 5g applications," *IEEE Transactions on Antennas and Propagation*, vol. 65, no. 12, pp. 6403–6412, Dec 2017.

[130] T.-Y. Yun and K. Chang, "A low-loss time-delay phase shifter controlled by piezoelectric transducer to perturb microstrip line," *IEEE Microwave and Guided Wave Letters*, vol. 10, no. 3, pp. 96–98, March 2000.

[131] K. Sellal, L. Talbi, T. Denidni, and J. Lebel, "A new substrate integrated waveguide phase shifter," in *2006 European Microwave Conference*, Sep. 2006, pp. 72–75.

[132] B. Khorasani and F. Geran, "New wideband fixed phase shifter with air holes integrated in substrate," in *2014 Third Conference on Millimeter-Wave and Terahertz Technologies (MMWATT)*, Dec 2014, pp. 1–4.

[133] M. A. Abdelaal, S. I. Shams, and A. A. Kishk, "Compact rgw differential phase shifter for millimeter-wave applications," in *2018 18th International Symposium on Antenna Technology and Applied Electromagnetics (ANTEM)*, Aug 2018, pp. 1–2.

[134] Y. Kou, X. Wang, C. Liu, and H. Gao, "Design of a uwb planar quasi yagi-uda antenna on s-c band," in *IET International Radar Conference 2015*, 2015, pp. 1–4.

[135] H. Kumar and G. Kumar, "Compact planar log-periodic dipole array based yagi-uda antenna," in *2017 IEEE International Symposium on Antennas and Propagation USNC/URSI National Radio Science Meeting*, 2017, pp. 2157–2158.

[136] H. Kumar and G. Kumar, "Compact planar yagi-uda antenna with improved characteristics," in *2017 11th European Conference on Antennas and Propagation (EUCAP)*, 2017, pp. 2008–2012.

[137] A. Elboushi, D. Joanes, M. Derbas, S. Khaled, A. Zafar, S. Attabibi, and A. R. Sebak, "Design of uwb antenna array for through-wall detection system," in *2013 IEEE Symposium on Wireless Technology Applications (ISWTA)*, 2013, pp. 349–354.

[138] R. A. Alhalabi and G. M. Rebeiz, "High-gain yagi-uda antennas for millimeter-wave switched-beam systems," *IEEE Transactions on Antennas and Propagation*, vol. 57, no. 11, pp. 3672–3676, 2009.

[139] O. M. Haraz, S. A. Alshebeili, and A. Sebak, "Low-cost high gain printed log-periodic dipole array antenna with dielectric lenses for v-band applications," *IET Microwaves, Antennas Propagation*, vol. 9, no. 6, pp. 541–552, 2015.

[140] C. Yu, W. Hong, L. Chiu, G. Zhai, C. Yu, W. Qin, and Z. Kuai, "Ultrawideband printed log-periodic dipole antenna with multiple notched bands," *IEEE Transactions on Antennas and Propagation*, vol. 59, no. 3, pp. 725–732, 2011.

[141] G. H. Zhai, W. Hong, K. Wu, and Z. Q. Kuai, "Wideband substrate integrated printed log-periodic dipole array antenna," *IET Microwaves, Antennas Propagation*, vol. 4, no. 7, pp. 899–905, 2010.

[142] N. Ashraf, A. Sebak, and A. A. Kishk, "End-launch horn antenna array for ka-band 5g applications," in *2018 18th International Symposium on Antenna Technology and Applied Electromagnetics (ANTEM)*, 2018, pp. 1–2.

[143] B. M. Schiffman, "A new class of broad-band microwave 90-degree phase shifters," *IRE Transactions on Microwave Theory and Techniques*, vol. 6, no. 2, pp. 232–237, April 1958.

[144] N. H. Farhat and W. R. Guard, "Millimeter wave holographic imaging of concealed weapons," *Proceedings of the IEEE*, vol. 59, no. 9, pp. 1383–1384, 1971.

[145] T. E. H. H. D. Collins, D. L. McMakin and R. P. Gribble, "Real-time holographic surveillance system," *U.S. Patent 5 455 590*, Oct. 3, 1995.

[146] M. Kawulok, P. Benecki, S. Piechaczek, K. Hrynczenko, D. Kostrzewa, and J. Nalepa, "Deep learning for multiple-image super-resolution," *IEEE Geoscience and Remote Sensing Letters*, vol. 17, no. 6, pp. 1062–1066, 2020.

List of Publications

Thesis Related Publications

Journal Papers

J1 I. Afifi, M. M. M. Ali and A. Sebak, "Analysis and Design of a Wideband Coaxial Transition to Metal and Printed Ridge Gap Waveguide," in IEEE Access, vol. 6, pp. 70698-70706, 2018, doi: 10.1109/ACCESS.2018.2881732.

J2 I. Afifi and A. R. Sebak, "Wideband Printed Ridge Gap Rat-Race Coupler for Differential Feeding Antenna," in IEEE Access, vol. 8, pp. 78228-78235, 2020, doi: 10.1109/ACCESS.2020.2990169.

J3 I. Afifi and A. Sebak, "Wideband 4×4 Butler Matrix in The Printed Ridge Gap Waveguide Technology for Millimeter Wave Applications," in IEEE Transactions on Antennas and Propagation, doi: 10.1109/TAP.2020.2981716.

Conference Papers

C1 I. Afifi, M. M. M. Ali and A. Sebak, "Wideband Printed Ridge Gap Semi-Log Periodic Structure Antenna for Millimeter Wave Applications," 2018 18th International Symposium on Antenna Technology and Applied Electromagnetics (ANTEM), Waterloo, ON, 2018, pp. 1-2, doi: 10.1109/ANTEM.2018.8572877.

C2 I. Afifi, M. Alzidani and A. Sebak, "Wideband printed ridge gap waveguide differential feeding aperture antenna for millimeter wave applications," 2019 IEEE International Symposium on Antennas and Propagation and USNC-URSI Radio Science

Meeting, Atlanta, GA, USA, 2019, pp. 267-268, doi: 10.1109 /APUSNCURSINRSM. 2019. 8888584.

Other Publications

Here is a list of other jointly published papers during my PhD program that are not included in this thesis.

Journal Papers

J4 M. Asaadi, I. Afifi and A. Sebak, "High Gain and Wideband High Dense Dielectric Patch Antenna Using FSS Superstrate for Millimeter-Wave Applications," in IEEE Access, vol. 6, pp. 38243-38250, 2018, doi: 10.1109/ACCESS.2018.2854225.

J5 A. Beltayib, I. Afifi and A. Sebak, "4 $\times$ 4 -Element Cavity Slot Antenna Differentially-Fed by Odd Mode Ridge Gap Waveguide," in IEEE Access, vol. 7, pp. 48185-48195, 2019, doi: 10.1109/ACCESS.2019.2910254.

J6 E. H. Mujammami, I. Afifi and A. B. Sebak, "Optimum Wideband High Gain Analog Beamforming Network for 5G Applications," in IEEE Access, vol. 7, pp. 52226-52237, 2019, doi: 10.1109/ACCESS.2019.2912119.

J7 M. M. M. Ali, I. Afifi and A. Sebak, "A Dual Polarized Magneto-Electric Dipole Antenna Based on Printed Ridge Gap Waveguide Technology," in IEEE Transactions on Antennas and Propagation, doi: 10.1109/TAP.2020.2980357.

J8 M. Alzidani, I. Afifi, M. Asaadi and A. Sebak, "Ultra-Wideband Differential Fed Hybrid Antenna With High-Cross Polarization Discrimination for Millimeter Wave Applications," in IEEE Access, vol. 8, pp. 80673-80683, 2020, doi: 10.1109/ACCESS.2020.2988000.

Conference Papers

C3 I. Afifi, M. M. M. Ali and A. R. Sebak, "Analysis and design of a 30 GHz printed ridge gap Ring-crossover," 2019 USNC-URSI Radio Science Meeting (Joint with AP-S Symposium), Atlanta, GA, USA, 2019, pp. 65-66, doi: 10.1109/USNC-URSI.2019.8861872.

C4 M. M. M. Ali, I. Afifi and A. R. Sebak, "Design of Printed RGW Crossover for Millimeter Wave Beam Switching Network," 2019 USNC-URSI Radio Science Meeting (Joint with AP-S Symposium), Atlanta, GA, USA, 2019, pp. 63-64, doi:10.1109/USNC - URSI.2019.8861853.

C5 Afifi I., Beltayib A., Sebak A.R. (2020) Ultra-Wideband Compact T-Junction with Optimized V Cut for Millimeter Wave Applications. In: Farouk M., Hassanein M. (eds) Recent Advances in Engineering Mathematics and Physics. Springer, Cham. http://doi-org-443.webvpn.fjmu.edu.cn/10.1007/978-3-030-39847-7_16

C6 Beltayib A., Afifi I., Sebak A.R. (2020) Excitation of the First High-Order Mode in Ridge Gap Waveguide. In: Farouk M., Hassanein M. (eds) Recent Advances in Engineering Mathematics and Physics. Springer, Cham. http://doi-org-443.webvpn.fjmu.edu.cn/10.1007/978-3-030-39847-7_17